

AD-A151 031

SYNTHESIS AND PROPERTIES OF ELEVATED TEMPERATURE P/M
ALUMINUM ALLOYS(U) NORTHWESTERN UNIV EVANSTON IL DEPT
OF MATERIALS SCIENCE ANDEE M E FINE ET AL 30 NOV 84

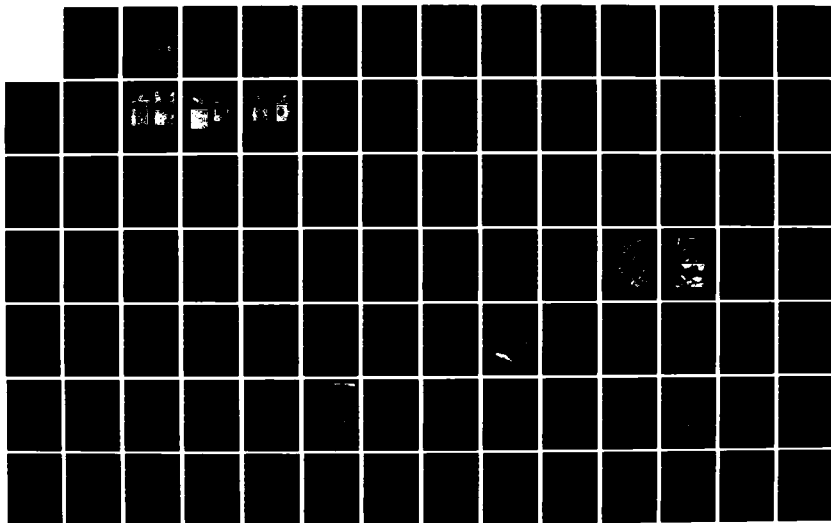
1/2

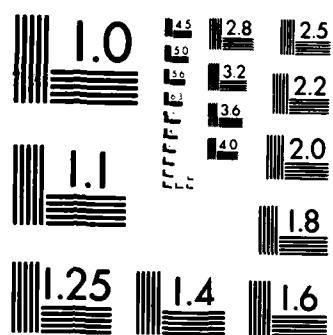
UNCLASSIFIED

AFOSR-TR-85-0139 AFOSR-82-0005

F/G 11/6

NL





MICROCOPY RESOLUTION TEST CHART
NATIONAL BUREAU OF STANDARDS-1963-A

AD-A151 031

DTIC FILE COPY

UNCLASSIFIED

SECURITY CLASSIFICATION OF THIS PAGE (When Data Entered)

REPORT DOCUMENTATION PAGE		READ INSTRUCTIONS BEFORE COMPLETING FORM
1. REPORT NUMBER AFOSR-TR- 85 - 0139	2. GOVT ACCESSION NO.	3. RECIPIENT'S CATALOG NUMBER
4. TITLE (and Subtitle) SYNTHESIS AND PROPERTIES OF ELEVATED TEMPERATURE P/M ALUMINUM ALLOYS		5. TYPE OF REPORT & PERIOD COVERED Annual Technical Report 10/1/83 - 9/30/84
		6. PERFORMING ORG. REPORT NUMBER
7. AUTHOR(s) Morris E. Fine Julia R. Weertman		8. CONTRACT OR GRANT NUMBER(s) AFOSR-82-0005
9. PERFORMING ORGANIZATION NAME AND ADDRESS Northwestern University Dept. of Materials Science & Engineering Evanston, Illinois 60201		10. PROGRAM ELEMENT, PROJECT, TASK AREA & WORK UNIT NUMBERS 2306/Al 61102F 612306
11. CONTROLLING OFFICE NAME AND ADDRESS Air Force Office of Scientific Research Bolling AFB, Building 410 Washington, D. C. 20332		12. REPORT DATE 11/30/84
14. MONITORING AGENCY NAME & ADDRESS (if different from Controlling Office)		13. NUMBER OF PAGES 94
		15. SECURITY CLASS. (of this report) Unclassified
		15a. DECLASSIFICATION DOWNGRADING SCHEDULE
16. DISTRIBUTION STATEMENT (of this Report) This document has been approved for public release unlimited ; its distribution is unlimited		
17. DISTRIBUTION STATEMENT (of the abstract entered in Block 20, if different from Report)		
18. SUPPLEMENTARY NOTES		
19. KEY WORDS (Continue on reverse side if necessary and identify by block number) Ostwald ripening (coarsening), aluminum-iron cerium alloy, aluminum- zirconium-vanadium alloy, iron-molybdenum-vanadium alloy, aluminum- molybdenum-vanadium alloy <i>ava</i>		
20. ABSTRACT (Continue on reverse side if necessary and identify by block number) The dispersed phases in the Al-8Fe, Al-10Fe-1.5Mo-1V, Al-8.8Fe-3.7Ce and Al-8.9Fe-6.9Ce RSP P/M alloys have been examined for composition and coarsening rate. Additionally, effects of prior heat treatment and deformation on particle coarsening have been studied. Energy dispersive spectroscopy on extracted particles from the Al-8Fe and Al-10Fe-1.5Mo-1V alloys in the as-received condi- tion as well as after aging at 316°C indicated that the particles have composi- tions close to Al ₃ Fe. In these two alloys, aging 240 hours at 425°C gives particles close to Al ₁₃ Fe ₄ in composition. In Al-Fe-Ce alloys aged at 425°C,		

DD FORM 1 JAN 73 1473

EDITION OF 1 NOV 65 IS OBSOLETE

85 02 19 048

UNCLASSIFIED

SECURITY CLASSIFICATION OF THIS PAGE (When Data Entered)

UNCLASSIFIED

SECURITY CLASSIFICATION OF THIS PAGE(When Data Entered)

two kinds of particles are present with composition close to $\text{Al}_{13}\text{Fe}_4$ and $\text{Al}_{10}\text{Fe}_2\text{Ce}$. Some Al_5Fe is seen in these alloys in the as-received condition and also after aging at 316°C . Overall coarsening rates of the dispersed phases indicate that at 375 and 425°C the Al-Fe-Mo-V alloy coarsens more slowly than the other three alloys. Creep deformation of the Al-8.8Fe-3.7Ce alloy enhances particle coarsening rates while no such effect is noted after fatigue deformation. A high temperature age preceding a low temperature age gives a stable microstructure at the lower temperature.

The improved lattice matching previously observed in the equilibrium, tetragonal $\text{Al}_3(\text{V}_{0.975}\text{Zr}_{0.125})$ over the unalloyed Al_3Zr phase was also found in the respective metastable cubic phases. This improvement in registry is suggested to be responsible for the improved stability and reduced coarsening kinetics of the cubic $\text{Al}_3(\text{V}_{0.975}\text{Zr}_{0.125})$ phase ($\sigma = 65 \text{ ergs/cm}^2$) when compared to the unalloyed Al-Zr phase ($\sigma = 90 \text{ ergs/cm}^2$). Electron diffraction analysis was employed to determine the lattice parameters of both cubic phases. After the application of Vegard's Law, it was predicted that the cubic $\text{Al}_3(\text{V}_{0.725}\text{Zr}_{0.275})$ should be perfectly coherent with the Al matrix.

Diagram - Supplied Figure is included

4 EA

UNCLASSIFIED

SECURITY CLASSIFICATION OF THIS PAGE(When Data Entered)

AFOSR-TR- 85 - 0139

DEPARTMENT OF MATERIALS SCIENCE & ENGINEERING
THE TECHNOLOGICAL INSTITUTE
NORTHWESTERN UNIVERSITY
EVANSTON, ILLINOIS

Annual Technical Report on
Synthesis and Properties of Elevated Temperature P/M
Aluminum Alloys

AF Grant No.: AFOSR-82-0005

For the Period
1 October 1983 to 30 September 1984

Accession For	
NTIS GRA&I	<input checked="checked" type="checkbox"/>
DTIC TAB	<input type="checkbox"/>
Unannounced	<input type="checkbox"/>
Justification	
By _____	
Distribution/ _____	
Availability Codes	
Dist	Avail and/or Special
A-1	

Principal Investigators:

Morris E. Fine, Walter P. Murphy Professor of Materials Science and
Engineering (Telephone: (312) 492-5579)

Julia R. Weertman, Professor of Materials Science and Engineering
(Telephone: (312) 492-5353)

November 30, 1984

Approved for public release;
distribution unlimited.

Introduction

The objective of this research is to provide basic data needed to design a high temperature aluminum base alloy useful to the highest possible temperature and to evaluate the stability of some high temperature aluminum base alloys developed in recent years.

According to the Wagner-Lifshitz-Slyozov (W-L-S) theory for diffusion controlled coarsening of a dispersed phase the average radius at time t , \bar{r} ³ is proportional to $(\sigma DC_0 t)$ where σ is the interfacial energy, D is the diffusivity of the rate controlling element, and C_0 is the solubility limit. For microstructural stability at high temperatures, the dispersed phase must be thermodynamically stable, and the product σDC_0 must be small. Thus information about σ , D , and C_0 are needed as the basis for design of Al alloys for elevated temperature use. If D and C_0 are known, then measurement of \bar{r}_t vs. t at constant temperature gives σ . Low values of σ are expected when there is good lattice matching across the interface between dispersed phase and matrix.

Another important consideration is the stability of the microstructure under fatigue loading conditions. Cyclic plastic deformation generates vacancies which amplify the diffusivity. Since D is proportional to $(C_v e^{-q_m/kT})$ where C_v is the vacancy concentration, q_m is the motion energy of vacancy-atom exchange, k is the Boltzmann constant and T is the absolute temperature, even a factor of 2 or 3 increase in the vacancy concentration should have a profound effect on the microstructure.

During the past year the following topics were under study:

1. Al-Fe, Al-Fe-Ce, and Al-Fe-Mo-V alloys. Further work was done on characterizing the dispersed phase in the Al-Fe-Ce and Al-Fe-Mo-V alloys. The microstructural stability of these

AIR FORCE OFFICE OF SCIENTIFIC RESEARCH (AFOSR)
NOTICE OF TRANSMITTAL TO DTIC
1 This technical report has been reviewed and is approved for public release IAA AFOSR 190-12. Distribution is unlimited.
MATTHEW J. KERRER
Chief, Technical Information Division

alloys upon exposure to high temperatures were compared, with and without prior cold work. Further studies on the effect of creep and fatigue deformation on dispersoid coarsening were carried out.

2. In Al-Al₃X alloys the best matching between Al and Al₃X (tetragonal DO₂₃ type) was obtained with Al₃(V_{.875}Zr_{.125}). Supersaturated solid solutions of one volume % Al₃Zr in Al and Al₃(V_{.875}Zr_{.125}) in Al were prepared by arc melting. Precipitation and coarsening of the precipitates were thoroughly studied in these alloys.
3. Coarsening rate of Al₃Mg₂ in Al was determined.
4. The modulus of Al₃Zr was determined.

1. Studies of the Al-Fe, Al-Fe-Mo-V and Al-Fe-Ce RSP P/M Alloys

An Al-8.0Fe alloy in the form of an upset pancake and an Al-8.9Fe-6.9Ce extrusion were recently obtained from Alcoa. An Al-10Fe-1.5Mo-1V alloy in the form of halves of broken tensile specimens, and an Al-8.8Fe-3.7Ce extrusion had been obtained from the AFML earlier. These alloys have been used in studies aimed at the identification of the dispersed phases and in the comparison of microstructural stability upon exposure to elevated temperatures with and without prior cold work. Additionally, the Al-8.8Fe-3.7Ce alloy was used in a study of the effect of creep and fatigue deformation on dispersoid coarsening. Some microstructural examination of dilute Al-Fe alloys (0.1% and 0.04% Fe), prepared by arc melting high purity Al and Fe, has been carried out as well.

1.1. Identification of dispersoids in the RSP P/M alloys

X-ray diffractometer scans were run on the four alloys in the as-received condition and after aging various times at 316, 375 and 425°C. The diffraction information obtained from the Al-8.0Fe forging clearly indicated the presence of only Al(ss) and Al_6Fe in the as-received condition and after aging at 316°C. Material aged at 375°C contained both Al_6Fe and $\text{Al}_{13}\text{Fe}_4$ in the Al(ss), with the ratio of Al_6Fe to $\text{Al}_{13}\text{Fe}_4$ decreasing with increasing time at 375°C. Some Al_6Fe could be detected in the Al-8.0Fe alloy aged short times at 425°C; after 120 hours at 425°C no Al_6Fe remained. The relative quantities of the two dispersed phases as a function of aging temperature and time are presented in Fig. 1. Plotted is $I_{\text{Al}_6\text{Fe}}/I_{\text{Al}_6\text{Fe},0}$ and $I_{\text{Al}_{13}\text{Fe}_4}/I_{\text{Al}_{13}\text{Fe}_4,0}$ as a function of time for the unaged Al-Fe alloy and the alloy aged at 316, 375 and 425°C. The intensities $I_{\text{Al}_6\text{Fe}}$ and $I_{\text{Al}_{13}\text{Fe}_4}$ refer to integrated intensities averaged over the three highest peaks of each phase. The normalizing intensities $I_{\text{Al}_6\text{Fe},0}$ and $I_{\text{Al}_{13}\text{Fe}_4,0}$ refer to the integrated intensities for conditions where all precipitation is

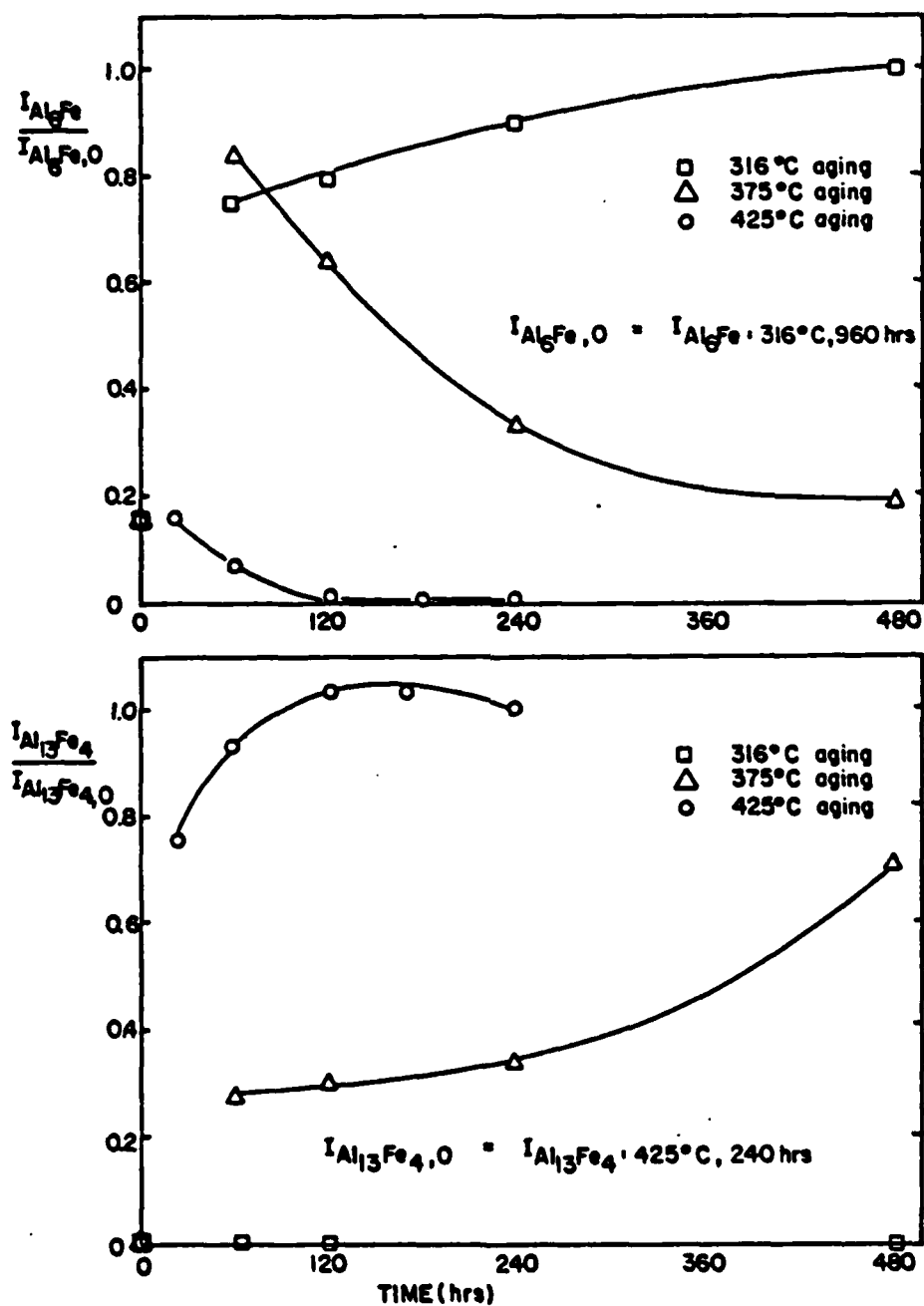


Fig. 1. Relative quantities of the Al_6Fe and $Al_{13}Fe_4$ phases present in the Al-8.0Fe forging as a function of aging temperature and time.

assumed complete, i.e., integrated intensity of Al_6Fe in the alloy aged 40 days at 316°C and $\text{Al}_{13}\text{Fe}_4$ in the material aged 10 days at 425°C respectively.

Interplanar spacings obtained by x-ray diffraction of the Al-Fe-Mo-V alloy in the as-received condition and after aging at a higher temperature, 575°C , have been reported earlier (1). Reflections in the as-received material were matched to the Al_6Fe phase; reflections in material aged at 575°C were matched to Al_3Fe , or more accurately expressed, $\text{Al}_{13}\text{Fe}_4$. No additional phases were found, indicating substitution of Mo and V for Fe in these phases. Aging the Al-Fe-Mo-V alloy at 316°C did not change the structure of the as-received material. Material aged at 425°C contained primarily $\text{Al}_{13}\text{Fe}_4$ although some Al_6Fe reflections were still weakly present even after aging 10 days.

X-ray diffraction of the Al-Fe-Ce extrusions aged at 425°C revealed essentially the same peaks as had been reported earlier for the Al-7.5Fe-3.7Ce forging aged at higher temperatures. Small differences were noted in relative peak intensities and small shifts of the lower intensity peak positions. The d-spacings representing reflections found in the three Al-Fe-Ce alloys aged at 425, 475 and 575°C have been retabulated in Table 1 of this report in order to facilitate comparison to the d-spacings reported for the $\text{Al}_{13}\text{Fe}_4$ (2) phase and to a body centered tetragonal $\text{Al}_8\text{Mn}_4\text{Ce}$ phase (3). The good match suggests that the equilibrium $\text{Al}_{10}\text{Fe}_2\text{Ce}$ phase may be body centered tetragonal, having lattice parameters similar to those of $\text{Al}_8\text{Mn}_4\text{Ce}$.

The x-ray diffraction information obtained for both Al-Fe-Ce alloys in the as-received condition and after aging at 316°C cannot be clearly matched to either of the aforementioned phases, although several of the $\text{Al}_{13}\text{Fe}_4$ and $\text{Al}_8\text{Mn}_4\text{Ce}$ high intensity peaks are observed. There is quite a bit of variation in peak position between the two alloys and between the as-

Table 1. Interplanar spacings for dispersed phases in the Al-7.5Fe-3.4Ce and Al-8.8Fe-3.7Ce RSP P/M alloys aged at 425°C, 475°C and 575°C for times from 24 to 240 hours

d (nm)*	I/I*	d (nm)†	I/I ₀ †	
0.690	10	0.7089	16	Al ₁₃ Fe ₄
0.671	10			
0.652	10	0.6523	22	Al ₁₃ Fe ₄
0.639	10	0.6499	6	Al ₈ Mn ₄ Ce, (110)
0.543-0.551	10			
0.511-0.519	10-20			
0.431-0.452	10-20	0.4490	10	Al ₈ Mn ₄ Ce, (200), (101)
0.405-0.410	10-35	0.4064	29	Al ₁₃ Fe ₄
0.401	10-15	0.4001	75	Al ₁₃ Fe ₄
0.391-0.396	10-45	0.3872	8	Al ₁₃ Fe ₄
0.381-0.386	15-45	0.3826	3	Al ₁₃ Fe ₄
0.367-0.377	10-35	0.3682	60	Al ₁₃ Fe ₄
0.324-0.327	10	0.3268	30	Al ₁₃ Fe ₄
0.3225	20	0.3234	7	Al ₁₃ Fe ₄
0.317-0.320	10-30	0.3190	25	Al ₈ Mn ₄ Ce, (220), (211)
0.3005-0.303	10-15			
0.290-0.288	10	0.2862	16	Al ₈ Mn ₄ Ce, (310)
0.275-0.277	10-15			
0.262	30-35	0.2655	2	Al ₁₃ Fe ₄
0.258	15-30	0.2561	6	Al ₁₃ Fe ₄
0.243-0.244	25	0.2465	5	Al ₁₃ Fe ₄
0.228	10-20	0.2276	3	Al ₁₃ Fe ₄
0.2265-0.227	70	0.2261	17	Al ₁₃ Fe ₄
0.224-0.225	100	0.2241	100	Al ₈ Mn ₄ Ce, (400), (321)
0.220	15	0.2174	3	Al ₁₃ Fe ₄
0.211	30	0.212	85	Al ₁₃ Fe ₄
0.209-0.210	30-70	0.209	138	Al ₁₃ Fe ₄
0.206	30	0.2056	111	Al ₁₃ Fe ₄
0.201	10-20	0.2004	131	Al ₁₃ Fe ₄
0.194	20-25	0.1938	24	Al ₁₃ Fe ₄
0.1834	10			
0.1828	10	0.1827	2	Al ₁₃ Fe ₄
0.160	10			
0.159	30	0.1588	40	Al ₈ Mn ₄ Ce, (440), (521)
0.158	10			
0.157	10			

* refer to d-spacings and relative intensities in the Al-Fe-Ce alloys

† refer to d-spacings and relative intensities for Al₁₃Fe₄ and Al₁₀Fe₂Ce phases (2,3)

received and 316°C aged patterns. Additionally, peaks were generally of low intensity and broadened.

To obtain additional information on dispersoid composition, extraction replicas were prepared from samples of each of the four alloys in the as-received condition and after aging 240 hours at 316°C or 240 hours at 425°C. The extraction was performed using the electrolyte of Cocks et al. (4). A constant current source and an aluminum cathode were used to apply 10 to 40 mA/cm² for 1 to 4 minutes to each specimen. Specimens were thoroughly rinsed and heavy (0.08 mm thick) replicating tape was applied to the surface. After removal, the tape containing extracted particles was carbon coated, the replicating plastic was dissolved and the films were mounted on electron microscope grids in the conventional manner.

Energy dispersive spectroscopy was done on extracted particles with a Hitachi H700-H STEM having an attached Kevex microanalysis system. Spectra were acquired from 25 to 70 extracted particles from each specimen, depending on the variability noted. The Quantex Ray system was used for analysis of the resulting spectra. Additionally, selected area diffraction patterns from particles of each material were obtained and analyzed.

The EDS results on the four alloys are summarized in Table 2. Included in the table are the number of particles analyzed for each condition. The results on the stoichiometry of the Al-Fe phases in the Al-8.0Fe alloy are consistent with information obtained from x-ray diffraction; Al₅Fe is present in unaged material and in material aged at 316°C; Al₁₃Fe₄ is present in material aged at 425°C. The slightly lower aluminum content in the "Al₅Fe" particles in the as-received material versus the material aged at 316°C may reflect a higher temperature of formation of the particles during rapid quenching.

Table 2. Summary of the Compositional Analysis of the Dispersed Phases in the RSP P/M Alloys of the Present Study.

Alloy Composition (wt. %)	Particle Composition (at. %)		
	As Received	316°C-240 hrs	425°C-240 hrs
Al-8Fe	21 particles:	18 particles:	12 particles:
	83.87 ± 1.50 Al	86.84 ± 0.65 Al	76.53 ± 1.42 Al
	16.13 ± 1.50 Fe	13.16 ± 0.65 Fe	23.47 ± 1.42 Fe
Al-10Fe-1.5Mo-1V	5 particles:		6 particles:
	86.54 ± 3.14 Al		80.14 ± 2.67 Al
	13.46 ± 3.14 Fe		19.86 ± 2.67 Fe
	19 particles:	-	13 particles:
	85.46 ± 0.51 Al		87.24 ± 1.52 Al
	11.36 ± 0.43 Fe		8.14 ± 2.45 Fe
	1.56 ± 0.12 Mo		2.04 ± 0.39 Mo
	1.61 ± 0.12 V		2.64 ± 1.62 V
Al-8.9Fe-6.9Ce	4 particles:	7 particles:	5 particles:
	87.98 ± 1.99 Al	86.66 ± 2.96 Al	79.77 ± 1.36 Al
	12.02 ± 1.99 Fe	13.22 ± 2.96 Fe	20.23 ± 1.36 Fe
		0.13 ± 0.31 Ce	
	22 particles:	20 particles:	21 particles:
	83.84 ± 1.23 Al	82.15 ± 0.59 Al	79.12 ± 0.68 Al
	11.31 ± 1.41 Fe	12.38 ± 1.44 Fe	15.43 ± 0.63 Fe
	4.85 ± 0.74 Ce	5.46 ± 0.89 Ce	5.48 ± 0.35 Ce
Al-8.8Fe-3.7Ce	14 particles:	3 particles:	22 particles:
	85.76 ± 1.42 Al	83.96 ± 4.09 Al	81.43 ± 3.00 Al
	14.13 ± 1.40 Fe	15.82 ± 4.84 Fe	18.32 ± 3.00 Fe
	0.10 ± 0.12 Ce	0.27 ± 0.95 Ce	0.24 ± 0.13 Ce
	16 particles:	11 particles:	21 particles:
	78.99 ± 0.86 Al	78.36 ± 0.96 Al	81.88 ± 1.00 Al
	20.40 ± 0.86 Fe	20.95 ± 0.79 Fe	13.53 ± 0.82 Fe
	0.62 ± 0.40 Ce	0.69 ± 0.42 Ce	4.59 ± 0.54 Ce
	34 particles:	10 particles:	
	81.77 ± 0.71 Al	79.69 ± 1.32 Al	
	13.89 ± 0.92 Fe	16.49 ± 1.98 Fe	
	4.34 ± 0.50 Ce	3.82 ± 0.42 Ce	
Al ₃ Fe: 85.7 Al 14.3 Fe	Al ₁₂ Fe ₄ : 76.5 Al 23.5 Fe	Al ₁₀ Fe ₂ Ce: 76.9 Al 15.4 Fe 7.7 Ce	

EDS results on the Al-Fe-Mo-V alloy are similar to those of the Al-Fe alloy, as expected. The aluminum concentration of the particles from the as-received material is consistent with the aluminum concentration in Al_3Fe . The iron content is somewhat low in most particles; several percent Mo and V appear to substitute for Fe in this phase. Some particles of the Al_3Fe type are seen having undetectable amounts of Mo or V. The compositions of particles in the material aged 240 hours at 425°C are more often consistent with the Al_3Fe stoichiometry than with the stoichiometry of $\text{Al}_{13}\text{Fe}_4$. This is in contrast to what was noted in the x-ray diffraction results, where some evidence of Al_3Fe was present but the pattern clearly indicated a higher volume fraction of $\text{Al}_{13}\text{Fe}_4$. This may be an artifact due to a preference in the extraction technique for removal of Al_3Fe .

The EDS results from both Al-Fe-Ce alloys aged at 425°C could be neatly divided into two groups; particles which contain little or no cerium and particles which contain substantial quantities of cerium. There is some correlation between morphology and composition. Elongated particles generally contain no cerium and more equiaxed particles generally contain cerium. Measured compositions for the two types of particles match well to the compositions of $\text{Al}_{13}\text{Fe}_4$ and $\text{Al}_{10}\text{Fe}_2\text{Ce}$. However, the Al concentrations are slightly high and the Fe and Ce concentrations are correspondingly low. Some x-ray mapping was done to determine whether there was any variation in particle size with particle type. Coarsening theory would predict that, since cerium diffusivity reported in aluminum is much slower than iron diffusivity in aluminum, the particles containing Ce should coarsen more slowly. Although no quantitative separation of particle size distributions was done, qualitative examination of the x-ray maps indicated that the Ce-containing particles are comparable in size to those particles having no cerium.

Results on the Al-8.8Fe-3.7Ce and Al-8.9Fe-6.9Ce alloys in the as-received and 316°C aged state show, in addition to the two types of particles mentioned above, particles having compositions close to Al_6Fe . The number fraction of particles containing Ce is higher in the alloy with the higher Ce content.

The volume fraction of dispersed phase present in the four alloys was measured by a point counting technique and compared to the volume fractions predicted from alloy composition and the phase or phases assumed present. This comparison is shown in Table 3. In the Al-8.0Fe alloy, if all Fe goes to form Al_6Fe , 22.3 volume percent dispersoid is expected; if it goes to form $\text{Al}_{13}\text{Fe}_4$, 15.6 percent is expected. The measured dispersoid volume fraction of 16 percent in the alloy aged at 425°C is consistent with the presence of all $\text{Al}_{13}\text{Fe}_4$. Table 3 shows that the as-received and 316°C aged Al-Fe-Mo-V alloys contain primarily Al_6Fe . Volume fraction measurements in the Al-Fe-Ce alloys seem to show that under all conditions examined, some Al_6Fe is present. Less is present after aging at 425°C.

Selected area diffraction patterns obtained for all alloys support the EDS results: patterns from particles in the binary alloy aged at 425°C were indexed to be $\text{Al}_{13}\text{Fe}_4$; patterns from particles in material aged at the lower temperature could be matched to the Al_6Fe structure (Fig. 2). The same trend was seen in the Al-Fe-Mo-V alloy: $\text{Al}_{13}\text{Fe}_4$ in material aged at 425°C; Al_6Fe in the as-received material (Fig. 3). Patterns from particles of the Al-Fe-Ce alloys aged at 425°C could be indexed either to monoclinic $\text{Al}_{13}\text{Fe}_4$ or to a body-centered tetragonal structure having lattice parameters similar to $\text{Al}_3\text{Mn}_4\text{Ce}$ (Fig. 4).

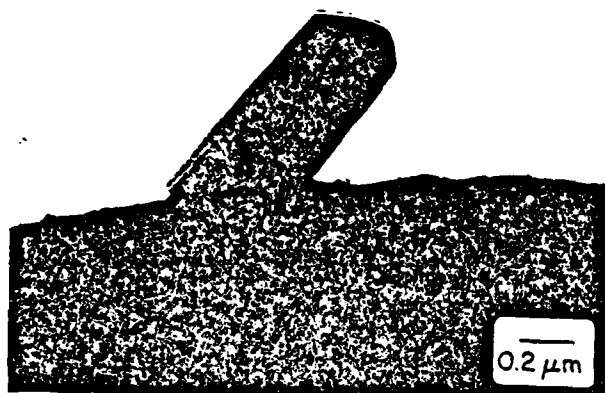
Table 3. Comparison of Measured and Predicted Dispersed Phase Volume Fraction in the RSP P/M Alloys of the Present Study

Alloy	Phases Assumed Present	Predicted Volume Fraction (%)	Measured Volume Fraction (%) *		
			As Received	316° C-240 hrs	425° C-240 hrs
Al-8Fe	Al ₆ Fe Al ₁₃ Fe ₄	22.3 15.6	-	-	16 ± 1
Al-10Fe-1.5Mo-1V	Al ₆ (Fe, Mo, V) Al ₁₃ (Fe, Mo, V) ₄	35.8 24.3	35 ± 1	33 ± 3	23 ± 1
Al-8.8Fe-3.7Ce	Al ₆ Fe + Al ₁₀ Fe ₂ Ce Al ₁₃ Fe ₄ + Al ₁₀ Fe ₂ Ce	27.8 21.7	25 ± 1	27 ± 2	23 ± 2
Al-8.9Fe-6.9Ce	Al ₆ Fe + Al ₁₀ Fe ₂ Ce Al ₁₃ Fe ₄ + Al ₁₀ Fe ₂ Ce	29.1 25.9	-	-	27 ± 4

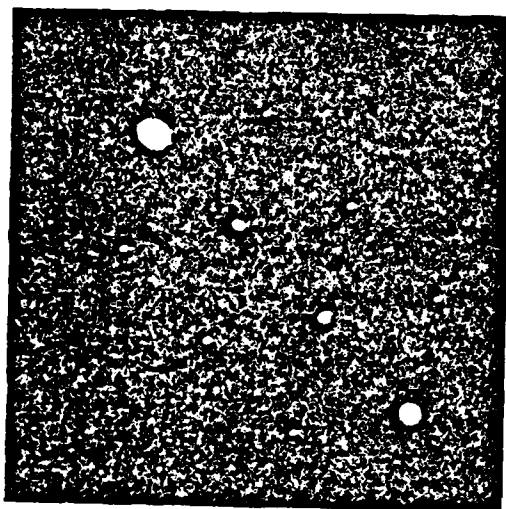
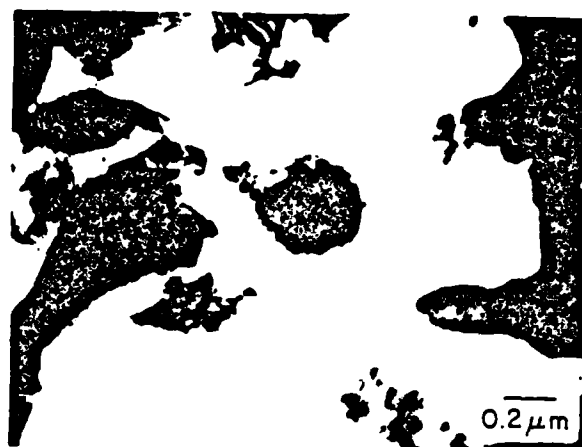
* + refers to 95% confidence intervals about the mean value

Al-8%Fe

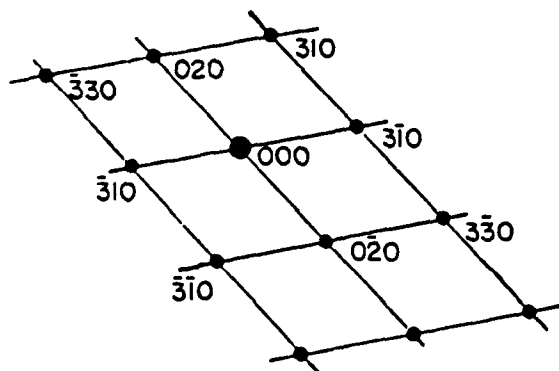
425°C - 240 hrs



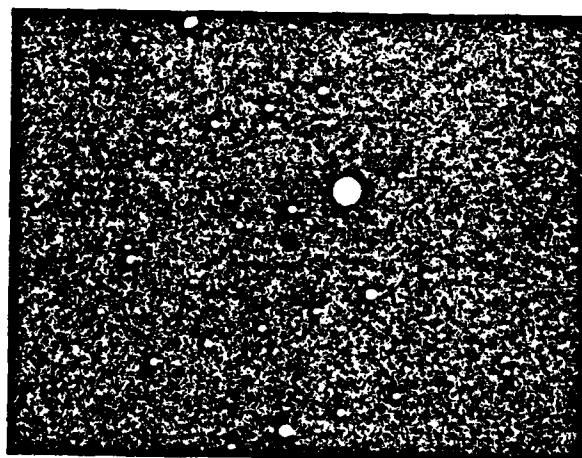
375°C - 240 hrs



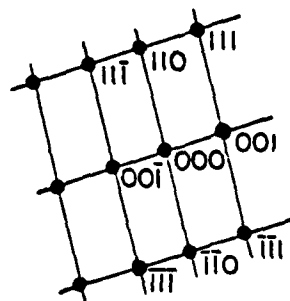
$\text{Al}_{13}\text{Fe}_4$ [001] Z.A.



(a)



Al_6Fe [110] Z.A.

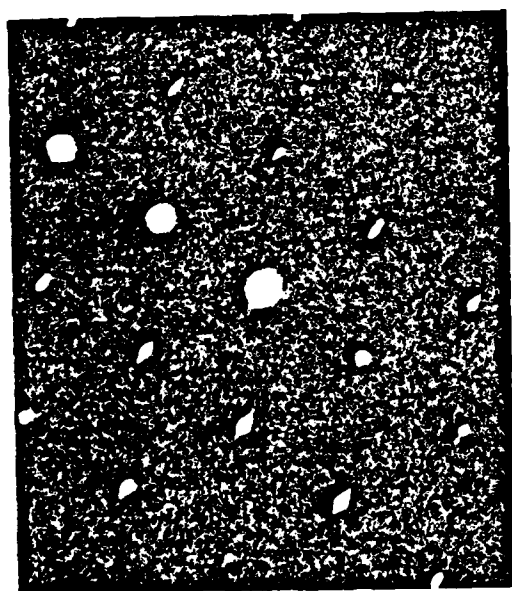
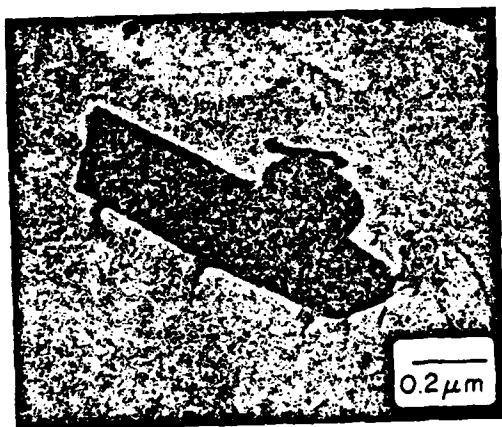


(b)

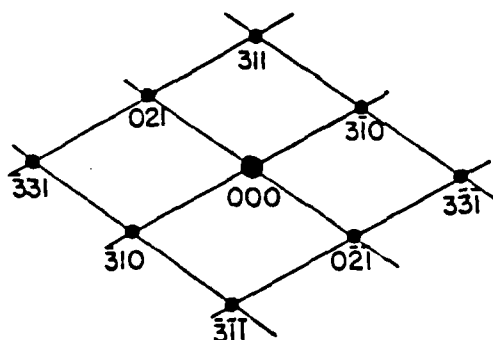
Fig. 2. Selected area diffraction pattern from particles in the Al-8Fe alloy: a) aged 240 hours at 425°C and b) aged 240 hours at 375°C.

Al-10%Fe-1.5%Mo-1%V

425°C - 240 hrs

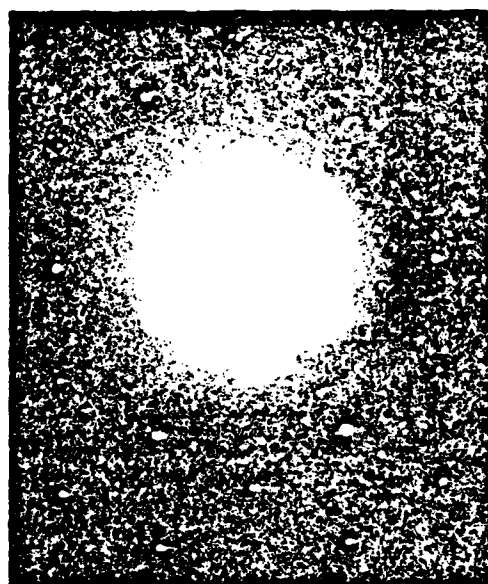


$\text{Al}_{13}\text{Fe}_4$ $[13\bar{6}]$ Z. A.

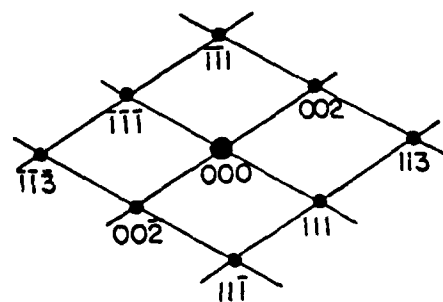


(a)

As Received



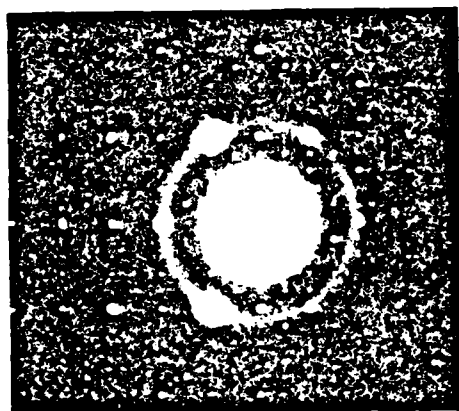
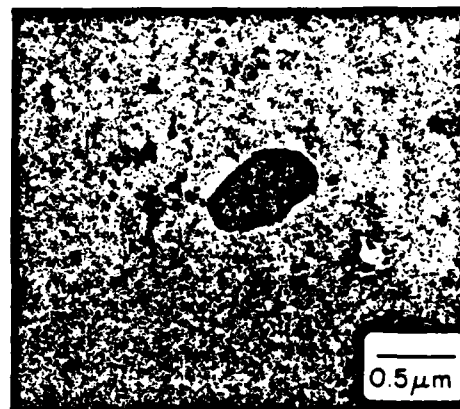
Al_6Fe $[\bar{1}10]$ Z. A.



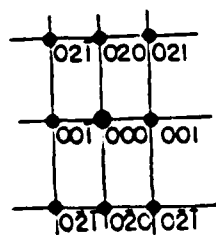
(b)

Fig. 3. Selected area diffraction patterns from particles in the Al-10Fe-1.5Mo-1V alloy: a) aged 240 hours at 425°C and b) in the as-received condition.

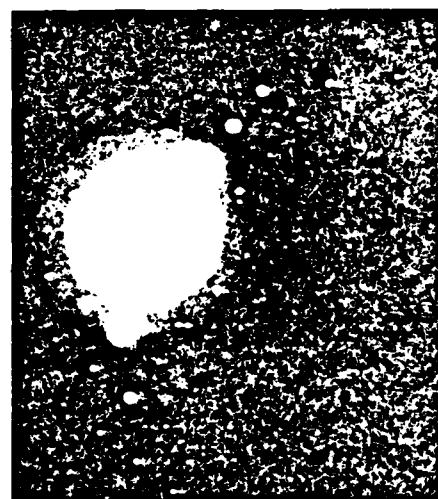
Al-8.8%Fe-3.7%Ce
425°C - 240hrs



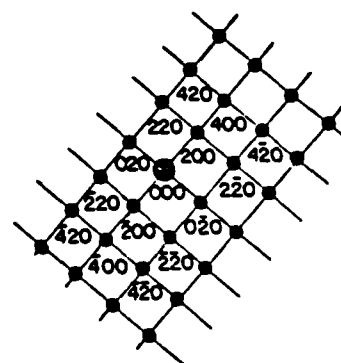
$\text{Al}_{13}\text{Fe}_4$ [100] Z.A.



(a)



$\text{Al}_{10}\text{Fe}_2\text{Ce}$ [001] Z.A.



(b)

Fig. 4. Selected area diffraction patterns from particles in the Al-8.8Fe-3.7Ce alloy: a) " $\text{Al}_{13}\text{Fe}_4$ " type and b) " $\text{Al}_{10}\text{Fe}_2\text{Ce}$ " type.

1.2. Coarsening kinetics of the alloys during exposure to high temperatures

The four alloys were aged varying lengths of time at 316, 375 and 425°C. Aging at 316°C was done in air; aging at 375 and 425°C was done in a vacuum of 1×10^{-3} Pa. Vickers microhardness measurements were taken from polished surfaces of the aged samples using a 300 gram load. Results of these microhardness measurements are presented in Figs. 5, 6 and 9. The microhardness of the Al-8.0Fe alloy drops more rapidly than the microhardness of any of the other alloys upon exposure to all three temperatures examined. However, the microhardness of the Al-8.0Fe alloy is for all conditions examined greater than the microhardness of the Al-8.8Fe-3.7Ce alloy.

Aging of the Al-10Fe-1.5Mo-1V, Al-8.9Fe-6.9Ce and Al-8.8Fe-3.7Ce alloys at 375°C and 425°C leads to a loss of microhardness. The rates at which these alloys lose hardness are comparable. In all cases, the microhardness of the Al-Fe-Mo-V alloy is highest and that of the Al-8.8Fe-3.7Ce alloy is lowest, but the actual values reflect not only dispersoid volume fraction and size but also the initial processing of the alloys.

Volume fraction of dispersoids, measured by the technique described earlier (1), has been plotted as a function of aging time at 425 and 375°C in Figs. 7 and 8 for the four alloys. The dispersoid volume fraction remains essentially constant for the Al-Fe-Ce alloys during aging at either temperature. Aging of the Al-8.0Fe alloy at 425°C shows constant volume fraction consistent with the volume fraction predicted if all of the Fe goes to form $\text{Al}_{13}\text{Fe}_4$. At 375°C, there is a decrease in volume fraction with time, expected as Al_3Fe transforms to $\text{Al}_{13}\text{Fe}_4$. Aging of the Al-Fe-Mo-V alloy at 425°C shows an initial drop in dispersoid volume fraction to the value expected for the $\text{Al}_{13}\text{Fe}_4$ phase. A constant high volume fraction is noted during aging at 375°C indicating the presence of the Al_3Fe phase.

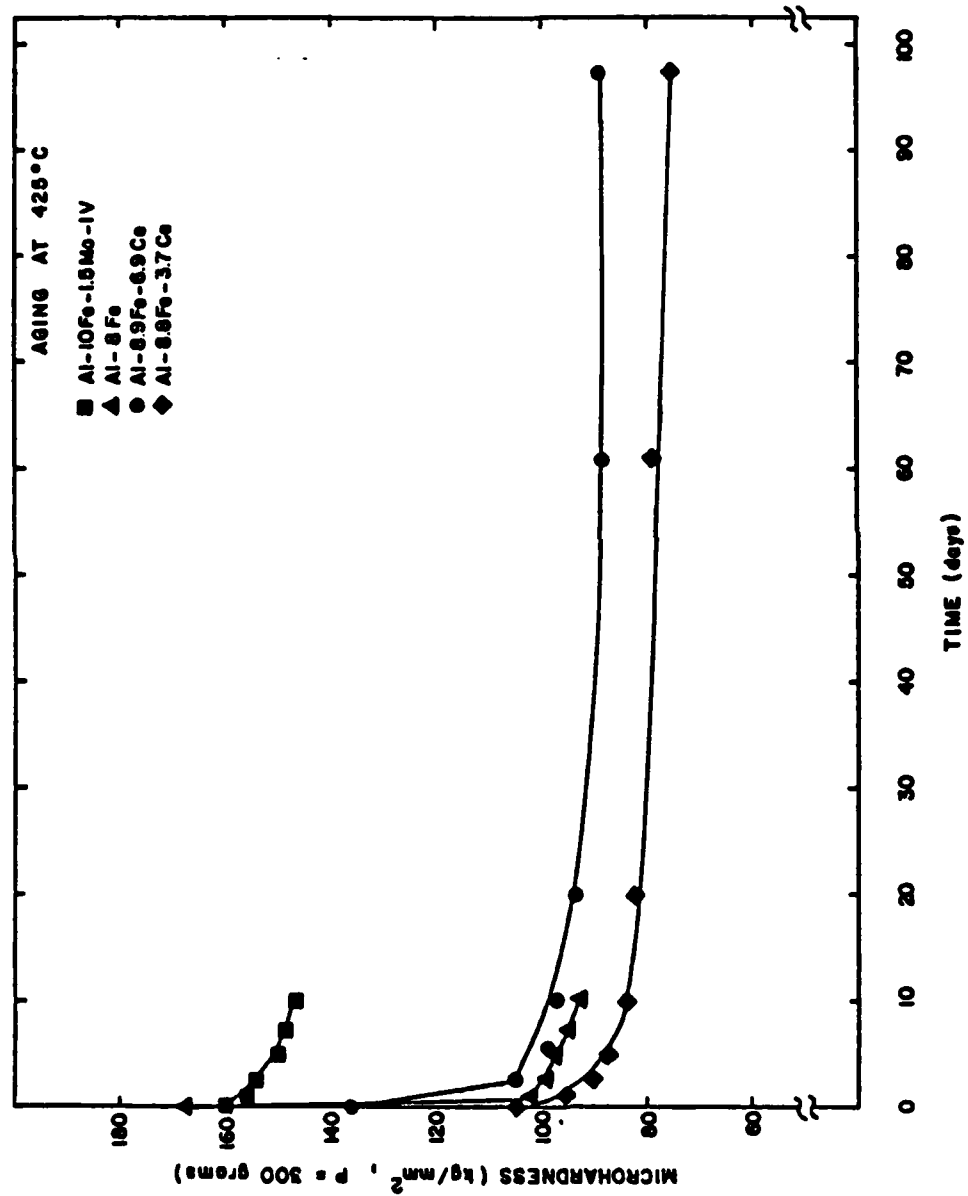


Fig. 5. Vickers microhardness vs. aging time at 425°C for the four RSP P/M alloys.

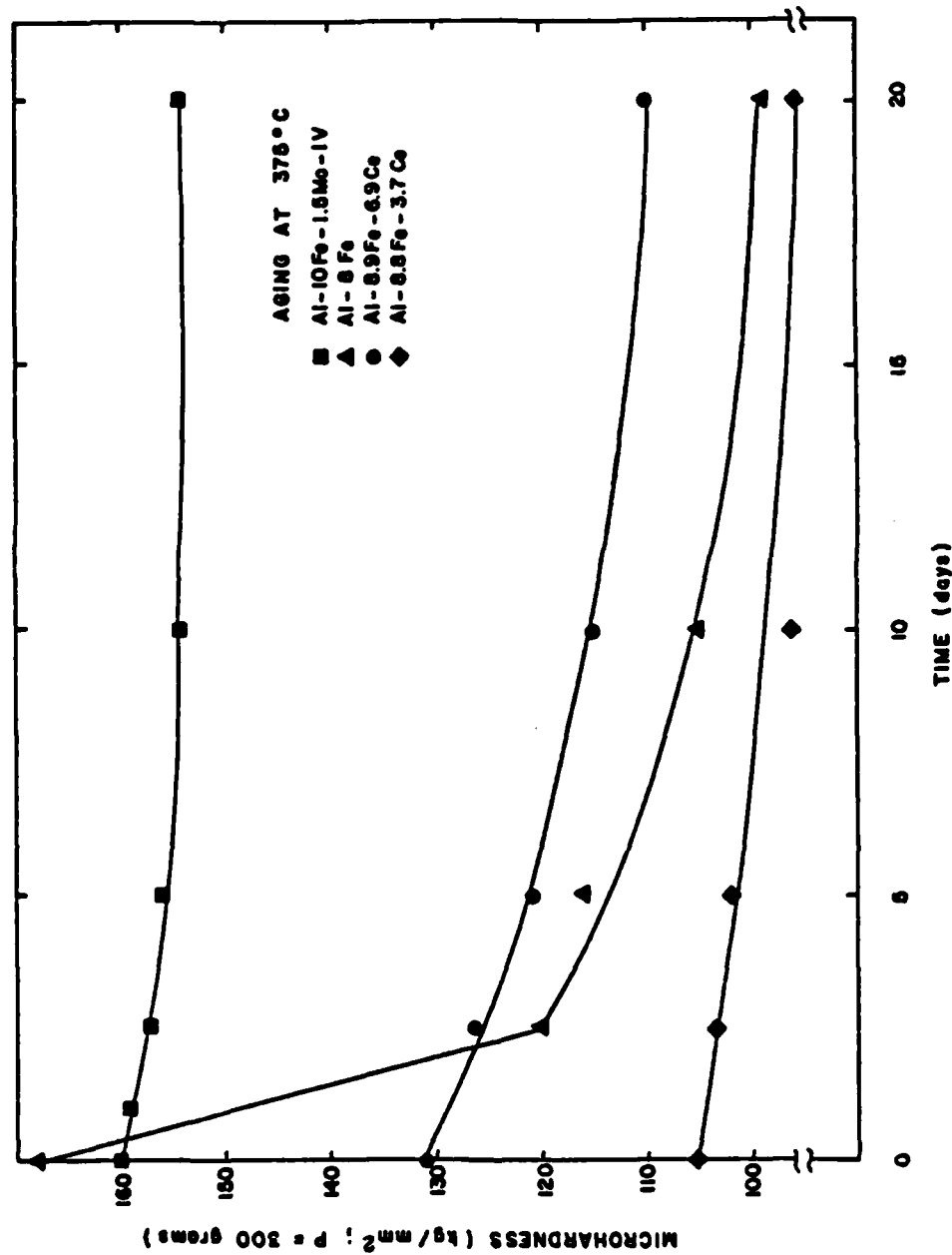


Fig. 6. Vickers microhardness vs. aging time at 375°C for the four RSP P/M alloys.

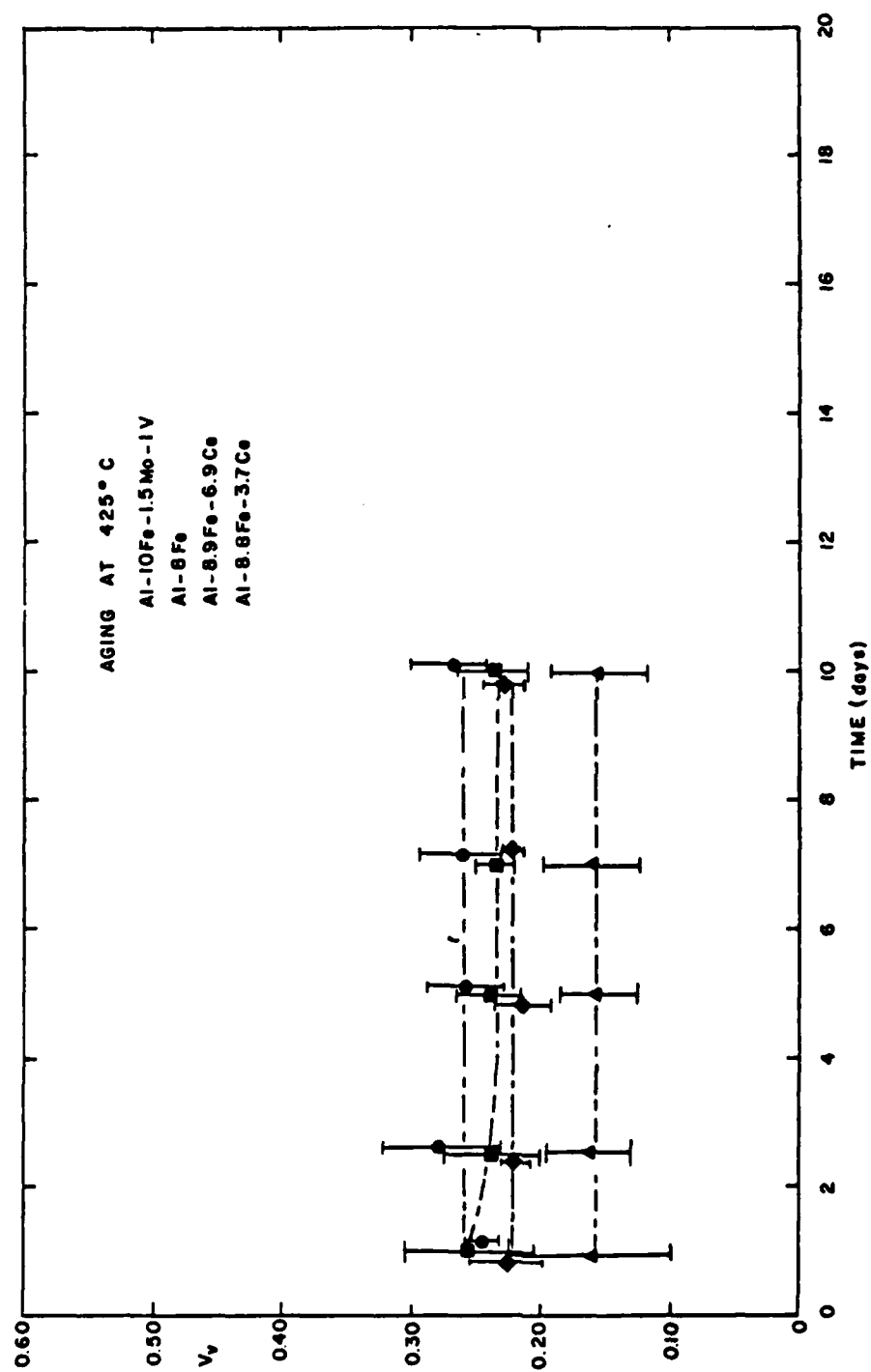


Fig. 7. Volume fraction dispersed phase vs. aging time at 425° C.

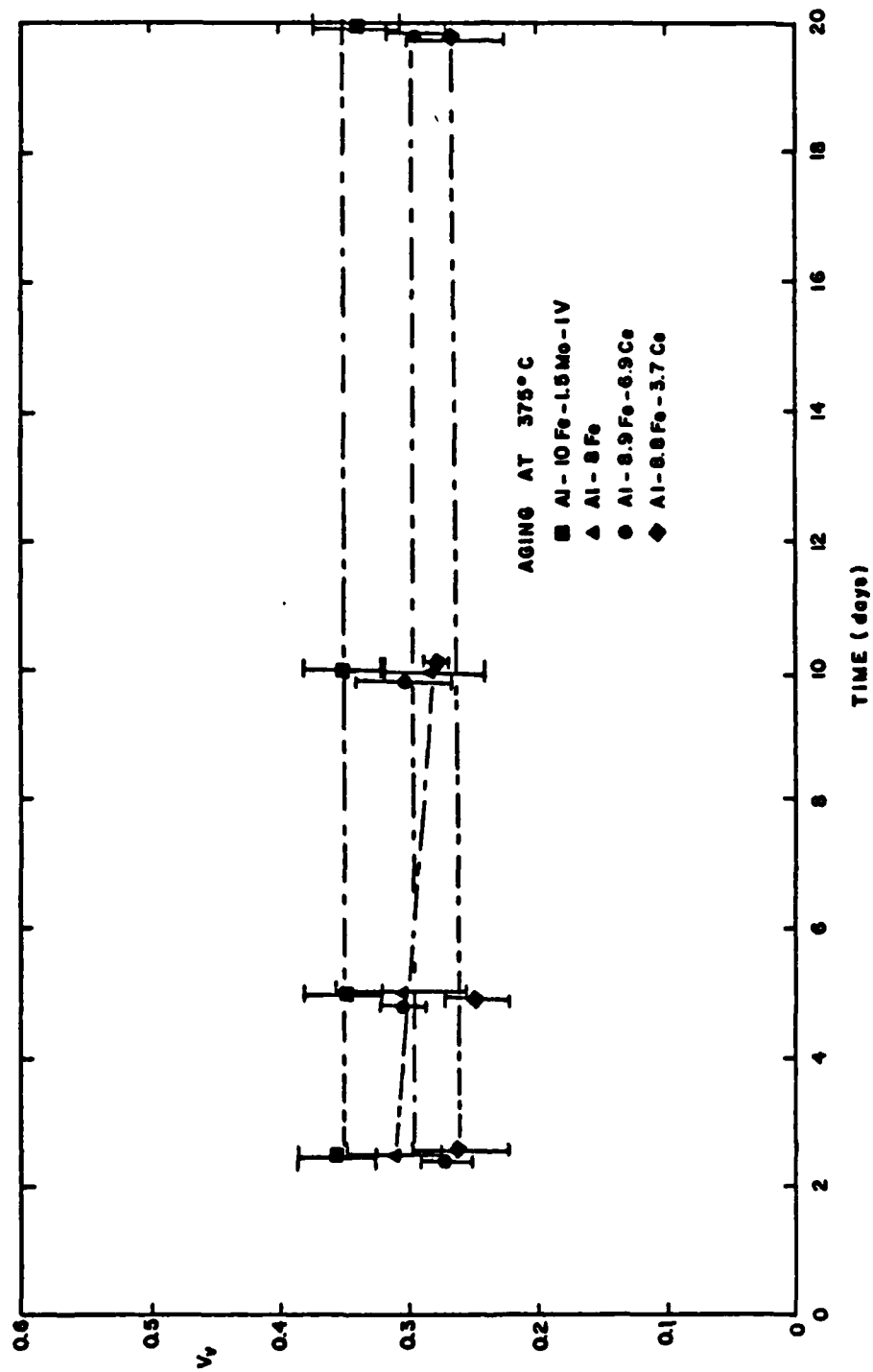


Fig. 8. Volume fraction dispersed phase vs. aging time at 375°C.

Aging of the Al-Fe-Mo-V and Al-Fe-Ce alloys at 316°C leads to a slight increase in microhardness, indicative of an increase in dispersoid volume fraction with a corresponding decrease in matrix supersaturation (Fig. 9).

Measurements of dispersed particle mean intercept length were made from TEM micrographs of two-stage replicas by the method used earlier (1). While no measurement of particle size was undertaken in the specimens aged at 316°C, the microstructure was observed. In Fig. 10a and b, the Al-Fe and Al-Fe-Mo-V microstructure after aging 480 hours at 316°C is shown. Note the inhomogeneity of both alloys preventing accurate determination of particle size. Particularly note the presence of large grain boundary particles and fine matrix particles. A comparison of the microstructures of the Al-Fe-Ce alloys aged 1488 hours at 316°C is seen in the TEM micrographs of shadowed two-stage replicas of Fig. 10c and d. The Al-Fe-Ce alloys are more homogeneous than the Al-Fe or Al-Fe-Mo-V alloys and appear similar to each other. The microstructures of the four alloys after aging 60 hours at 425°C are presented in the TEM micrographs of Fig. 11a through d.

The results of measurements of particle mean intercept lengths for all four alloys after aging at 425°C and 375°C are presented in Table 4. The + indicates the 95% confidence interval about the average value of mean intercept length calculated for different regions of the same specimen and do not refer in any way to the distribution of particle sizes.

A number of theories (5-8) modeling the coarsening of dispersed phase particles predict equations having the form

$$\bar{r}^n = A + B_n t$$

where \bar{r} is the average particle radius, t is time and A and B_n are constants. The exponent n is generally an integer between 2 and 5 and is indicative of

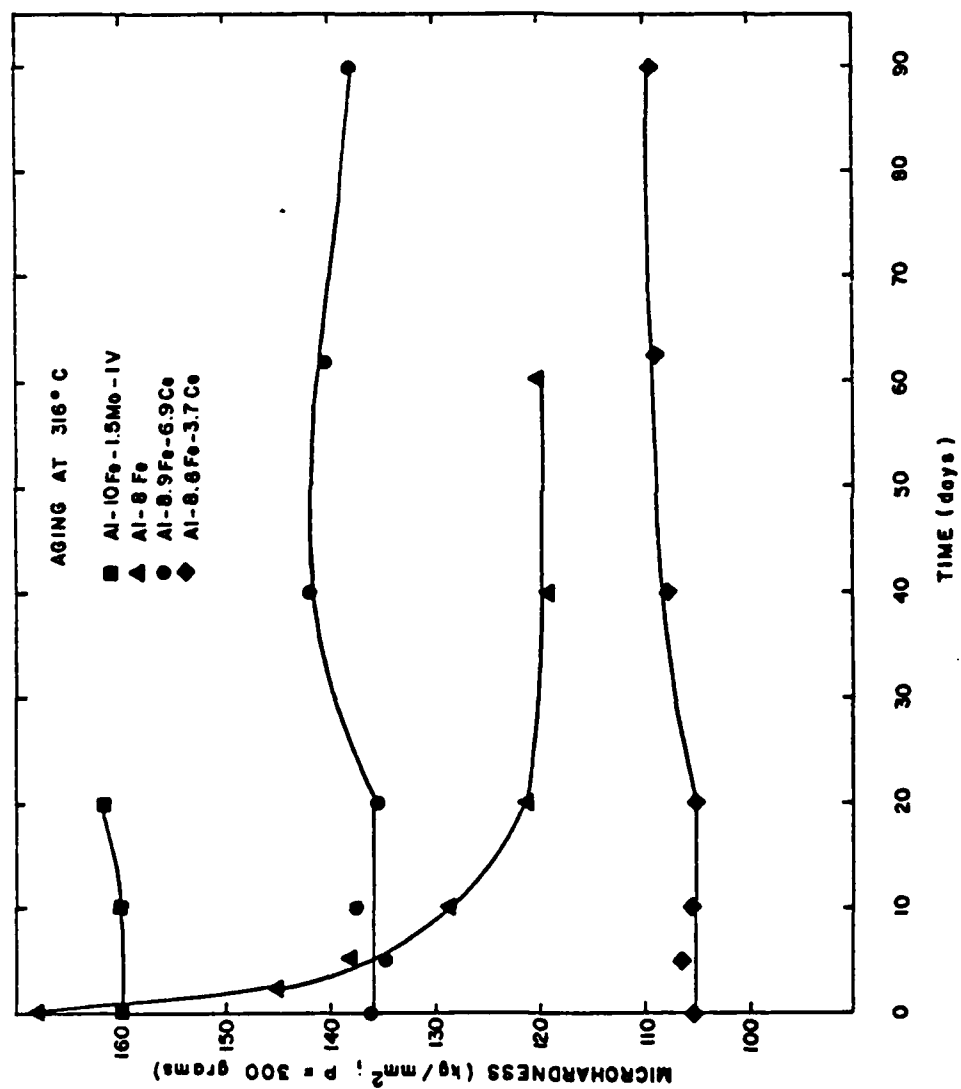


Fig. 9. Vickers microhardness vs. aging time at 316°C for the four RSP P/M alloys.

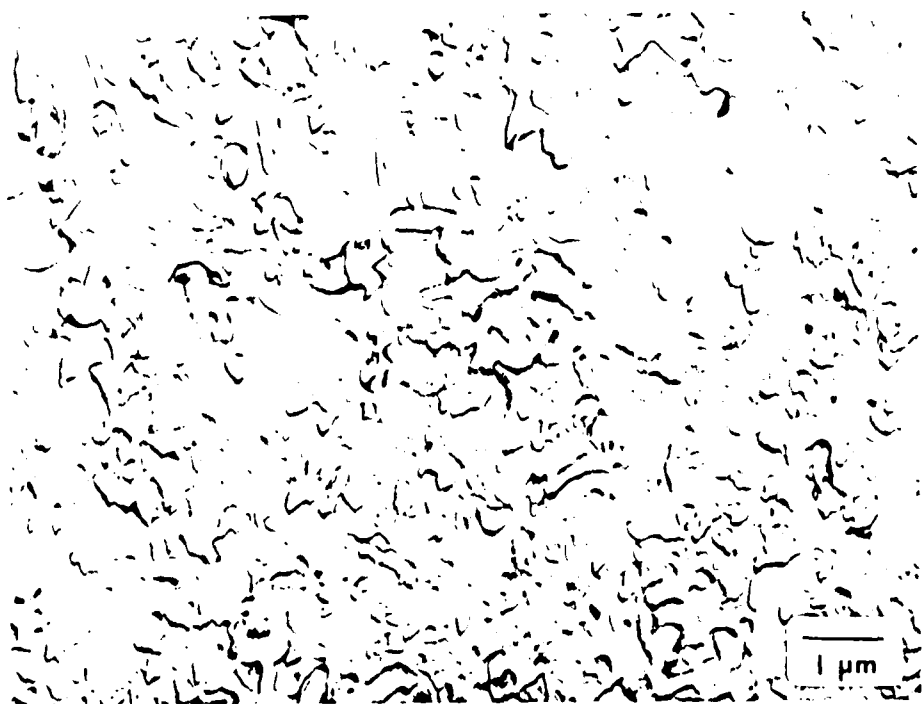


(a)



(b)

Fig. 10. TEM micrographs of shadowed two-stage replicas of specimens aged at 316°C: a) Al-8Fe after 480 hours, b) Al-10Fe-1.5Mo-1V after 480 hours, c) Al-8.8Fe-3.7Ce after 1488 hours and d) Al-8.9Fe-6.9Ce after 1488 hours.



(c)



(d)

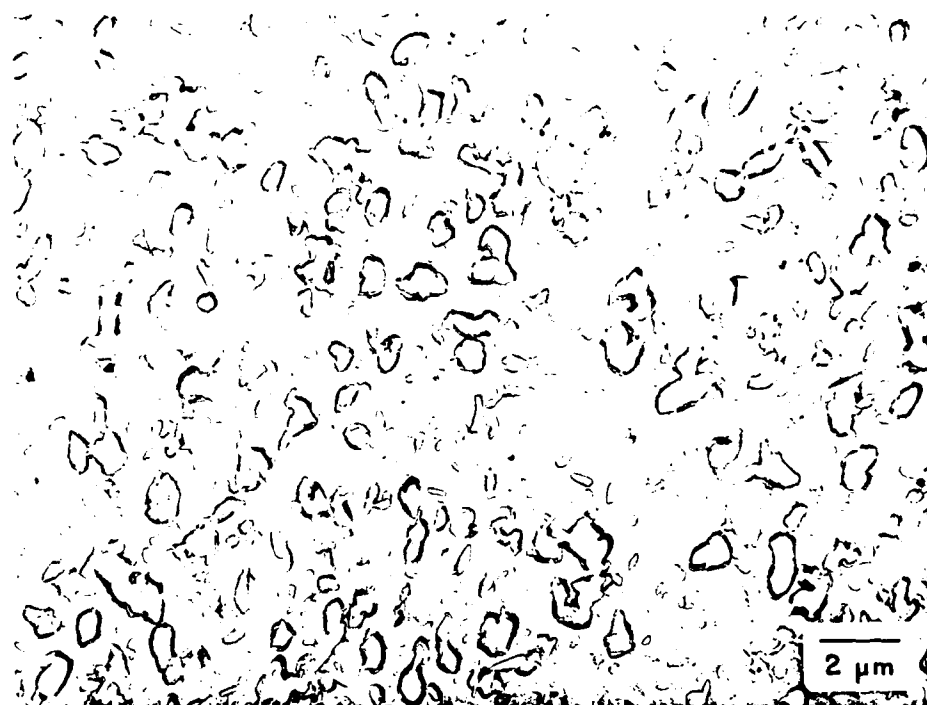


(a)

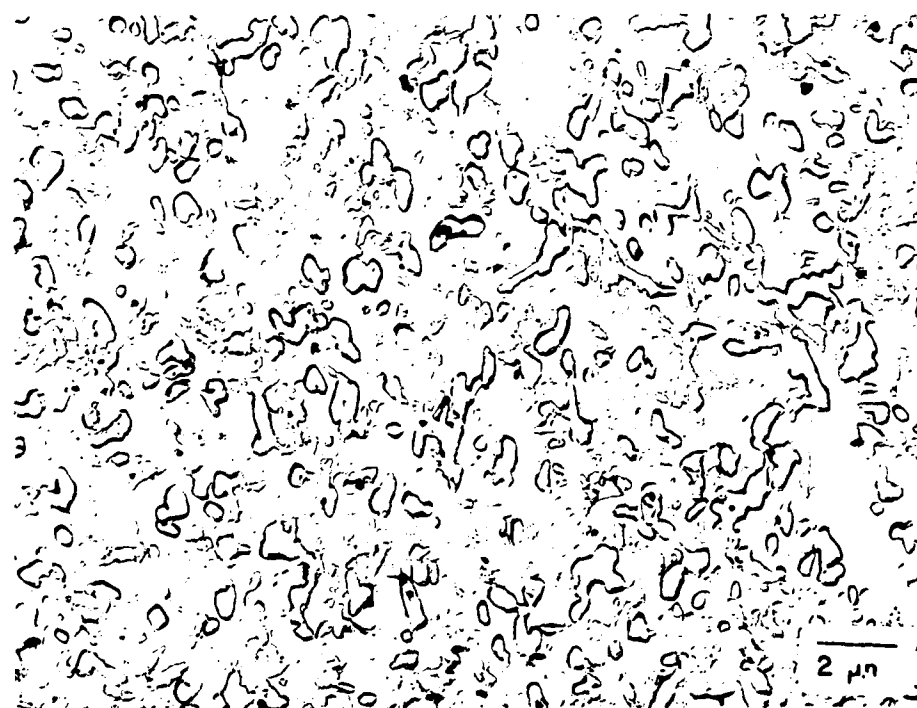


(b)

Fig. 11. TEM micrographs of shadowed two-stage replicas of specimens aged 60 hours at 425°C: a) Al-8Fe, b) Al-10Fe-1.5Mo-1V, c) Al-8.8Fe-3.7Ce and d) Al-8.9Fe-6.9Ce.



(c)



(d)

Table 4. Particle Mean Intercept Lengths for the RSP P/M Alloys Aged at 425 and 375°C.

Temperature (°C)	Time (hrs)	Particle Mean Intercept Length* (μm)		
		Al-8Fe	Al-10Fe-1.5Mo-1V	Al-8.8Fe-3.7Ce Al-8.9Fe-6.9Ce
425	24	0.16 ± 0.03	0.18 ± 0.03	0.17 ± 0.02 0.24 ± 0.03
425	60	0.17 ± 0.05	0.20 ± 0.03	0.24 ± 0.01 0.26 ± 0.04
425	120	0.23 ± 0.03	0.24 ± 0.03	0.34 ± 0.04 0.33 ± 0.04
425	168	0.25 ± 0.05	0.26 ± 0.03	0.35 ± 0.02 0.31 ± 0.02
425	240	0.29 ± 0.05	0.29 ± 0.03	0.37 ± 0.02 0.36 ± 0.04
375	60	0.13 ± 0.03	0.14 ± 0.03	0.17 ± 0.01 0.22 ± 0.04
375	120	0.17 ± 0.03	0.15 ± 0.03	0.19 ± 0.02 0.28 ± 0.02
375	240	0.22 ± 0.03	0.17 ± 0.03	0.24 ± 0.02 0.28 ± 0.02
375	480	-	0.18 ± 0.03	0.23 ± 0.01 0.34 ± 0.02

* ± refers to 95% confidence intervals about the mean value

the rate controlling mechanism of growth, i.e., growth by reaction at the interface ($n=2$), by bulk diffusion ($n=3$), by grain boundary diffusion ($n=4$), or by dislocation pipe diffusion ($n=5$). All models require several simplifying assumptions. Binary alloys having a very dilute dispersion of a single phase may be treated easily. The alloy systems of this study all have a relatively high volume fraction dispersed phase having non-spherical morphology. Of course, both the Al-Fe-Mo-V and Al-Fe-Ce alloys are ternary systems, but additional complications arise in the Al-Fe-Ce system because of the presence of two types of particles. Nevertheless, the mean intercept length data of this study was inserted into the above expression for the cases where $n=1, 2, 3, 4$ and 5 . A least squares analysis was used to obtain a 'rate constant' B_n for each case. Additionally, a correlation coefficient, R , was calculated to obtain a quantitative measure of the linearity for each case. The correlation coefficient R is given by the expression

$$R = \frac{m \sum_{i=1}^m \bar{L}_i^n t_i - (\sum \bar{L}_i^n)(\sum t_i)}{\sqrt{\{m(\sum \bar{L}_i^{2n}) - (\sum t_i)^2\} \{m \sum \bar{L}_i^{2n} - (\sum \bar{L}_i^n)^2\}}}$$

where m is the number of data points available and i represents an individual data point.

Values of R closest to unity represent the best linear fit. In Fig. 12, the coefficient R is plotted versus the exponent n for the data taken from specimens aged at 425 and 375°C. A value of $n=3$ appears to give the best fit for aging all alloys except Al-8.8Fe-3.7Ce at 425°C. A higher exponent gives a better fit for the Al-8.8Fe-3.7Ce data at 425°C. At 375°C, an exponent $n=3$ still gives the best fit for the Al-8.0Fe alloy, while a higher exponent gives a better fit for the other alloys. This type of analysis seems to show that different coarsening mechanisms operate between the two temperatures and between the four alloys.

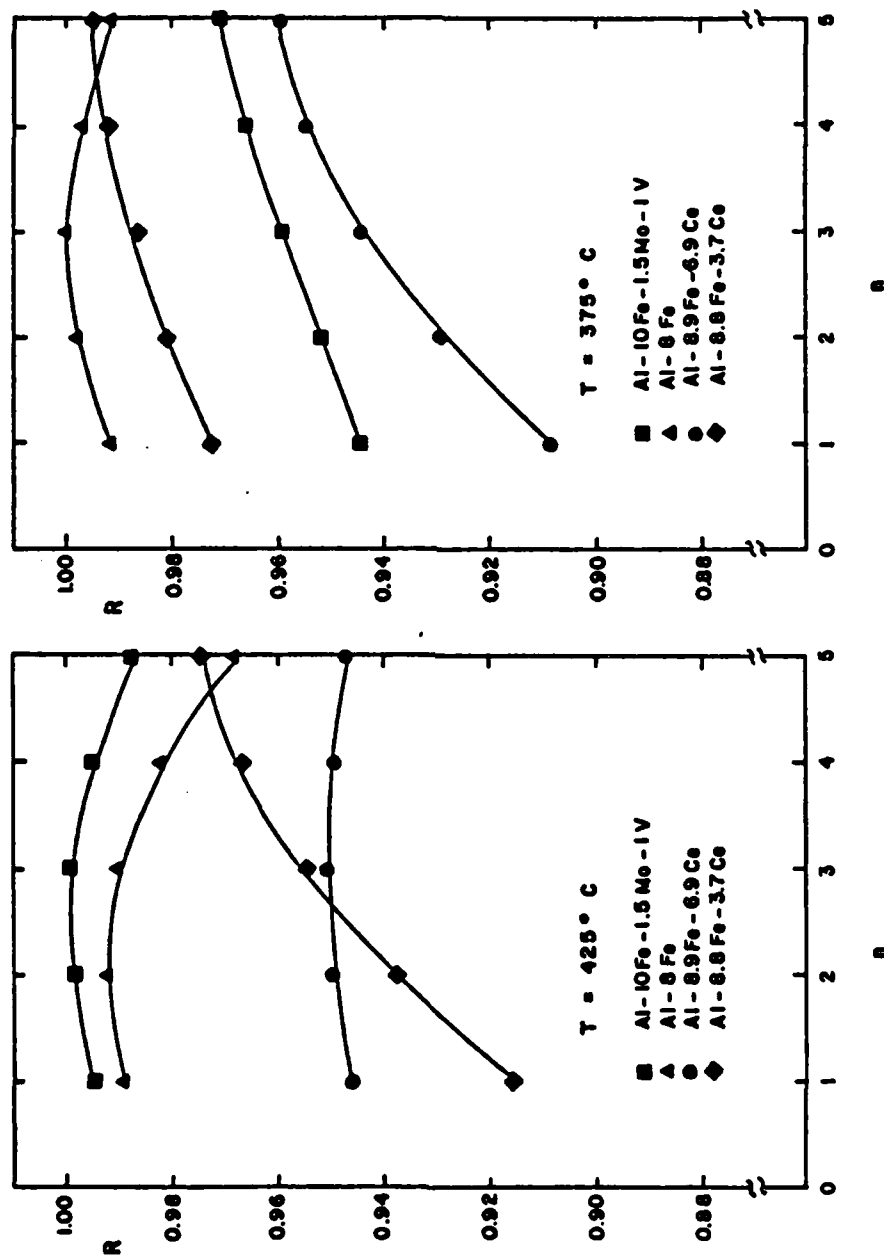


Fig. 12. Least squares correlation coefficient, R , vs. exponent, n , for aging of the RSP P/M alloys at a) 425°C and b) 375°C .

In Figs. 13 and 14, the data has been plotted as \bar{L}^3 vs. time to conform with the predictions of the LSW theory for bulk diffusion controlled coarsening. The rate constants, measured from the slopes of the \bar{L}^3 vs. time curves, have been listed in Table 5. The measured rate constants are compared to rate constants calculated using the LSW model:

$$K = \frac{8}{9} \frac{\sigma D C_0 \Omega^2}{X_B k T} \frac{K(\phi)}{K(0)} \cdot \xi$$

where σ is the particle-matrix interfacial energy, D is the diffusivity of the solute in the matrix, C_0 is the equilibrium solubility limit of the solute in the matrix, Ω is the atomic volume of the solute in the dispersed phase, X_B is the atom fraction of solute in the dispersed phase, $K(\phi)/K(0)$ is a volume fraction correction factor, ξ is a constant relating the average particle radius cubed to an intercept length cubed, and k and T have their usual meanings.

In this calculation, a particle-matrix interfacial energy of 1 J/m^2 is assumed. Values for the solid solubility and diffusivity of Fe and Ce in Al were taken from the literature (9-12). The available data lie in a range of temperatures which are somewhat higher than those used in this study. Therefore, it was necessary to extrapolate the solubility and diffusivity results to the temperatures used in the present work. Rate constants were calculated assuming dispersed phase compositions of Al_3Fe , $\text{Al}_{13}\text{Fe}_4$ and $\text{Al}_{12}\text{Fe}_2\text{Ce}$ where appropriate. In the calculations for the Al-Fe and Al-Fe-Mo-V alloys, use was made of the Brailsford and Wynblatt (13) volume fraction correction factor for the measured volume fraction dispersed phase. In the case of the Al-Fe-Ce alloys, the Brailsford and Wynblatt volume fraction correction factor was used for the predicted volume fraction of each dispersed phase since the measured volume fractions could not be separated into contributions

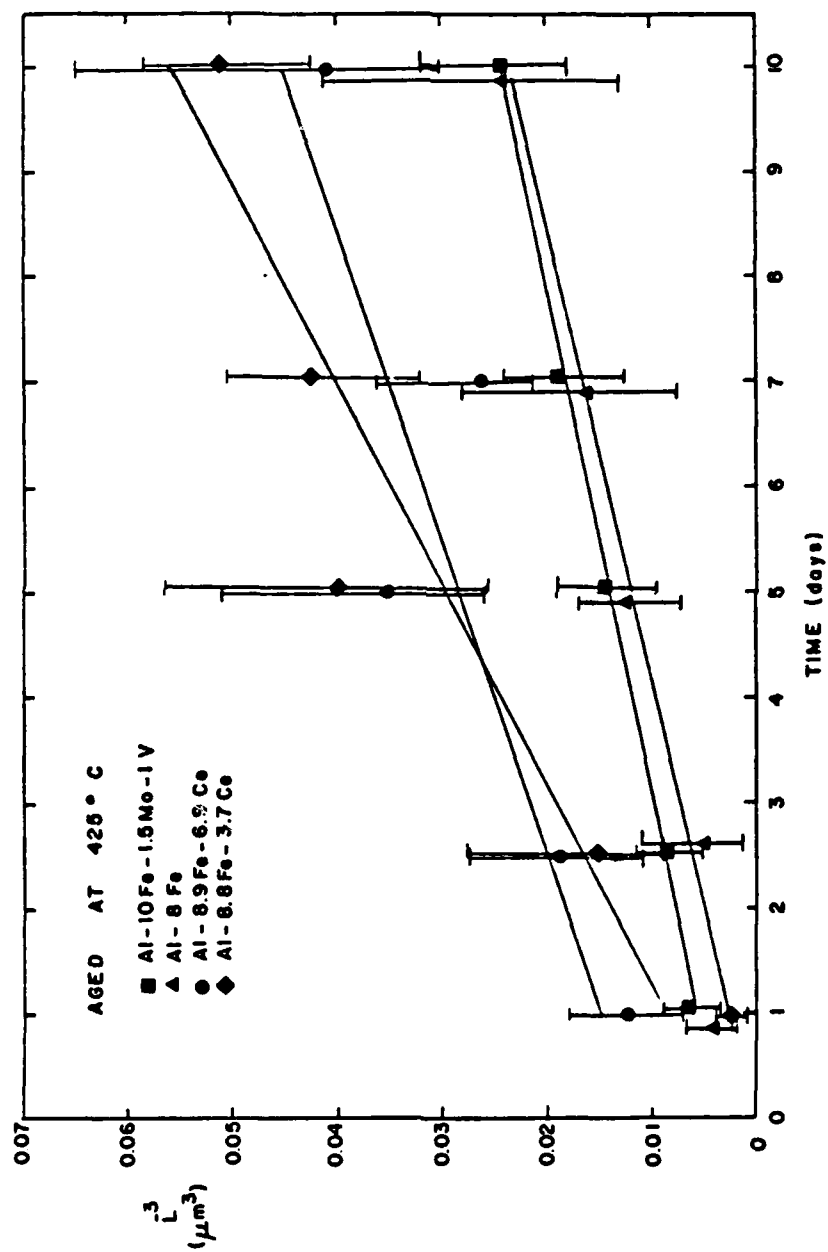


Fig. 13. Particle mean intercept length cubed, \bar{L}^3 , vs. aging time at 425°C.

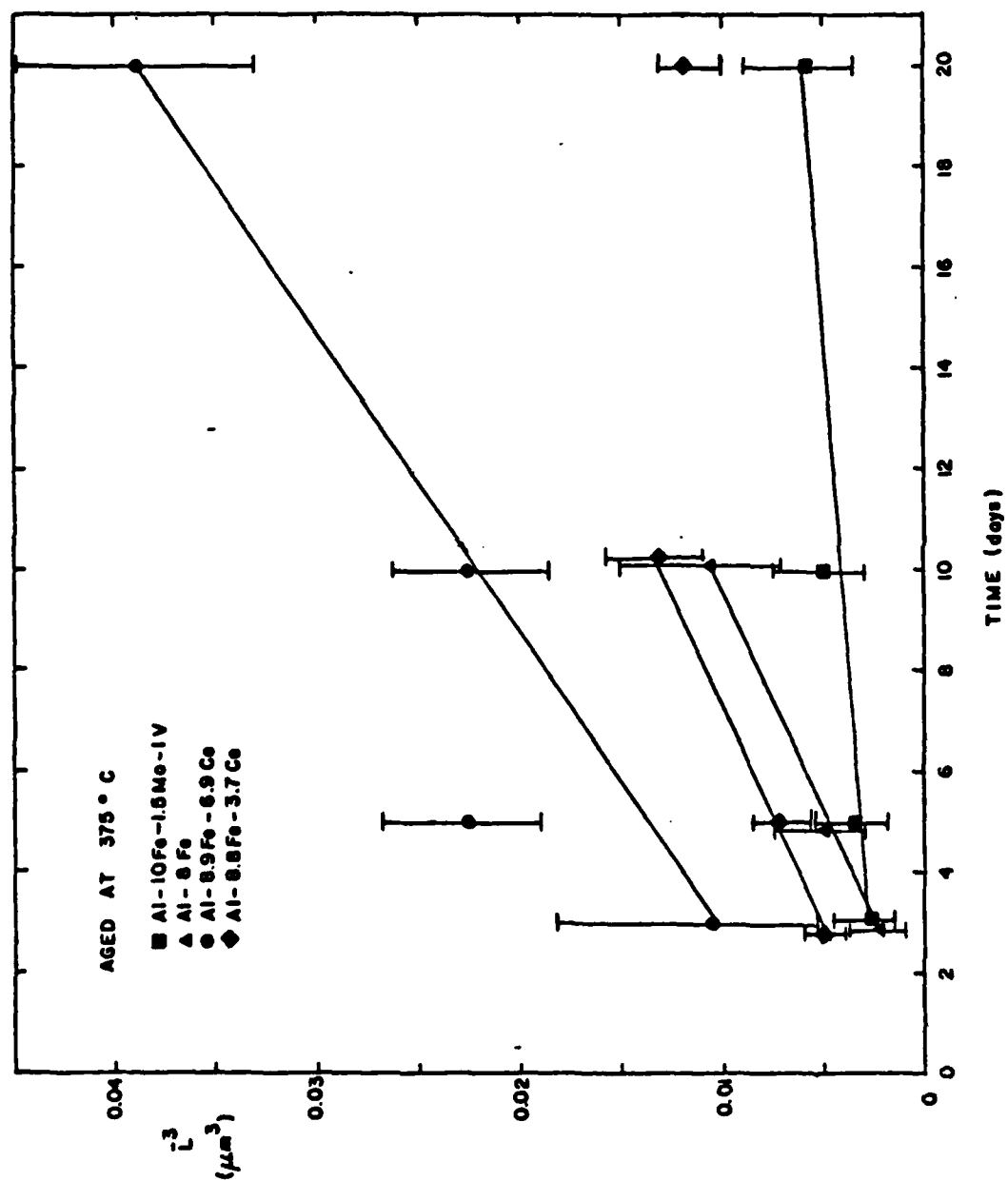


Fig. 14. Particle mean intercept length cubed, \bar{L}^3 , vs. aging time at 375° C.

Table 5. Comparison of Measured Particle Growth Rates and Growth Rates Predicted by the MLSW Theory for Alloys Aged at 375 and 425°C

Temperature (°C)	Alloy (wt. %)	K		K _{Al₆Fe}		K _{Al₁₃Fe₄}		K _{Al₁₀Fe₂Ce}	
		Measured ($\mu\text{m}^3/\text{hr}$)		Calculated ($\mu\text{m}^3/\text{hr}$)		Calculated ($\mu\text{m}^3/\text{hr}$)		Calculated ($\mu\text{m}^3/\text{hr}$)	
425	Al-8Fe	9.64×10^{-6}		-		1.47×10^{-6}		-	
425	Al-10Fe-1.5Mo-1V	8.69×10^{-5}		-		1.73×10^{-6}		-	
425	Al-8.8Fe-3.7Ce	2.20×10^{-4}		-		1.44×10^{-6}		8.00×10^{-10}	
425	Al-8.9Fe-6.9Ce	1.40×10^{-4}		-		1.12×10^{-6}		1.07×10^{-9}	
375	Al-8Fe	4.71×10^{-6}		1.22×10^{-7}		8.98×10^{-8}		-	
375	Al-10Fe-1.5Mo-1V	7.28×10^{-6}		1.35×10^{-7}		-		-	
375	Al-8.8Fe-3.7Ce	4.67×10^{-5}		-		7.09×10^{-8}		3.90×10^{-11}	
375	Al-8.9Fe-6.9Ce	5.95×10^{-5}		-		5.51×10^{-8}		5.20×10^{-11}	

from each phase.

In all cases, the measured rate constants were larger than the calculated values. The largest discrepancies occurred at the lower temperatures. Note that the predicted value of the rate constant for $\text{Al}_{10}\text{Fe}_2\text{Ce}$ growth is orders of magnitude smaller than that for $\text{Al}_{13}\text{Fe}_4$. From this result, one would expect to find small $\text{Al}_{10}\text{Fe}_2\text{Ce}$ particles and large $\text{Al}_{13}\text{Fe}_4$ particles in the Al-Fe-Ce alloys. As was stated in an earlier section, x-ray mapping on extracted particles did not show this trend; $\text{Al}_{10}\text{Fe}_2\text{Ce}$ particles were comparable in size to the $\text{Al}_{13}\text{Fe}_4$ particles. Additionally, one would expect a significantly slower growth rate of particles in the Al-8.9Fe-6.9Ce alloy as compared to the Al-8.8Fe-3.7Ce alloy since a much larger ratio of $\text{Al}_{10}\text{Fe}_2\text{Ce}$ to $\text{Al}_{13}\text{Fe}_4$ is predicted in the former alloy. Comparison of the measured rate constants for these two alloys at the two temperatures of this study did not show this effect. One explanation for the comparable growth rates for $\text{Al}_{10}\text{Fe}_2\text{Ce}$ and $\text{Al}_{13}\text{Fe}_4$ particles is that the reported value for Ce diffusivity in Al is incorrect; examination of the pre-exponential term shows an unreasonably small value. The measured rate constants may be compared for the four alloys. At 425°C , $K_{\text{Al-Fe-Mo-V}}^{\text{meas}} < K_{\text{Al-Fe}}^{\text{meas}} < K_{\text{Al-8.9Fe-6.9Ce}}^{\text{meas}} < K_{\text{Al-8.8Fe-3.7Ce}}^{\text{meas}}$. At 375°C , $K_{\text{Al-Fe-Mo-V}}^{\text{meas}}$ is much smaller than K^{meas} for the other three alloys. $K_{\text{Al-Fe}}^{\text{meas}}$, $K_{\text{Al-8.8Fe-3.7Ce}}^{\text{meas}}$ and $K_{\text{Al-8.9Fe-6.9Ce}}^{\text{meas}}$ are comparable.

Determination of an activation energy for the coarsening process was attempted for the Al-Fe-Ce and Al-Fe-Mo-V alloys. Plotted in Fig. 15 is $\ln K^{\text{meas}} T/C_0$ vs. $1/T$ for the measured rate constants presented here in addition to rate constants obtained earlier at higher temperatures. The slope of each line is given by $-Q/R$ where Q is the activation energy for the process and R is the gas constant. The figure actually shows a slightly larger activation energy for the Al-Fe-Ce alloys than for the Al-Fe-Mo-V (18.9 vs. 17.6 kcal/mole).

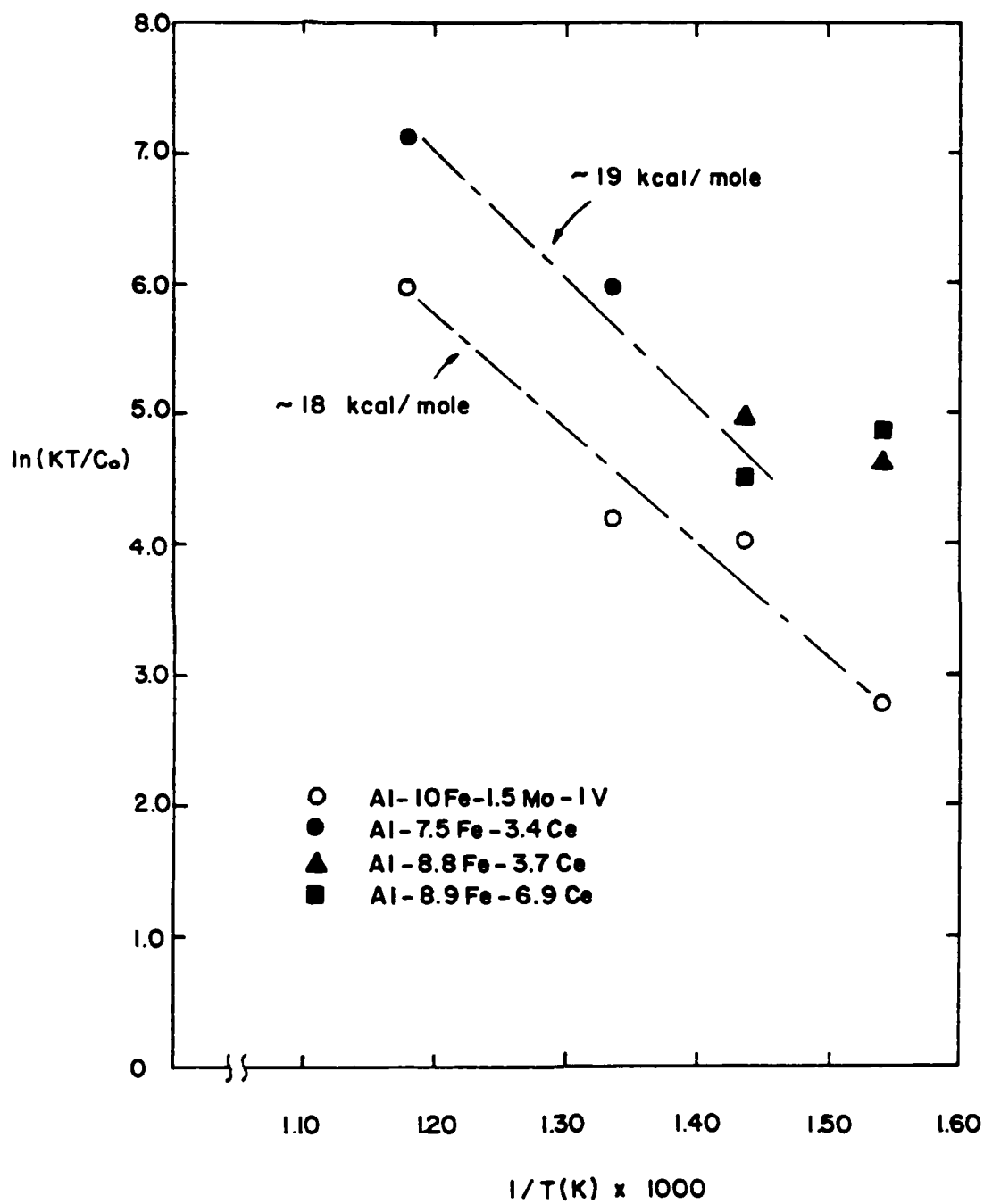


Fig. 15. Plot of $\ln \frac{KC_0}{T}$ vs. $1/T$ for aged Al-Fe-Mo-V and Al-Fe-Ce alloys.

(Note that the two Al-Fe-Ce points on the far right side of the figure have not been considered in the activation energy determination since the exponent, $n=3$, was clearly inappropriate at that temperature.) This would seem to suggest that since the activation energy is larger, the pre-exponential term in an effective diffusivity must also be larger for the Al-Fe-Ce alloys in order to achieve the faster coarsening kinetics. This term would be expected to be a strong function of the defect density of the material and therefore a strong function of alloy processing.

Since a larger value of the exponent n was appropriate for several of the alloys, particularly at the lower temperatures, rate constants based on the slope of an \bar{L}^3 vs. time plot have been calculated and are listed in Table 6 of the four alloys. Calculation of a rate constant predicted by Kreye's model for coarsening along dislocation lines requires knowledge of the number of dislocations attached to the particles, a quantity which was not determined in this study. It is possible then to compare only the relative magnitudes of the rate constants of the four alloys. At 425°C, $K_{\text{Al-Fe-Mo-V}}^{\text{meas}}$ and $K_{\text{Al-Fe}}^{\text{meas}}$ are comparable and much smaller than $K_{\text{Al-8.8Fe-3.7Ce}}^{\text{meas}}$ and $K_{\text{Al-8.9Fe-6.9Ce}}^{\text{meas}}$. At 375°C, $K_{\text{Al-Fe-Mo-V}}^{\text{meas}}$ is an order of magnitude smaller than the K^{meas} for the other alloys.

Grain size during 425°C aging of the Al-8.8Fe-3.7Ce alloy was approximated by counting intersections of grains with random test lines on projected TEM images. In Fig. 16, grain size vs. aging time at 425°C is plotted. After the first 24 hours of aging, grain size appears relatively constant. Having a measurement of grain size in the alloy allows one to calculate an expected rate of growth of particles by diffusion along grain boundaries as done by Pontikakos and Jones (14) in the Al-Fe alloy. Values for such parameters as grain boundary diffusion of Fe in Al, grain boundary

Table 6. Comparison of Coarsening Rate Constants in the RSP P/M Alloys for exponent, $n = 5$.

Temperature (°C)	Alloy Composition (wt. %)	Rate Constant ($\mu\text{m}^5/\text{hr}$)
425	Al-10Fe-1.5Mo-1V	8.64×10^{-8}
425	Al-8Fe	8.99×10^{-8}
425	Al-8.8Fe-3.7Ce	3.33×10^{-5}
425	Al-8.9Fe-6.9Ce	2.20×10^{-5}
375	Al-10Fe-1.5Mo-1V	3.23×10^{-7}
375	Al-8Fe	2.72×10^{-6}
375	Al-8.8Fe-3.7Ce	3.39×10^{-6}
375	Al-8.9Fe-6.9Ce	8.64×10^{-6}

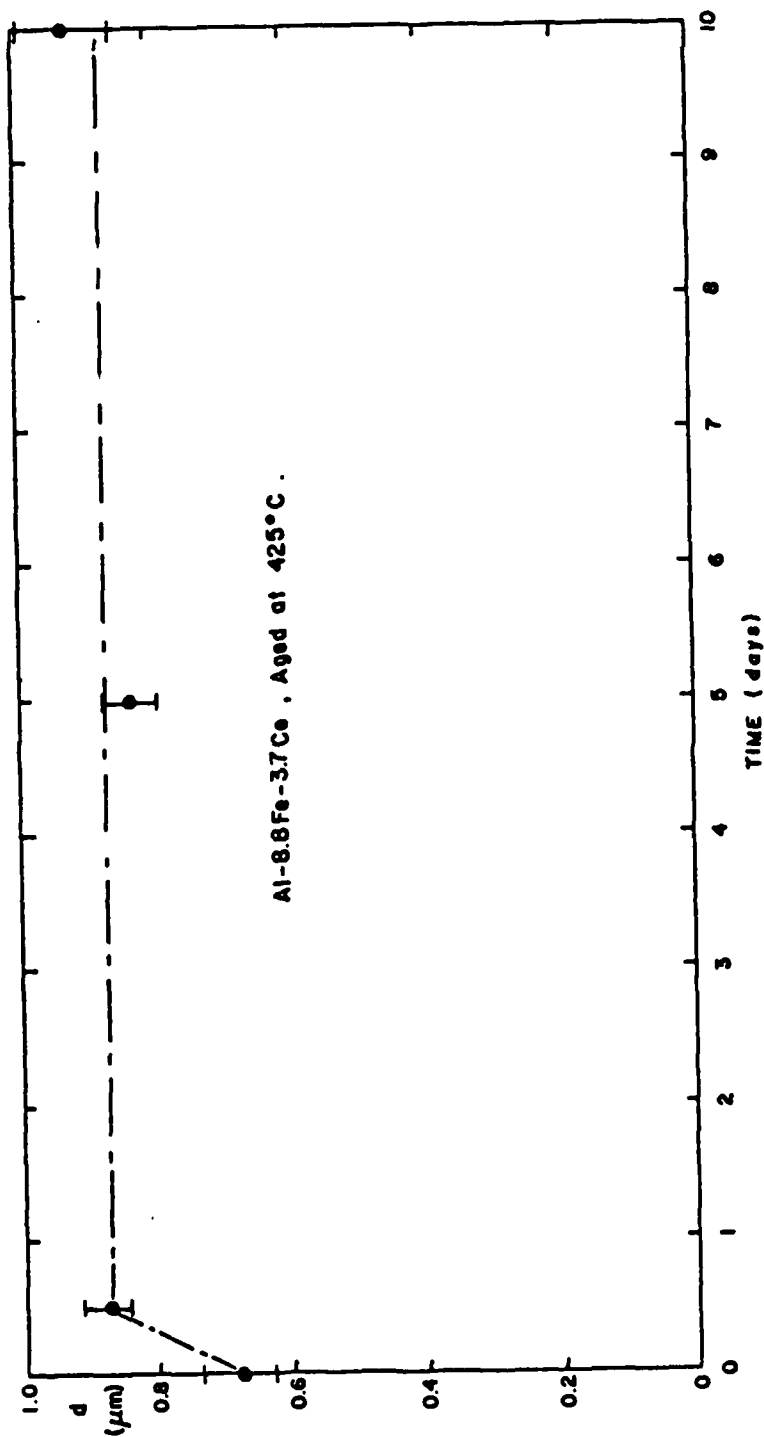


Fig. 16. Grain size vs. aging time at 425°C for the RSP P/M Al-8.8Fe-3.7Ce alloy.

width and the ratio of grain boundary energy to particle-matrix interfacial energy were chosen as in the Pontikakos and Jones study. A value for the fraction of grain boundary area covered by particles was approximated by assuming all particles lie on grain boundaries. This value is a function of time. Calculating the rate constant using values of the fraction at early and late times leads to $K^{\text{calc}} = 2.31 \times 10^{-4}$ to $.582 \times 10^{-4} \mu\text{m}^4/\text{hr}$. The experimental rate constant of $2.29 \times 10^{-4} \mu\text{m}^4/\text{hr}$ is consistent with the predicted value. To date, no measurements of grain size in the other alloys have been done so this calculation cannot be extended to the other alloys.

1.3. Effect of deformation on coarsening kinetics in the RSP P/M alloys

Preliminary creep experiments at 316 to 425°C reported earlier (1) had indicated that creep deformation enhances coarsening kinetics in the Al-8.8Fe-3.7Ce alloy. More recently, a series of specimens were crept at 425°C and at an initial stress of 17.2 MPa for varying lengths of time in order to quantify the degree of enhanced coarsening. The creep specimens were flat with gage section dimensions of 6 mm × 2.8 mm × 2 mm. Axial strain as monitored by an LVDT is plotted versus time in Fig. 17 for specimens crept at 425°C. Additionally, several specimens were fatigued in load control at 425°C with stress amplitudes of 34.4 or 68.8 MPa for varying lengths of time. Round threaded fatigue specimens had a gage diameter and gage length of 4.77 mm. Prior to testing, all specimens were polished to a 0.3 μm finish. After the tests, TEM micrographs of shadowed two-stage replicas of surfaces of sectioned samples were obtained for observation and subsequent quantitative metallography. Additionally, microhardness measurements for each specimen were taken using a 300 gram load with a Vickers hardness indenter.

Results of microhardness measurements for the series of specimens aged, crept or fatigued at 425°C are given in Fig. 18. The effect of imposed

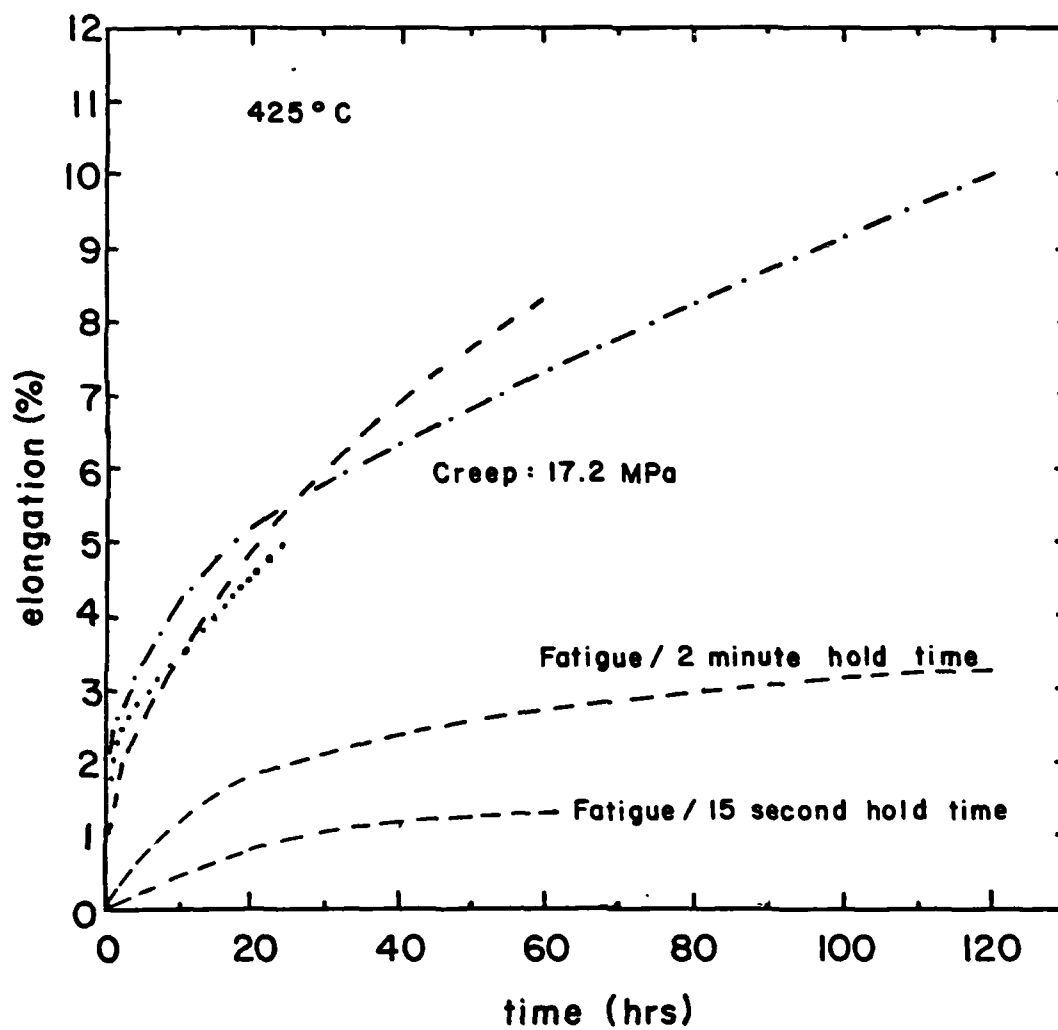


Fig. 17. Axial strain vs. time for Al-8.8Fe-3.7Ce specimens crept at 17.2 MPa.

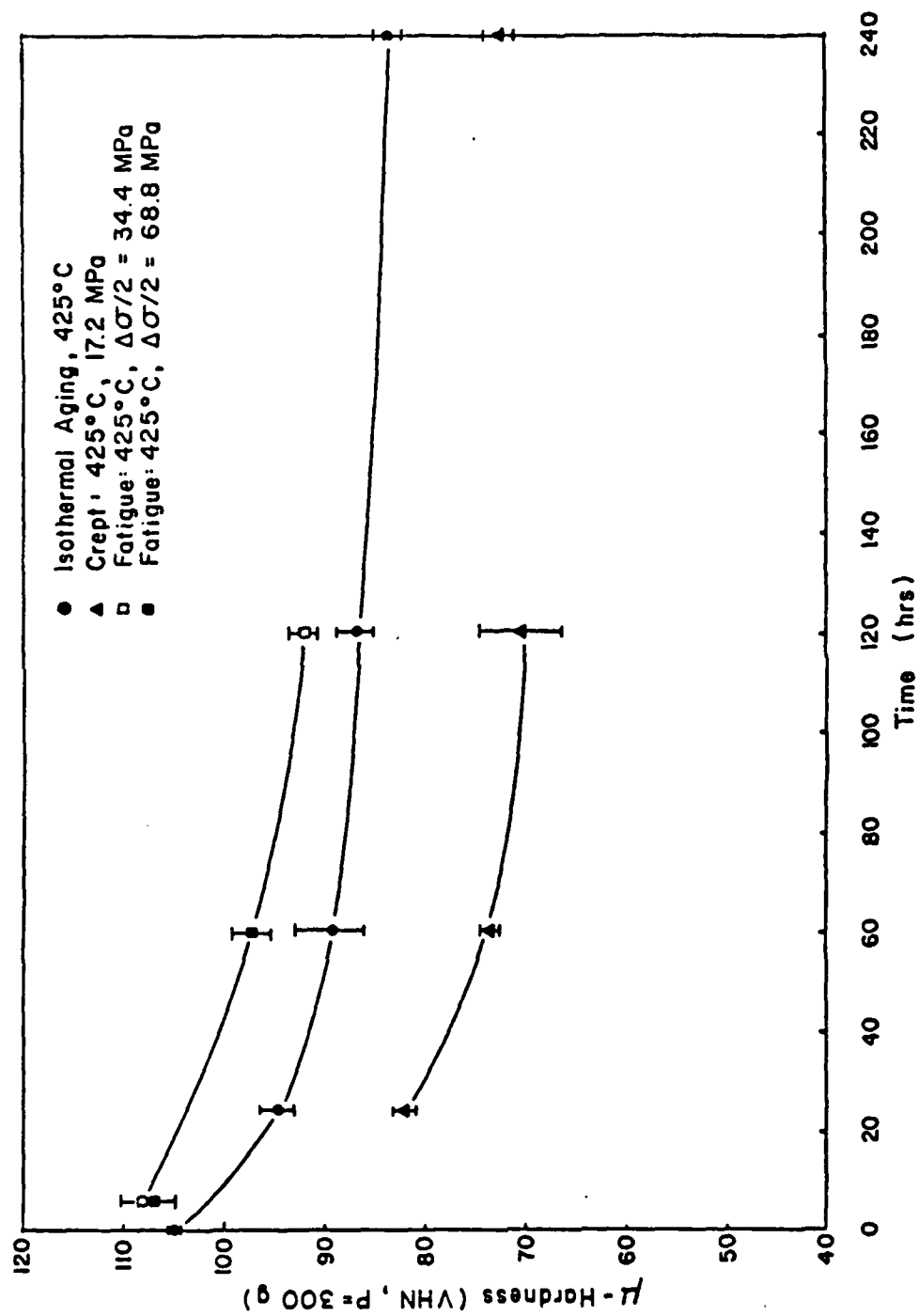
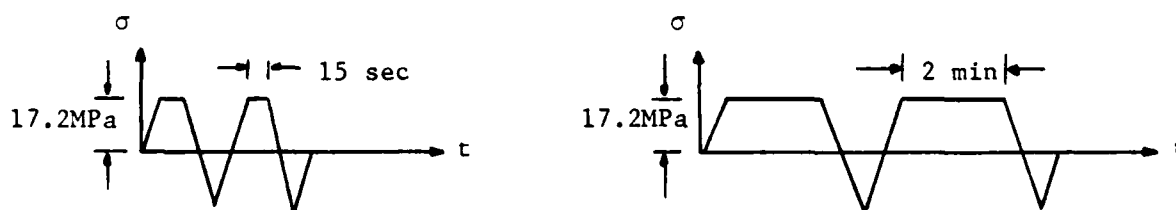


Fig. 18. Vickers microhardness vs. time for the isothermally annealed, crept or fatigued Al-8.8Fe-3.7Ce specimens.

creep on the Al-Fe-Ce alloy is to markedly soften the material in comparison to purely isothermal annealing. A somewhat smaller effect in the opposite sense is noted after fatigue loading. Figure 19 illustrates that the volume fraction of dispersed phases in the isothermally annealed, crept and fatigued specimens is constant with time at 425°C, as expected during coarsening.

The particle mean intercept lengths for specimens isothermally annealed, crept and fatigued at 425°C are tabulated in Table 7. Note that, in contrast to creep, the intercept lengths in fatigued specimens are somewhat smaller than those in specimens isothermally annealed for the same length of time. Since the use of the exponent $n=5$ leads to a good linear fit (see Fig. 12) for isothermal aging, results have been presented in Fig. 20 as \bar{L}^5 vs. time. The error bars of this figure are exacerbated by taking reasonable variations in intercept length to a fifth power. The slopes of the isothermal aging and creep data are $3.33 \times 10^{-5} \mu\text{m}^5/\text{hr}$ and $2.89 \times 10^{-4} \mu\text{m}^5/\text{hr}$, respectively.

Two specimens were fatigued 120 hours at 425°C with hold times to represent deformation intermediate to the extremes of creep and fatigue. The waveforms for these specimens are shown schematically below.



Net ratcheting of the fatigue curves, constructed by converting measured diametral strain to axial strain using a Poisson's ratio of 1/2, are included in Fig. 17. The particle mean intercept lengths in these specimens after 120 hours at 425°C are compared in Table 8 to mean intercept lengths in the crept specimen and the specimen fatigued without holding for the same length of time.

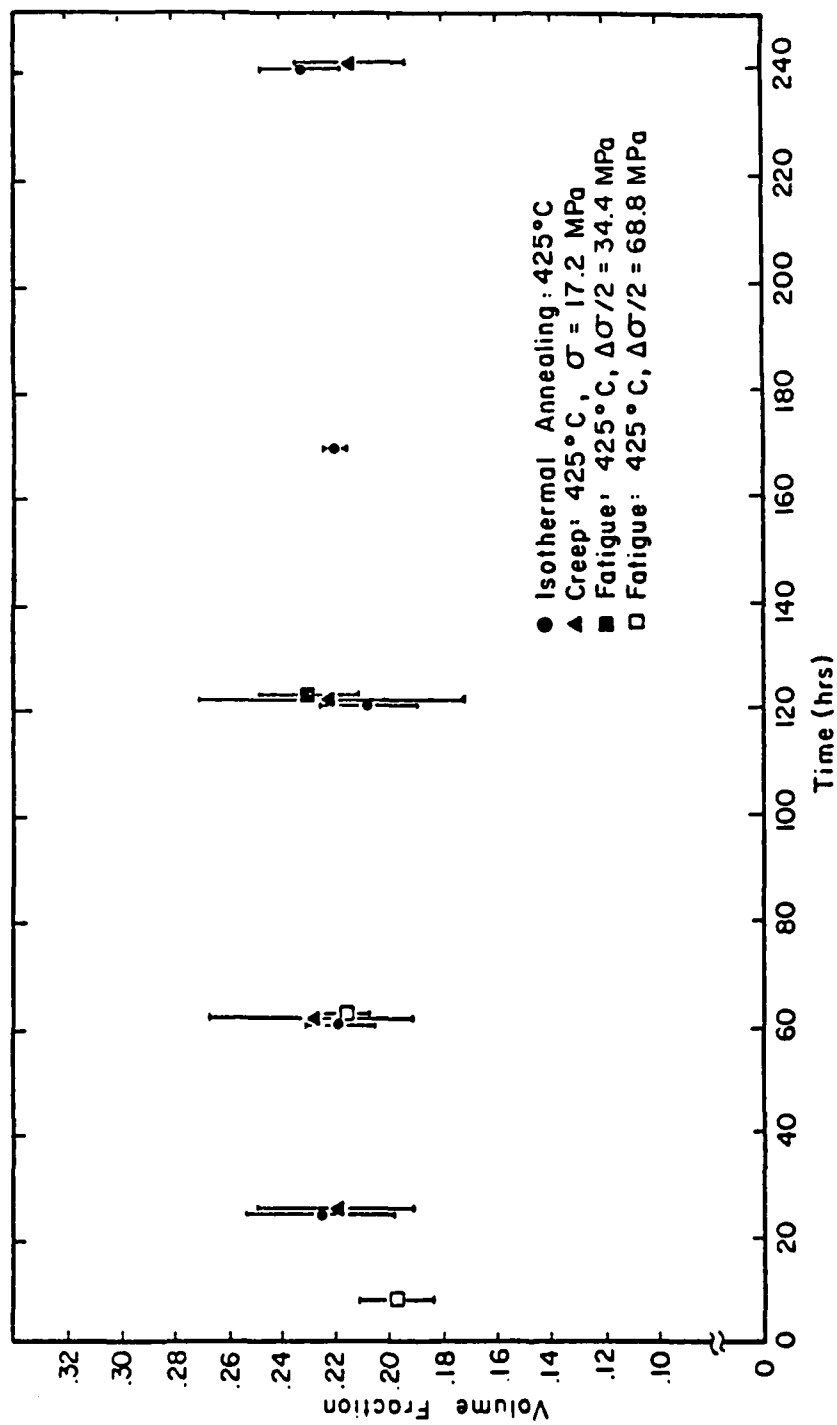


Fig. 19. Volume fraction dispersed phase vs. time for the isothermally annealed, crept and fatigued Al-8.8Fe-3.7Ce specimens.

Table 7. Values of Particle Mean Intercept Length in the
Al-8.8Fe-3.7Ce RSP Alloy after Isothermal Annealing,
Creep and Fatigue at 425°C

Time (hrs)	Mean Intercept Length* (μm)			
	Isothermal Annealing	Creep(17.2MPa)	Fatigue $\Delta\sigma/2 = 34.4\text{MPa}$	Fatigue $\Delta\sigma/2 = 68.8\text{MPa}$
6	-	-	-	$0.194 \pm .022$
24	$0.166 \pm .014$	$0.328 \pm .044$	-	-
60	$0.243 \pm .011$	$0.473 \pm .031$	-	$0.212 \pm .013$
120	$0.340 \pm .044$	$0.570 \pm .060$	$0.273 \pm .033$	-
168	$0.348 \pm .022$	-	-	-
240	$0.371 \pm .016$	$0.584 \pm .032$	-	-

* \pm refers to 95% confidence intervals about the mean value

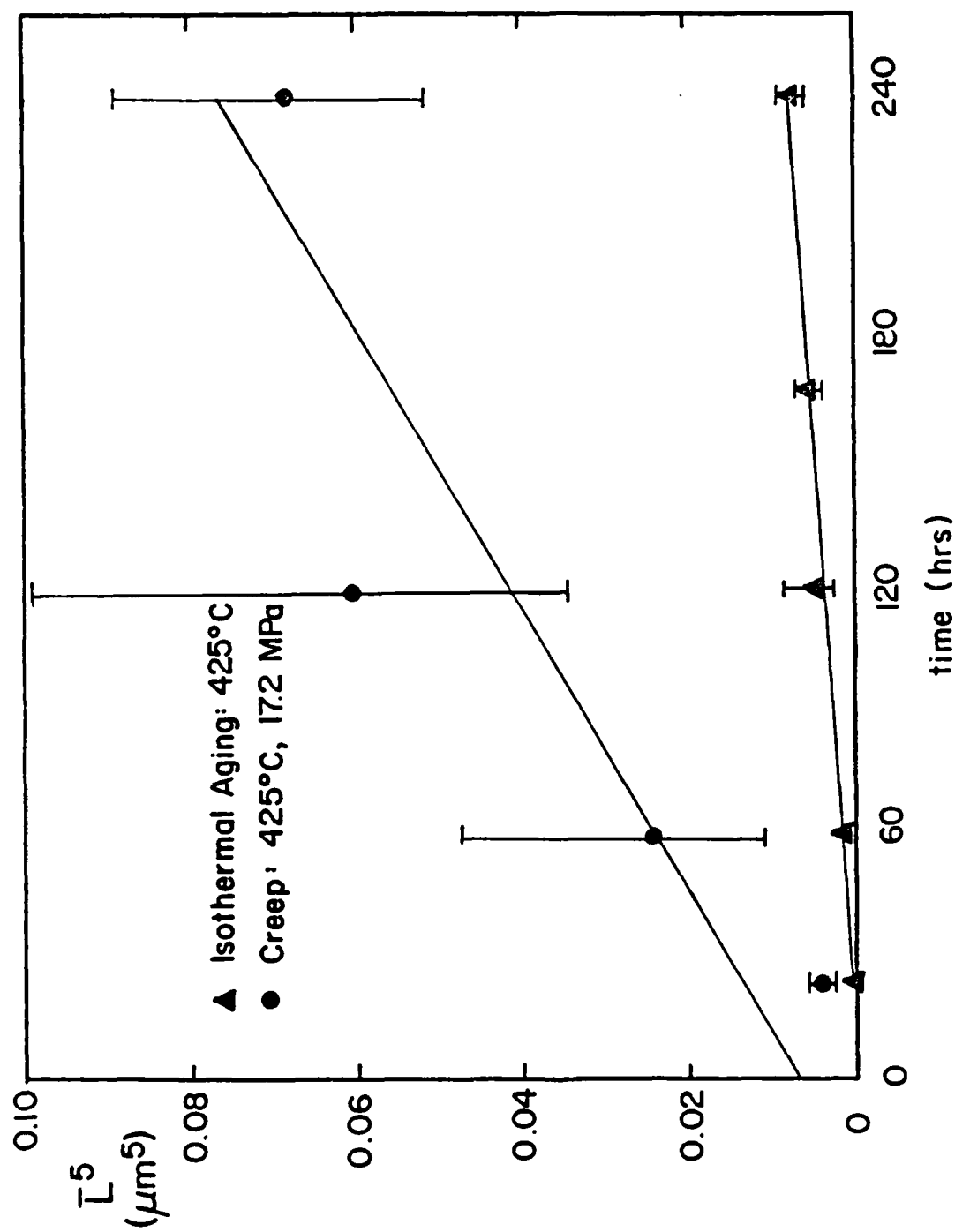


Fig. 20. Particle mean intercept length to a fifth power, L^5 , vs. time for the isothermally annealed, crept and fatigued Al-8.8Fe-3.7Ce specimens.

Table 8. Particle Mean Intercept Lengths in Specimens Deformed 120 Hours at 425 C.

Stress Amplitude (MPa)	Hold Time (s)	Particle Mean Intercept Length (μm)
34.4	0	0.23 ± 0.02
17.2	15	0.27 ± 0.02
17.2	120	0.32 ± 0.04
17.2	∞	0.57 ± 0.06

* \pm refers to 95% confidence intervals about the mean value

When comparing the kinetics noted in creep and fatigue, it is important to note that the strain rates are very different in the two deformation modes. Creep deformation of this study employed strain rates on the order of 10^{-8} s^{-1} . Fatigue deformation was carried out of strain rates in the 10^{-4} s^{-1} range.

Additional creep tests aimed at the determination of the strain rate sensitivity of the Al-8.8Fe-3.7Ce alloy were run at initial stresses of 25, 30 and 40 MPa at 425°C . In Fig. 21, the plot of $\ln \sigma$ vs. $\ln \dot{\epsilon}_{\min}$ leads to a measure of n , the power law exponent, of ~ 1.0 . This value of n is expected for the Nabarro-Herring diffusional creep mechanism.

The microstructure of crept and fatigued specimens were examined by TEM from two-stage replicas and from TEM thin foils. Figure 22a shows creep cavities present at a particle-matrix interface in an Al-8.8Fe-3.7Ce specimen crept 120 hours at 17.2 MPa and 425°C . Figure 22b shows creep cavities at nearly every particle in the field of view in a specimen crept to failure at 33.7 MPa and 425°C . Smaller cavities were noted in material fatigued at this temperature.

The TEM micrographs of thin foils of crept specimens (Fig. 23) show dislocations connecting the dispersed phase particles. Figure 23a was taken in material crept 96 hours at 25 MPa and 425°C . This micrograph indicates that dislocation pipe diffusion may play a significant role in the enhanced coarsening due to creep deformation, despite the fact that the strain rate sensitivity of unity indicates that dislocations should not play a major role in the creep process. In Fig. 23b, dislocations are seen forming a network within a grain of the material crept 120 hours at 35 MPa and 425°C .

Studies of the effect of prior cold work (CW) on coarsening kinetics were undertaken in the Al-8Fe, Al-8.8Fe-3.7Ce and Al-8.9Fe-6.9Ce alloys.

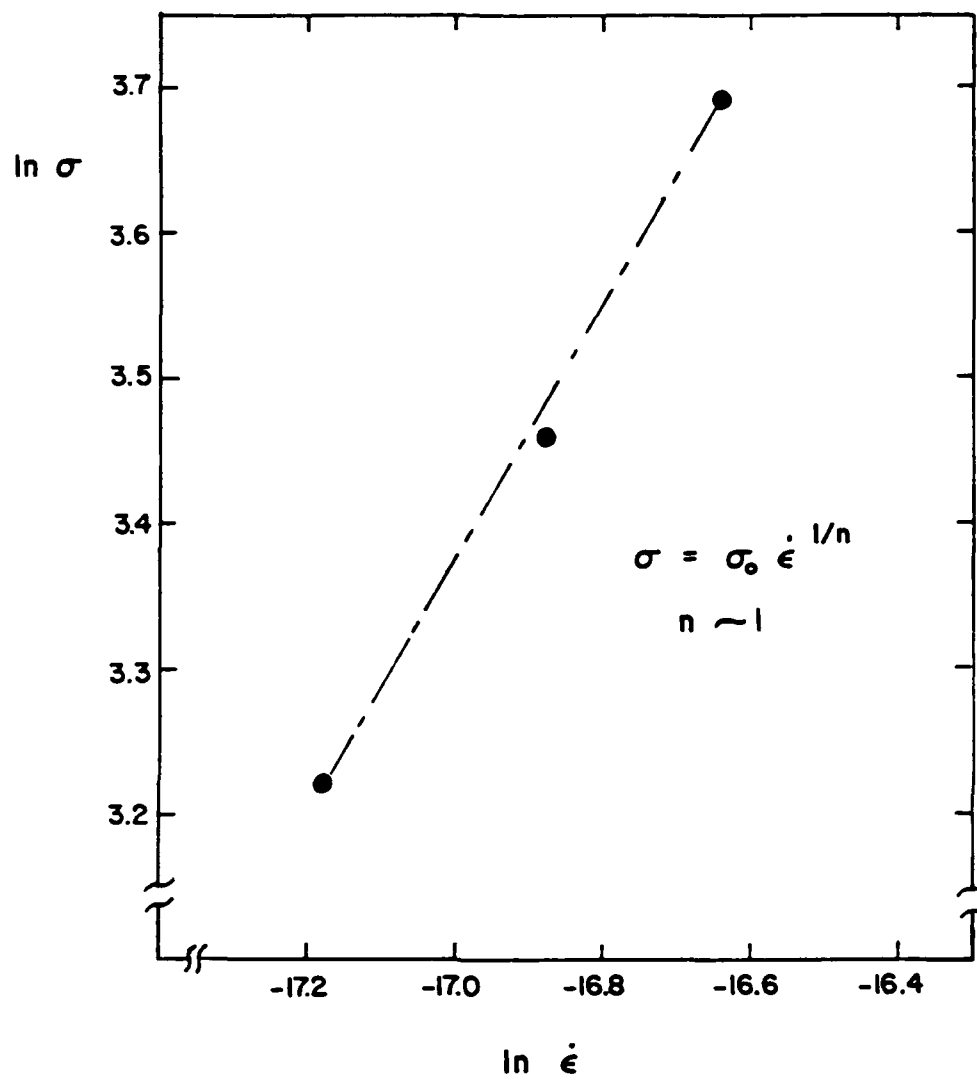
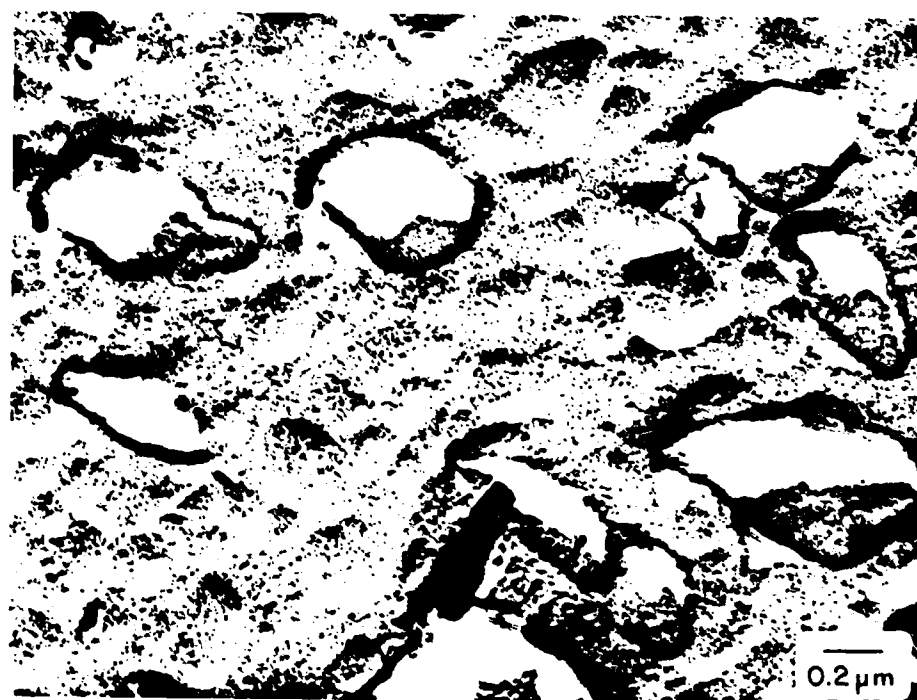


Fig. 21. Plot of $\ln \sigma$ vs. $\ln \dot{\epsilon}$ for Al-8.8Fe-3.7Ce specimens crept at 425°C.

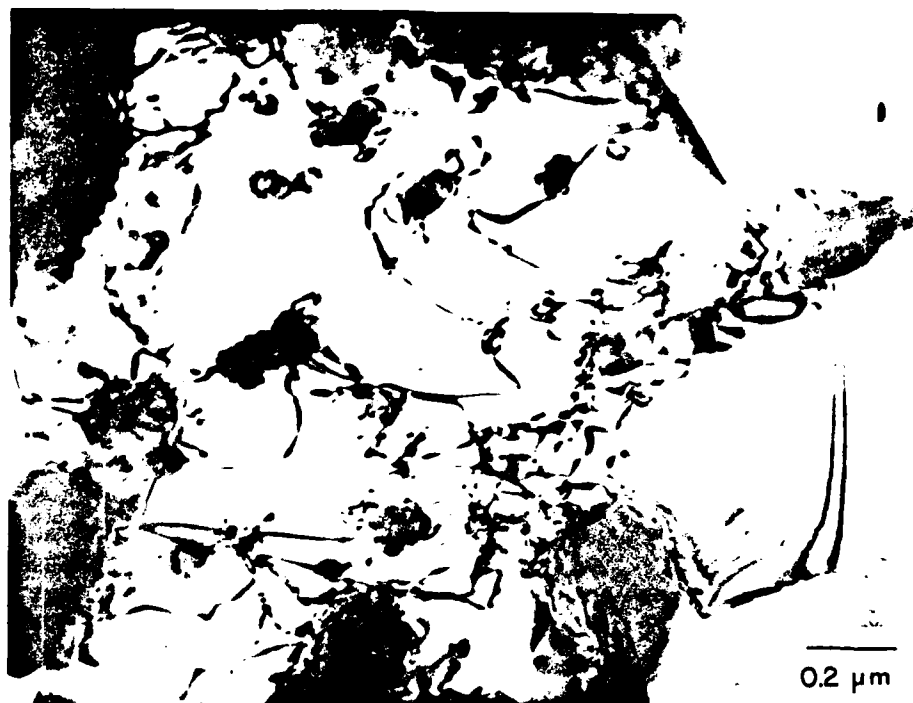


(a)

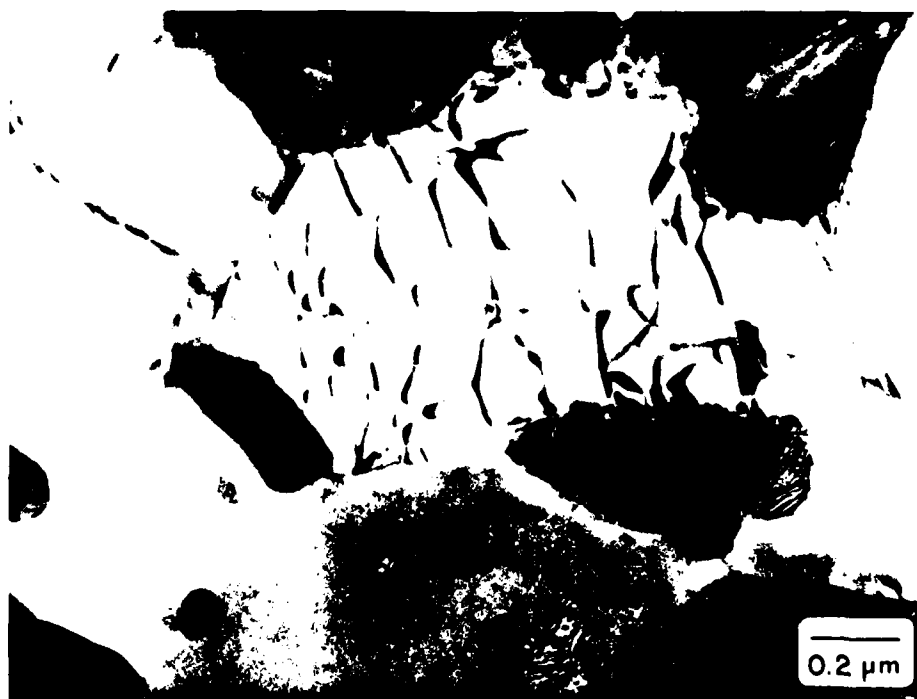


(b)

Fig. 22. Creep cavitation in Al-8.8Fe-3.7Ce specimens:
a) crept 120 hours at 17.2 MPa, 425°C and b)
crept to failure at 33.7 MPa, 425°C.



(a)



(b)

Fig. 23. TEM micrographs of thin foils of crept Al-8.8Fe-3.7Ce specimens showing dislocation structures typically observed: a) after 96 hours at 25 MPa, 425°C, b) 120 hours at 35 MPa, 425°C.

Samples of each material were first isothermally annealed at 575°C for 2 hours. Half of these samples were then cold rolled 66% and all samples were isothermally annealed at 425°C for various lengths of time. Vickers microhardness measurements on these specimens are compared to specimens isothermally annealed at 425°C without any prior treatment in Fig. 24a through c. Volume fraction measurements and \bar{L}^3 have been plotted as a function of time in Figs. 25 and 26.

Studying the kinetics in specimens aged 2 hours at 575°C prior to aging at 425°C were meant to represent kinetic behavior at longer times. For the three alloys considered, Fig. 26 shows that growth has been slowed down by the prior heat treatment. Introduction of 66% CW was intended to increase the defect density of the material, thereby increasing the coarsening kinetics over those in the material that was not cold worked. This effect is seen in the Al-8Fe alloy. In the Al-8.8Fe-3.7Ce alloy, the kinetics are even slower after cold working than without cold working, indicating that the material may have recrystallized and grains have grown. Effects of short circuit diffusion along grain boundaries would then be reduced.

1.4. Study of dilute Al-Fe alloys

Alloys of nominal compositions Al-0.1% Fe and Al-0.04% Fe were prepared by arc melting high purity Al and Fe in an argon atmosphere. Pieces of the alloys were aged at 375°C or 425°C; some were cold rolled 90% prior to aging. Two results were noted from this study. The morphology of the particles first to nucleate in the aged alloy was needle-like; particles nucleating in the material which had been cold worked before aging had a more equiaxed morphology. This difference is illustrated in Fig. 27 where the microstructure of the Al-0.04Fe alloy aged 425°C for 60 hours and of the alloy cold rolled 90% and then aged 60 hours at 425°C is shown. In addition, it was

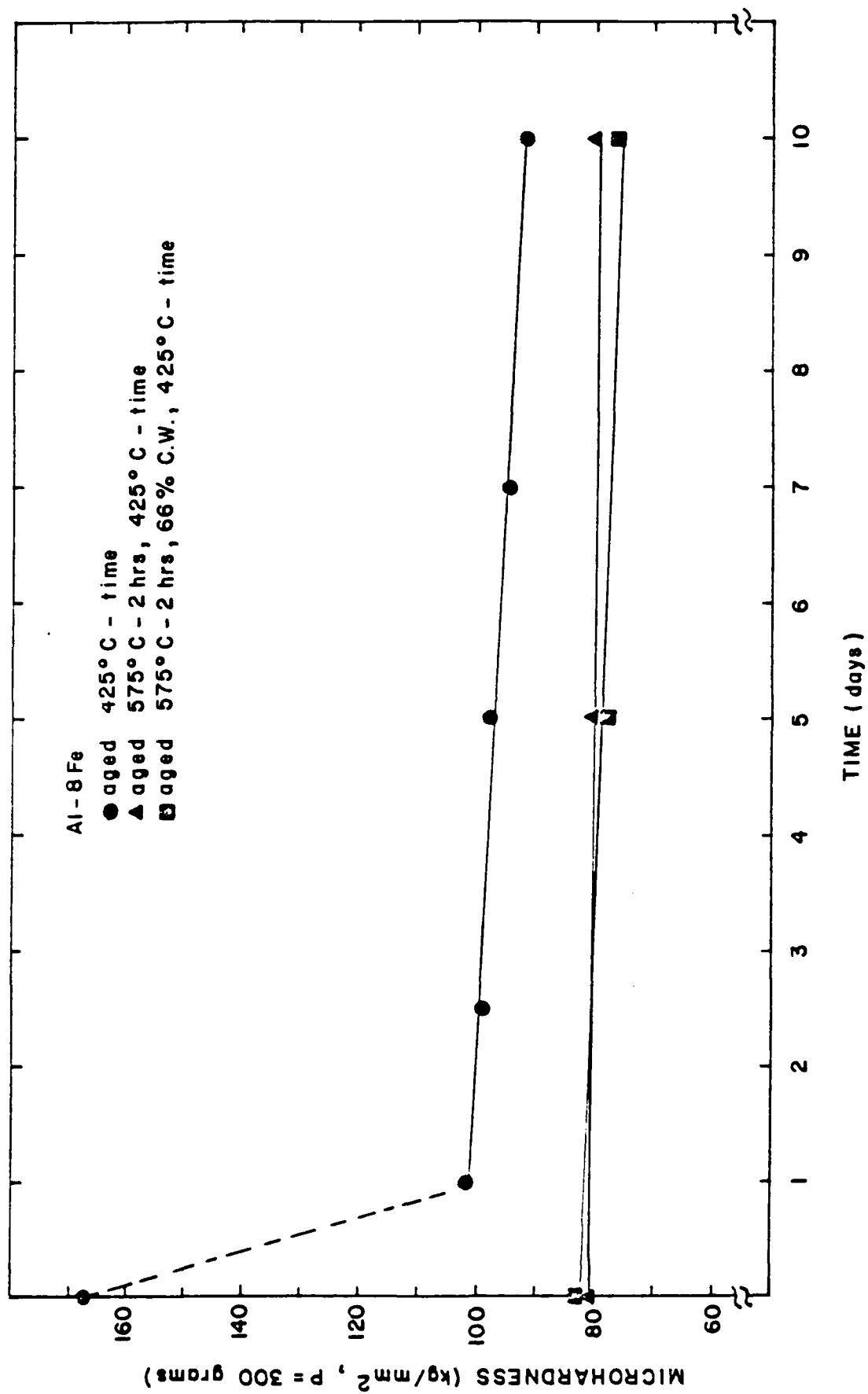


Fig. 24(a). Vickers microhardness vs. time for isothermal aging at 425°C with and without prior treatment for Al-8Fe.

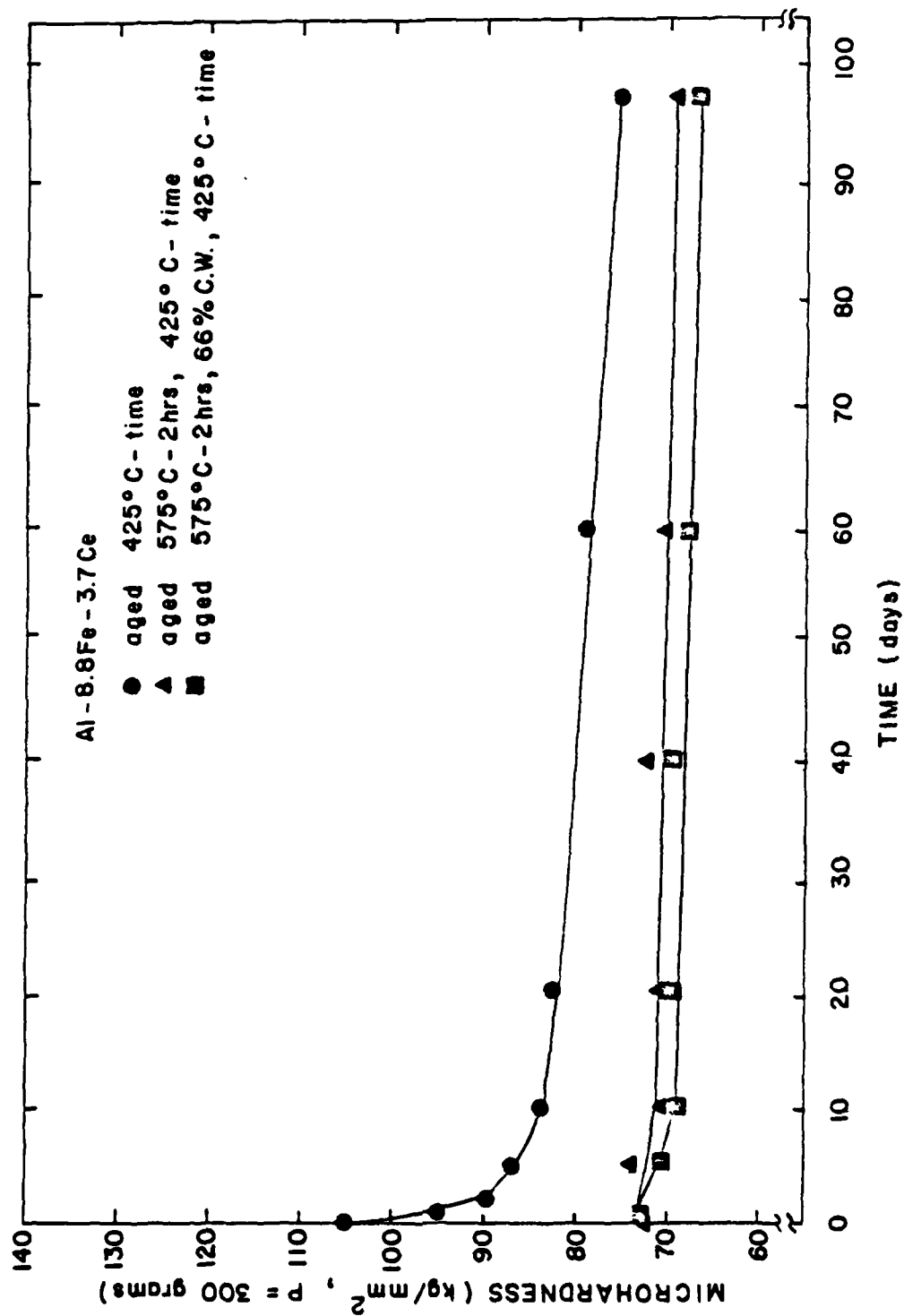


Fig. 24(b). Vickers microhardness vs. time for isothermal aging at 425°C with and without prior treatment for Al-8.8Fe-3.7Ce.

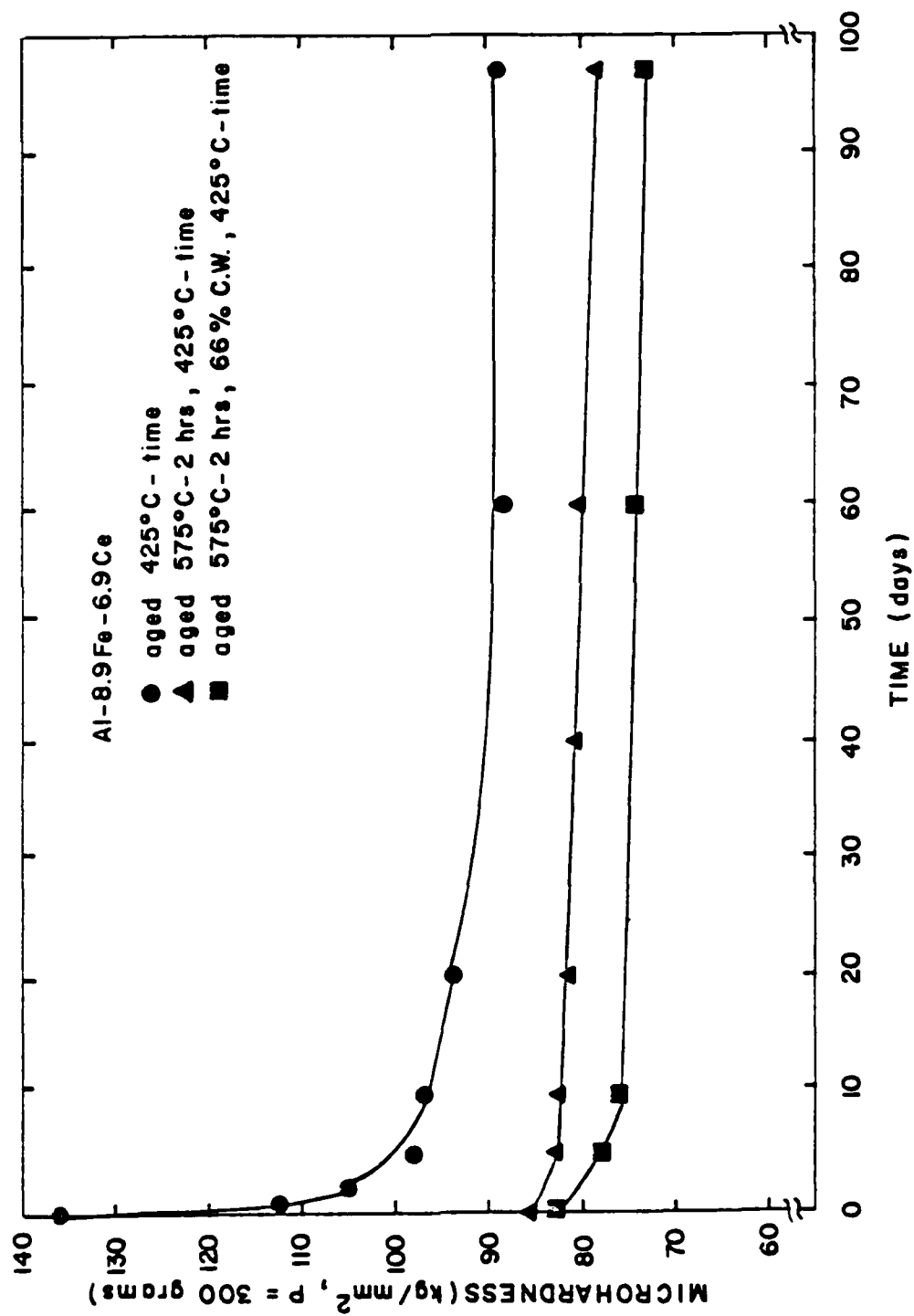


Fig. 24(c). Vickers microhardness vs. time for isothermal aging at 425°C with and without prior treatment for Al-8.9Fe-6.9Ce.

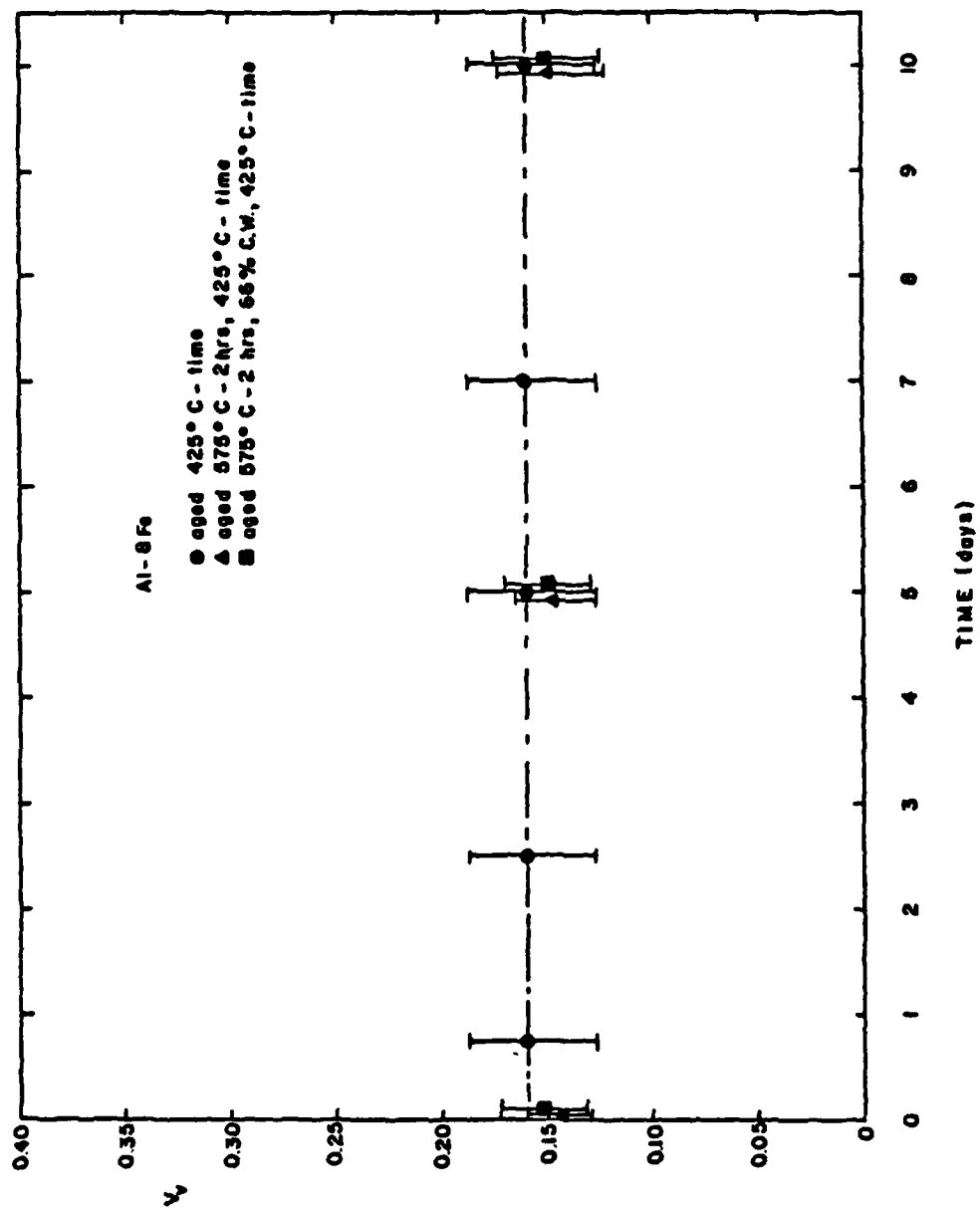


Fig. 25(a). Volume fraction dispersed phase vs. time for isothermal aging at 425° C with and without prior treatment for Al-8Fe.

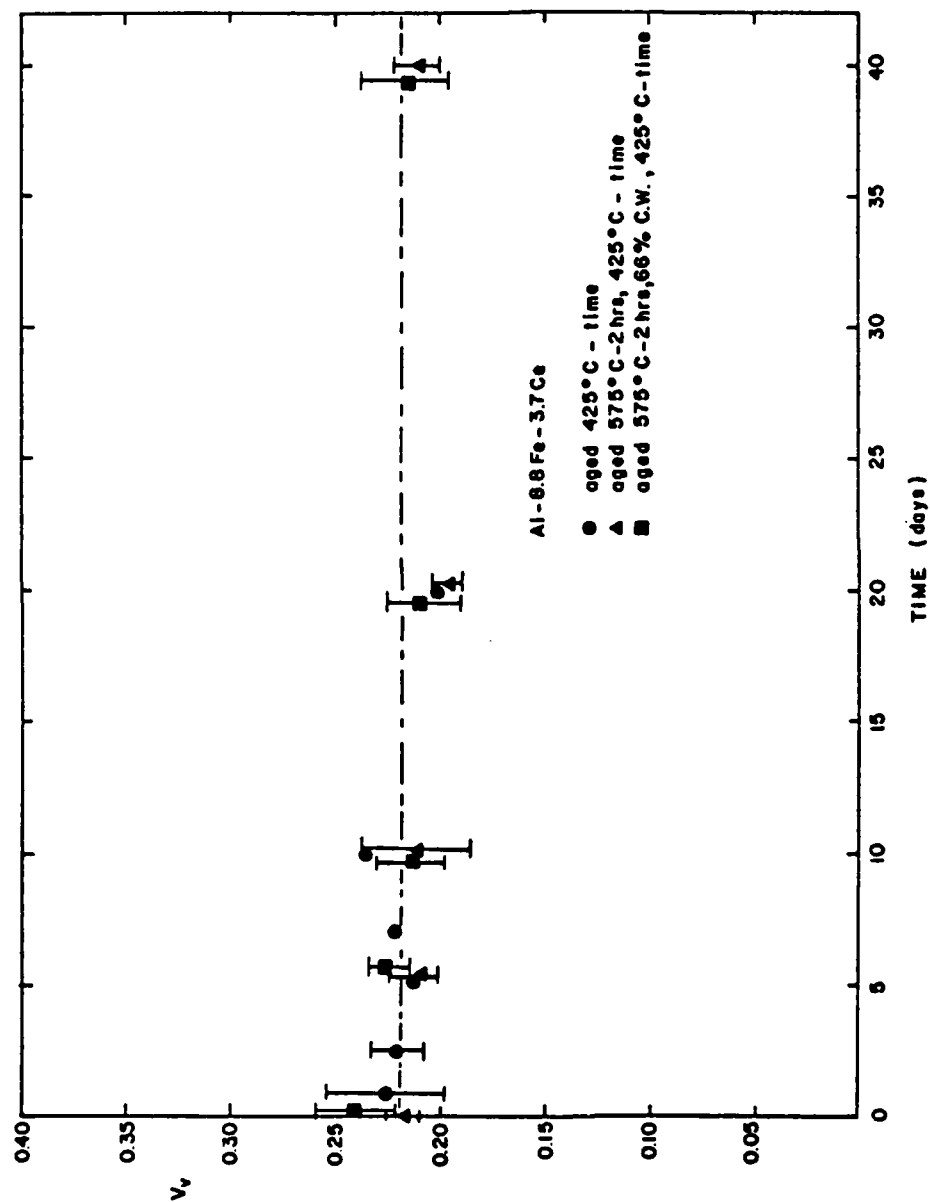


Fig. 25(b). Volume fraction dispersed phase vs. time for isothermal aging at 425°C with and without prior treatment for Al-8.8Fe-3.7Ce.

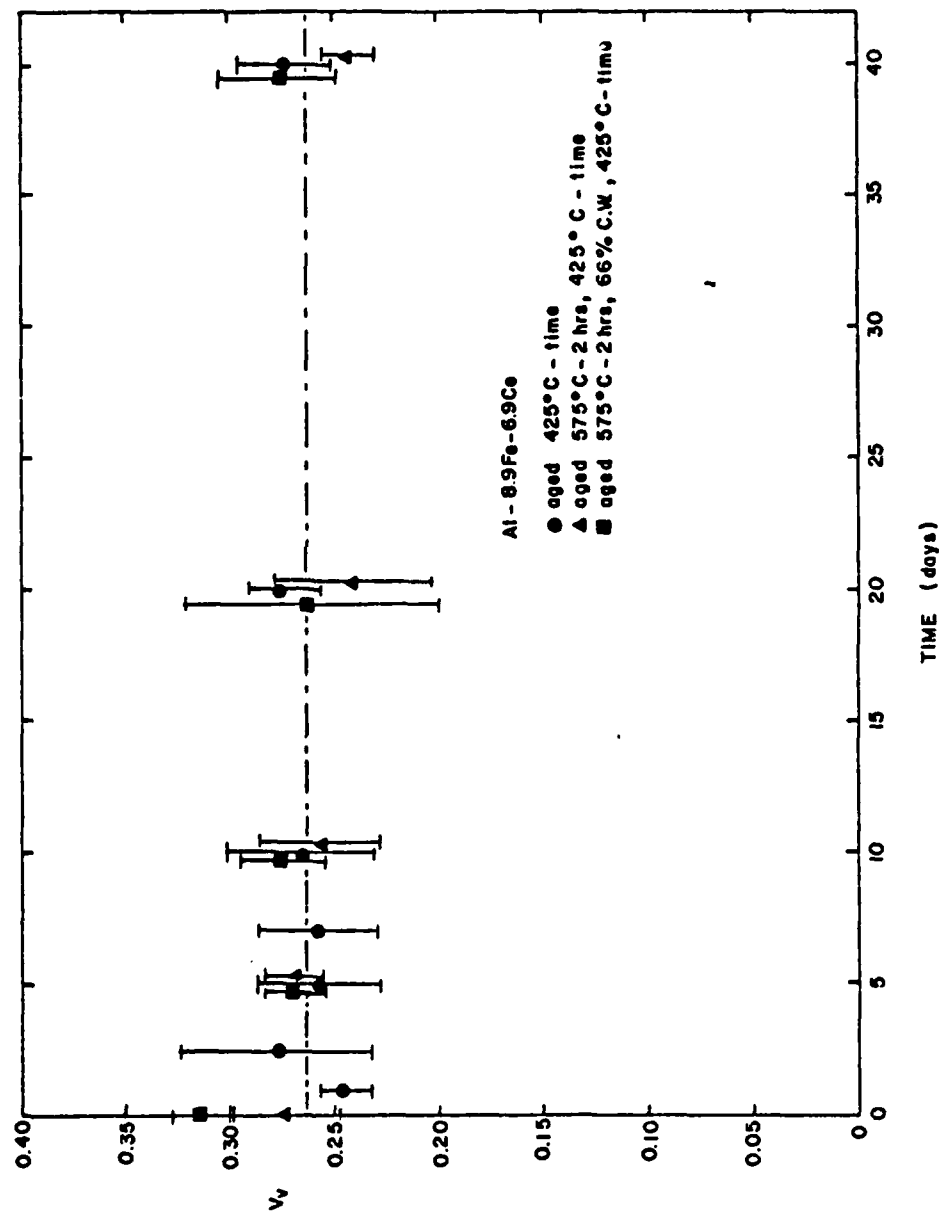


Fig. 25(c). Volume fraction dispersed phase vs. time for isothermal aging at 425°C with and without prior treatment for Al-8.9Fe-6.9Ce.

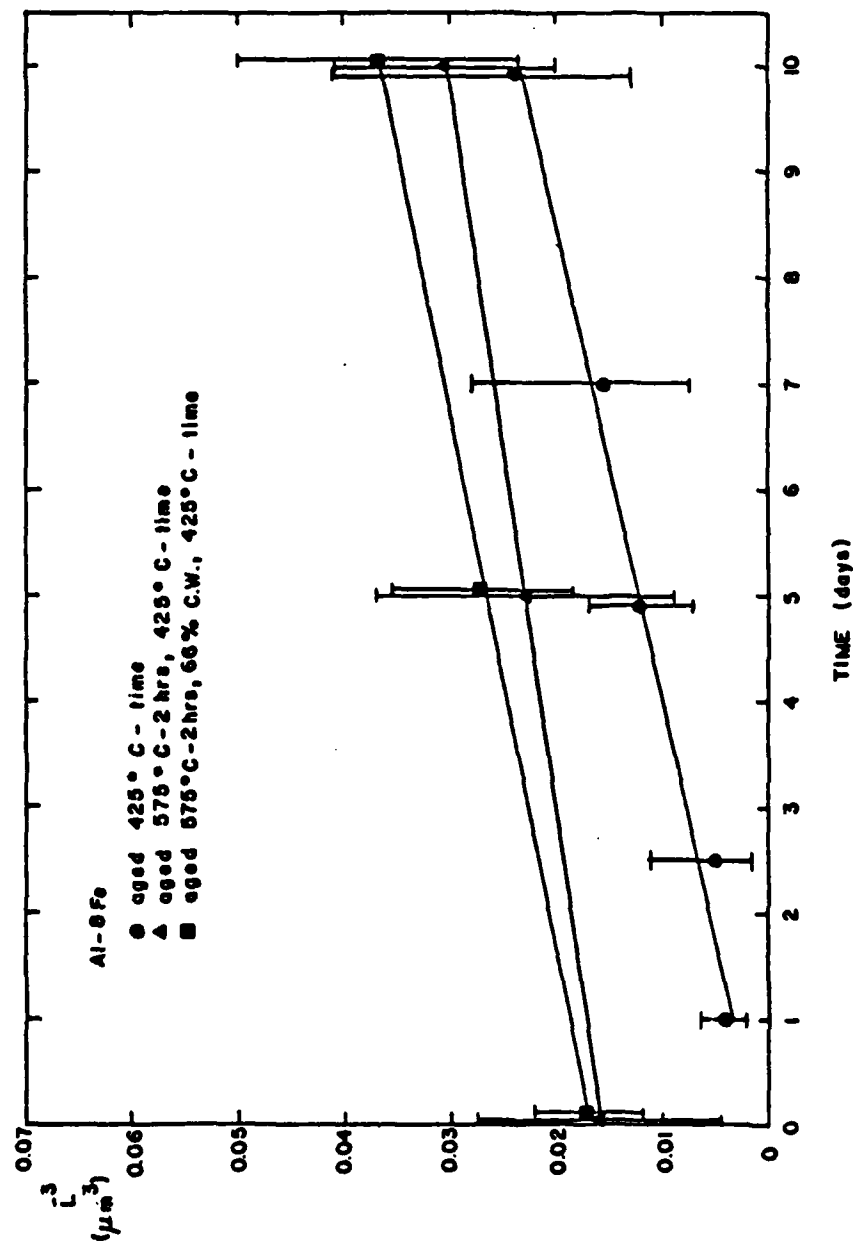


Fig. 26(a). Particle mean intercept length cubed, L^3 , vs. time for isothermal aging at 425°C with and without prior treatment for Al-8Fe.

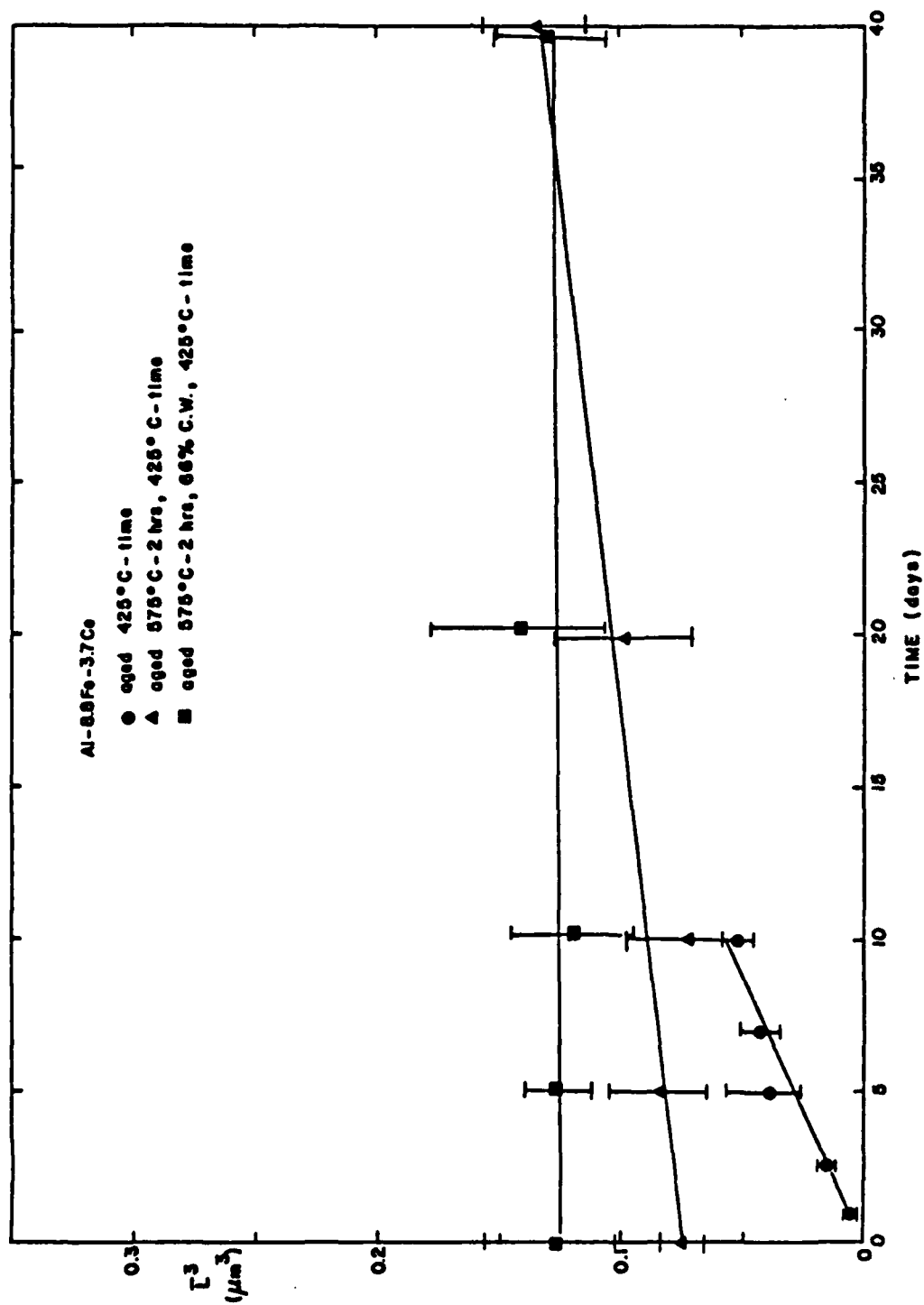


Fig. 26(b). Particle mean intercept length cubed, \bar{L}^3 , vs. time for isothermal aging at 425°C with and without prior treatment for Al-8.8Fe-3.7Ce.

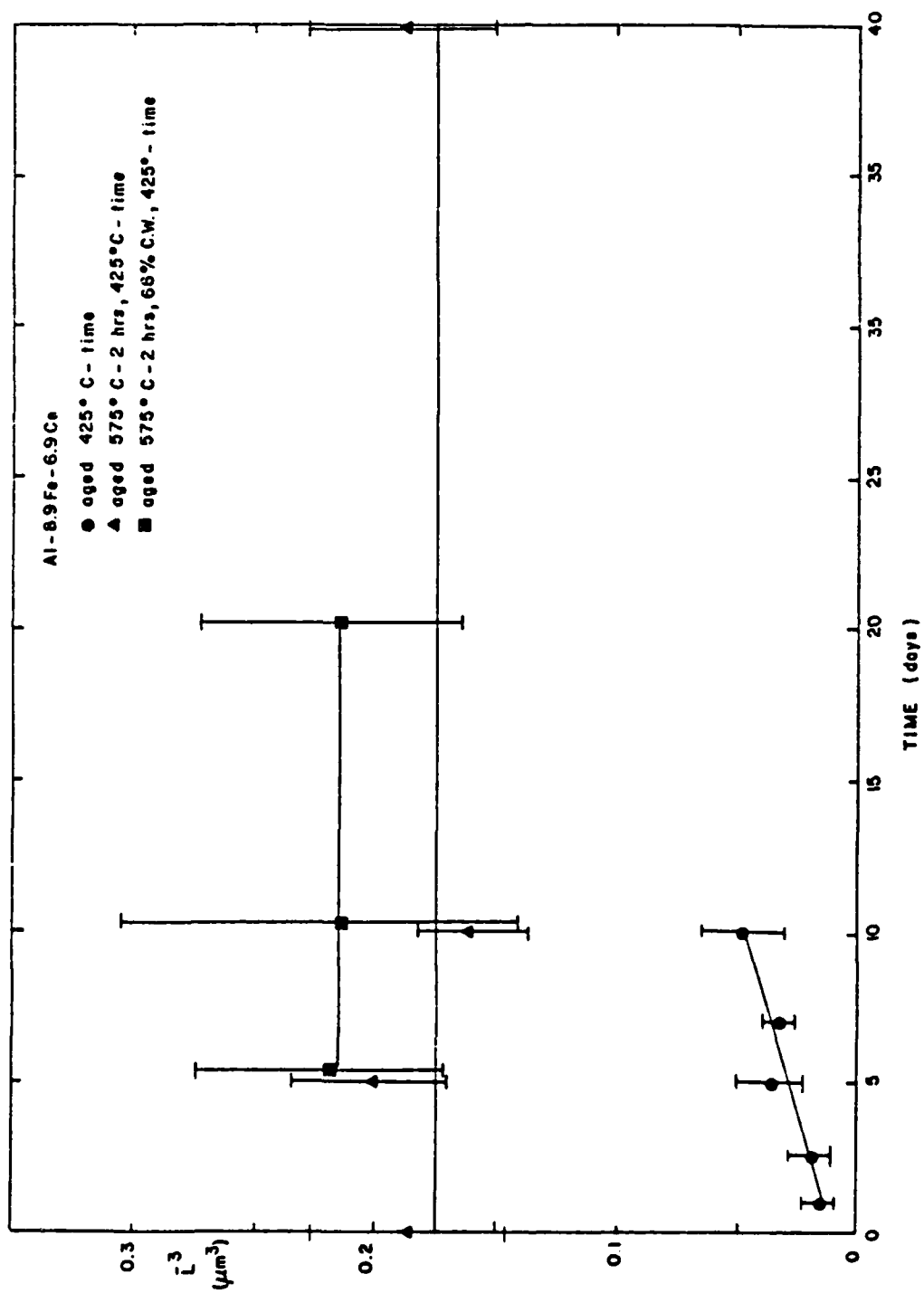
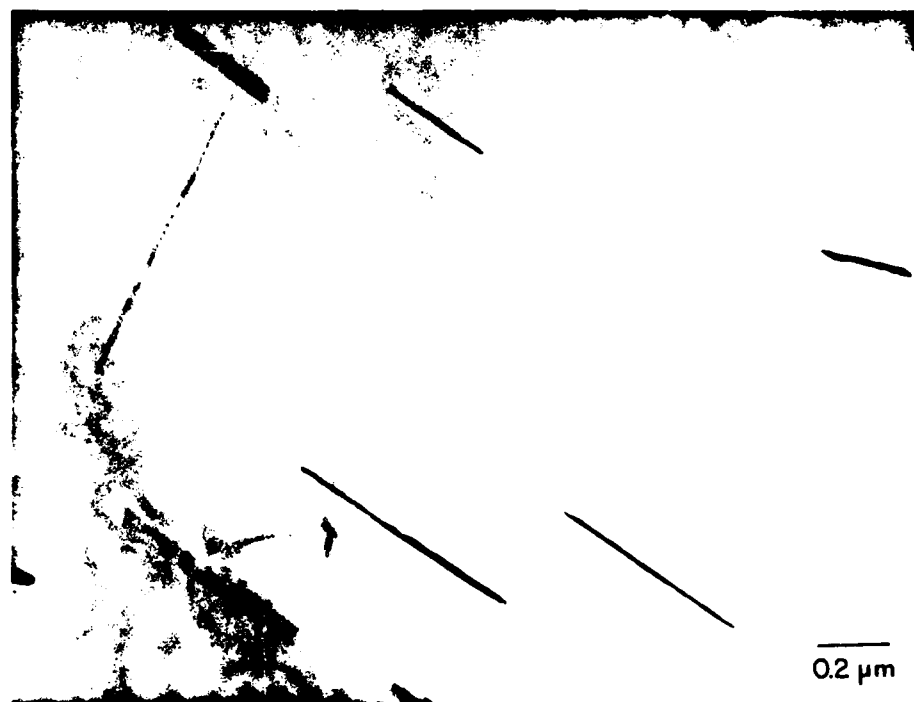


Fig. 26(c). Particle mean intercept length cubed, \bar{L}^3 , vs. time for isothermal aging at 425° C with and without prior treatment for Al-8.9Fe-6.9Ce.



(a)



(b)

Fig. 27. TEM micrographs of thin foils of Al-0.04Fe: a) aged 60 hours at 425°C and b) cold rolled 90% and aged to hours at 425°C.

noted that precipitation occurred in much shorter times in material which was first cold rolled than in material which was only aged.

References

1. Air Force Progress Report 1982-1983.
2. P. J. Black, *Acta. Crystall.* 8, 175 (1955).
3. O. S. Zarechnyuk and P. I. Kripyahevich, *Sov. Phys.- Crystallography* 7, No. 4, 436 (1963).
4. F. H. Cocks, M. L. Shepard and H. G. Chilton, *J. Mat. Sci.* 12, 494 (1977).
5. I. M. Lifshitz and V. V. Slyozov, *Phys. Chem. Solids* 19, 35 (1961).
6. C. Wagner, *Z. Electrochem.* 65, 581 (1961).
7. H. O. K. Kirchner, *Metall. Trans.* 2, 2861 (1971).
8. H. Kreye, *Z. Metallkde.* 61, 108 (1970).
9. *Metallurgy and Phase Diagrams*, American Society for Metals, 1967, p. 362.
10. L. F. Mondolfo in Aluminum: Structure and Properties, Butterworths, London-Boston, 1976, p. 242.
11. K. Soronson and G. Trumpy, *Phys. Rev. B1*, vol. 7, 1791 (1973).
12. S. P. Murarka and R. P. Agarwala, Indian Atomic Energy Commission Rept. BARC-368, 1968.
13. A. D. Brailsford and P. Wynblatt, *Acta Metall.* 27, 489 (1979).
14. I. Pontikakos and H. Jones, *Metal Science* 16, 27 (1982).

2. Effect of Lattice Disregistry on the Decomposition and Coarsening Kinetics of the $Al_3(V,Zr)$ Phase in Supersaturated Al - V - Zr Alloys

With the recent advances in powder metallurgy and rapid solidification technology, the development of an aluminum base alloy suitable for elevated temperature applications above $375^\circ C$ seems possible. Such a development is dependent on the thermodynamic stability and physical makeup of the strengthening dispersed phases. As is true for γ' in the Ni-base systems, for very high temperature Al alloys suitable dispersed phases must be thermodynamically stable at temperatures of interest, coherent with the matrix and the solutes must have low solubilities in the Al solid solution matrix. If minimum lattice disregistry exists across the precipitate/matrix boundary, then a low interfacial energy, σ , is expected to exist, and thus, a low driving force for Ostwald ripening.

As predicted by the Lifshitz-Slyozov-Wagner (LSW) theory of Ostwald ripening (1,2), assuming diffusion controlled coarsening, the average precipitate size should increase in accordance to the relationship:

$$\bar{r}^3 - \bar{r}_0^3 = k(t - t_0) \quad (1)$$

where \bar{r} is the average particle radius at time t , \bar{r}_0 is the extrapolated value corresponding to t_0 , and k represents the rate constant given by:

$$k = \frac{8\sigma DC_0 V_m^2}{\nu RT} \quad (2)$$

where D is the diffusivity of the rate-controlling solute, C_0 , is the solubility limit of that component in the matrix, ν is a stoichiometric factor and V_m is the molar volume of the dispersed phase. In the strictest sense,

the LSW theory assumes an infinitely dilute solution and that all particles are spherical; however, few comparisons with systems which completely adhere to these assumptions have been conducted (3-5). Examination of equation 2 shows that minimum coarsening should result in alloy systems demonstrating low values of σ , D and C .

On the basis of these parameters, Fine (6) proposed a number of intermetallic compounds that form in aluminum as likely candidates for elevated temperature service. Previous X-ray studies (7,8) performed on the Al-transition metal alloy systems have demonstrated that substitution of Ti or V into the tetragonal Al_3Zr or Al_3Hf intermetallic compound reduces the overall lattice mismatch, δ , when dispersed in an Al matrix. For the tetragonal Al_3Zr intermetallic compound, a δ of 2.88% was measured (9), while the addition of V decreases δ to 2.39% for the tetragonal $Al_3(V_{0.975}Zr_{0.125})$ dispersed phase (8).

This composition is very near the solubility limit of V in the tetragonal DO_{22} , Al_3Zr phase.

Since the transition metals have been used extensively as a grain refiner in Al alloys, numerous studies have been performed in the past to characterize the decomposition of Al_3X -type phases from the supersaturated solid solution (10-20). Though the exact transformation mode between the intermediate and equilibrium phases remains unresolved, it is known that the equilibrium tetragonal phase, DO_{22} -type, is preceded by a surprisingly stable cubic phase, $L1_2$ -type, in the form of spheres and/or rods. Qualitative metallography has found that it is the presence of these small spherical particles which pin grain and subgrain boundaries and thereby inhibit grain growth. Thus, the stability of this cubic phase is of primary concern in Al alloys employed at elevated temperatures.

It was the objective of this study during the past year to 1) determine if the improved lattice matching previously observed in the equilibrium tetragonal $Al_3(V_{0.275}Zr_{0.125})$ over the unalloyed Al_3Zr phase is also found in the respective metastable cubic phase and 2) investigate what effect lattice disregistry in both the intermediate and equilibrium phases has on the decomposition and coarsening kinetics in Al - V - Zr alloys. Furthermore, as a result of the limited solubility of the transition metals in Al (21) as well as the spherical intermediate phase which has been reported in these alloys (11-20) and the small volume fraction of the $L1_2$ dispersed phase in the alloys studied, direct correlation with the LSW theory is possible.

Experimental Procedure

Small, approximately 5 gram Al - Zr and Al - V - Zr alloy buttons were prepared in a Ti gettered argon atmosphere by nonconsumable W arc melting using a water cooled Cu cathode as the crucible. The Al was 99.996% pure, the V was Johnson - Mathey spectrochemical grade and the Zr was cut from bars prepared by the Van Arkel process, i.e., thermal reduction of iodides. Each button was melted four to five times and inverted between melting to ensure homogeneity. Compositional analysis performed by Alcoa reaffirmed that minimal vaporization losses occurred.

To evaluate the effect of improved lattice matching on the decomposition kinetics, alloy buttons containing Al - 0.35 w/o Zr and Al - 0.40 w/o V - 0.10 w/o Zr were initially cold rolled to 5% of their original thicknesses prior to isothermal aging at 450°C and 600°C. These compositions were selected since they represent approximately the same extent of supersaturation above the

peritectic solubility limit. For additional analysis, a second set of buttons underwent straight isothermal aging at 375°C.

For coarsening analysis, alloy buttons containing approximately 1 v/o Al_3Zr and 1 v/o $\text{Al}_3(\text{V}_{0.875}\text{Zr}_{0.125})$ were prepared. To evaluate the coarsening kinetics of the intermediate cubic phase, specimens were isothermally aged at 375°C and 425°C, however, a preaging treatment at 600°C for 1 hour was necessary in those specimens aged at the lower temperature, since cellular precipitation was found following straight aging at 375°C. To promote the formation of the equilibrium tetragonal Al_3Zr phase for coarsening analysis, a third set of specimens were initially cold rolled by 90% and pre-heat treated at 600°C for 50 hours. Following cold rolling and heat treating, both systems underwent isothermal aging at 425°C. Since quenched-in dislocation loops are often confused with coherent, spherical precipitates in the TEM, all specimens were air cooled following aging. In all cases, the temperature was controlled to $\pm 1^\circ\text{C}$ in a vacuum of 5×10^{-6} Torr.

TEM foils were then spark machined and mechanically thinned prior to electropolishing in a solution of 80% CH_3OH - 20% HNO_3 at 50 V and at -70°C . The foils were examined in a 200 kV Hitachi H-700H electron microscope at an operating voltage of 175 kV. A two beam condition was used to take advantage of the "butterfly" strain contrast shown by the metastable, cubic $\text{Al}_3(\text{V},\text{Zr})$ precipitates and a weak-beam, darkfield technique was employed to resolve dislocation/precipitate interaction. For electron diffraction analysis, the techniques outlined by Hirsch et al. (22) and Edington (23) were employed.

Results

Lattice Disregistry of the Cubic $Al_3(V,Zr)$ Phases

To measure the lattice parameters of both the finely dispersed cubic Al_3Zr and $Al_3(V_{0.875}Zr_{0.125})$ phases, electron diffraction analysis was performed. With the Al matrix acting as a camera constant standard, spacings between superlattice reflections were measured on a densitometer and where possible, Kikuchi line spacings were measured. The results of the diffraction analysis in specimens isothermally aged at $425^\circ C$ for various lengths of time are presented in figure 1 for both systems studied. The dashed line represents the lattice parameter of pure Al, 0.40495nm, and was included so direct comparison can be made. As may be seen with the Al_3Zr phase aged at $425^\circ C$, the mismatch reaches a plateau after 100 hours at approximately $1.0 \pm 0.2\%$. The plateau may signify loss of perfect coherence. This result is in good agreement with past studies performed on this system (11-16). Alternatively, for the $Al_3(V_{0.875}Zr_{0.125})$ phase, the measured lattice parameter deviates only slightly and most notably, is negative. Diffraction analysis following 400 hours of aging determined the lattice disregistry to be approximately $-0.2 \pm 0.2\%$.

Effect of δ on the Decomposition Kinetics

To investigate the effect of lattice disregistry on the decomposition kinetics, Al alloys containing 0.35 w/o Zr and 0.40 w/o V - 0.10 w/o Zr were isothermally aged at $375^\circ C$. Since neither electron nor light microscopy revealed the presence of any second phase particles in the as-cast microstructure, it appears that chill casting has extended the solubility limit beyond the equilibrium concentration; 0.28 w/o and 0.37 w/o for Zr and V

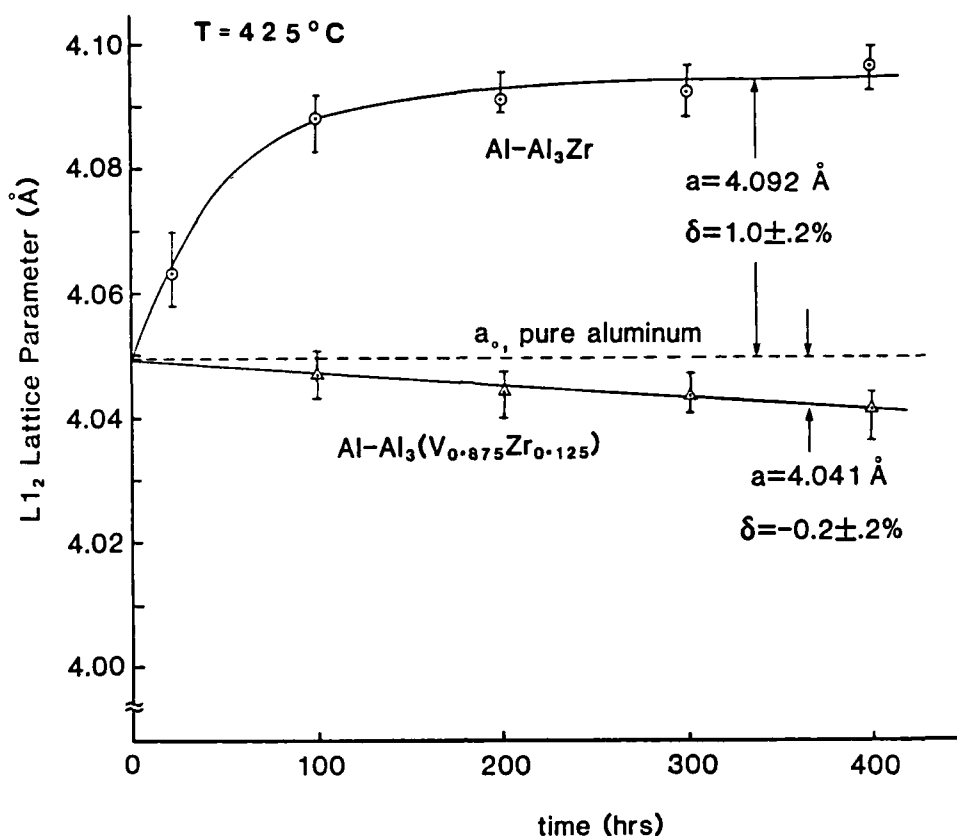


Figure 1. The variation in lattice disregistry of both the cubic Al_3Zr and $\text{Al}_3(\text{V}_{0.875}\text{Zr}_{0.125})$ as a function of aging time at 425°C as measured by electron diffraction.

in binary Al, respectively (24,25). As may be seen in figures 2(a-d), decomposition from the supersaturated solid solution was observed to occur in both alloy systems by a discontinuous mode of precipitation. Migrating grain boundaries act as natural sinks for solute atoms and leave cellular precipitates behind in their wakes. As a result, only short range diffusion is in operation, and results in a more refined dendritic structure at longer aging times, Fig. 2d. Even following 300 hours of aging at 375°C , selected area electron diffraction analysis identified all precipitates to be of the cubic, L1_2 -type.

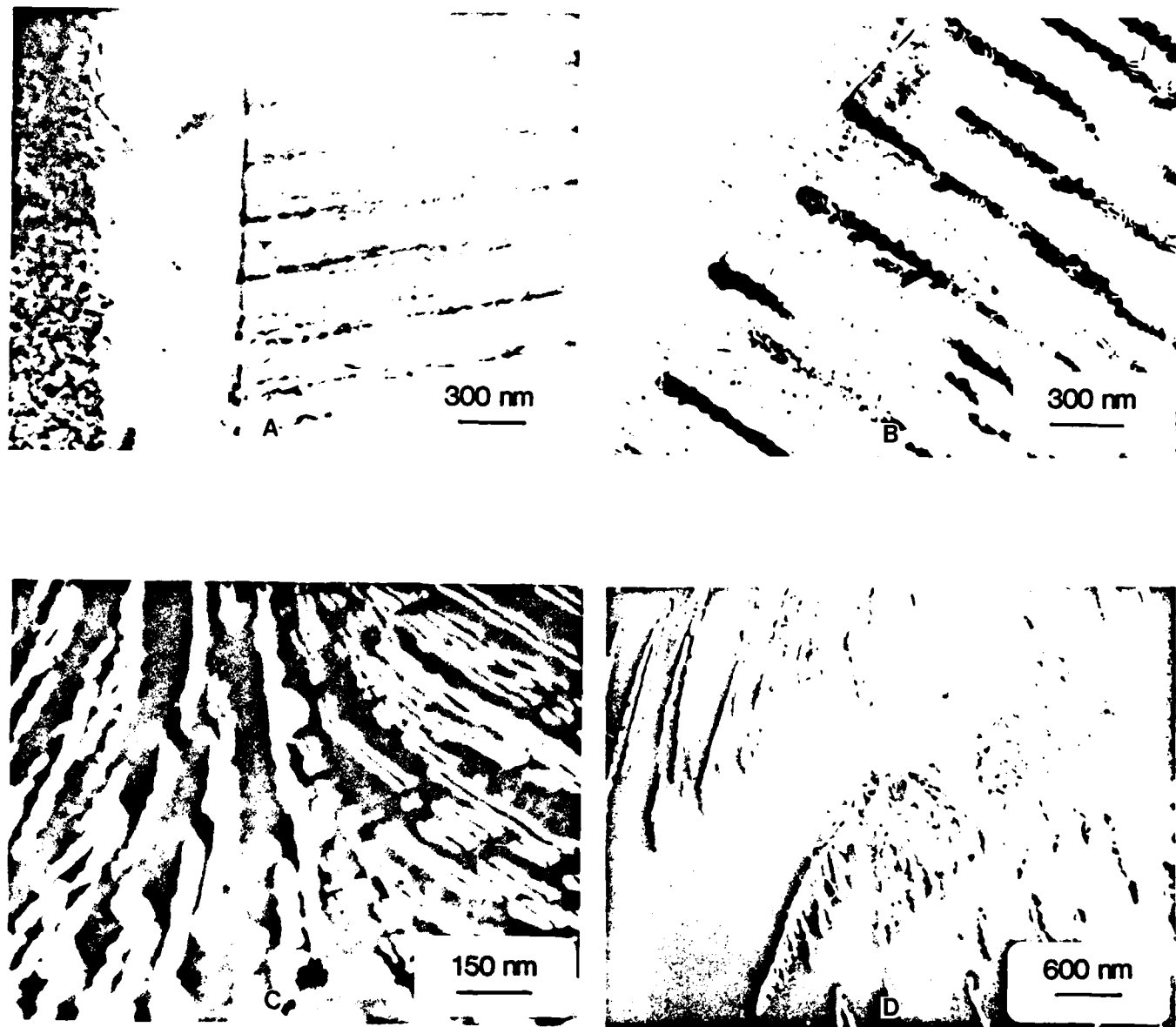
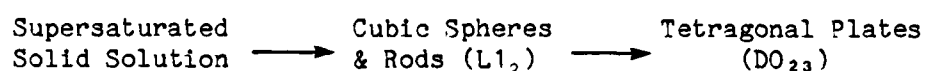


Figure 2. TEM micrographs of discontinuous precipitation reaction observed for the $\text{Al}_3(\text{V,Zr})$ phases following aging at 375°C for (a) 50 hrs., (b) 200 hrs., (c) 200 hrs. and (d) 300 hrs.

To enhance nucleation and minimize discontinuous precipitation, a second set of alloys were initially cold rolled 95% prior to isothermal aging at 450°C. Though cold rolling was found to enhance the kinetics of decomposition from that previously reported, in both the Al - Zr and Al - V - Zr systems studied, the decomposition from the supersaturated solid solution was observed to follow the generally agreed upon sequence of precipitation, i.e.,



For the alloy containing 1 v/o Al_3Zr with a δ of $1.0 \pm 0.2\%$ and 2.88% for the cubic and tetragonal phases, respectively, following 0.5 hours of aging at 450°C, approximately 20 nm, spherical particles were observed, some located on dislocations as well as on sub-grain boundaries, figure 3a. With continued aging, the density of precipitates appeared constant and initially no apparent increase in size was observed. Electron diffraction analysis of such areas verified them to be of the ordered, L1_2 -type with a lattice parameter and orientation nearly that of the Al matrix. As in previous studies, precipitation again was not uniform, yet the "fan-shaped", discontinuous precipitation reaction was not apparent. Following 5 hours of aging, spherical Al_3Zr particles were often seen connected by dislocations and in many instances, oriented along crystallographic directions (fig. 3b). Such connecting dislocations may act as a conduit for solute diffusion and may result in the apparent coalescence and formation of rod-shaped particles, evident after 10 hours of aging, (fig. 3c). Expectantly, following 13.5 hours of aging, the microstructure consisted of a combination of well defined spherical and rod-shaped particles, as shown in figure 3d. By using a weak

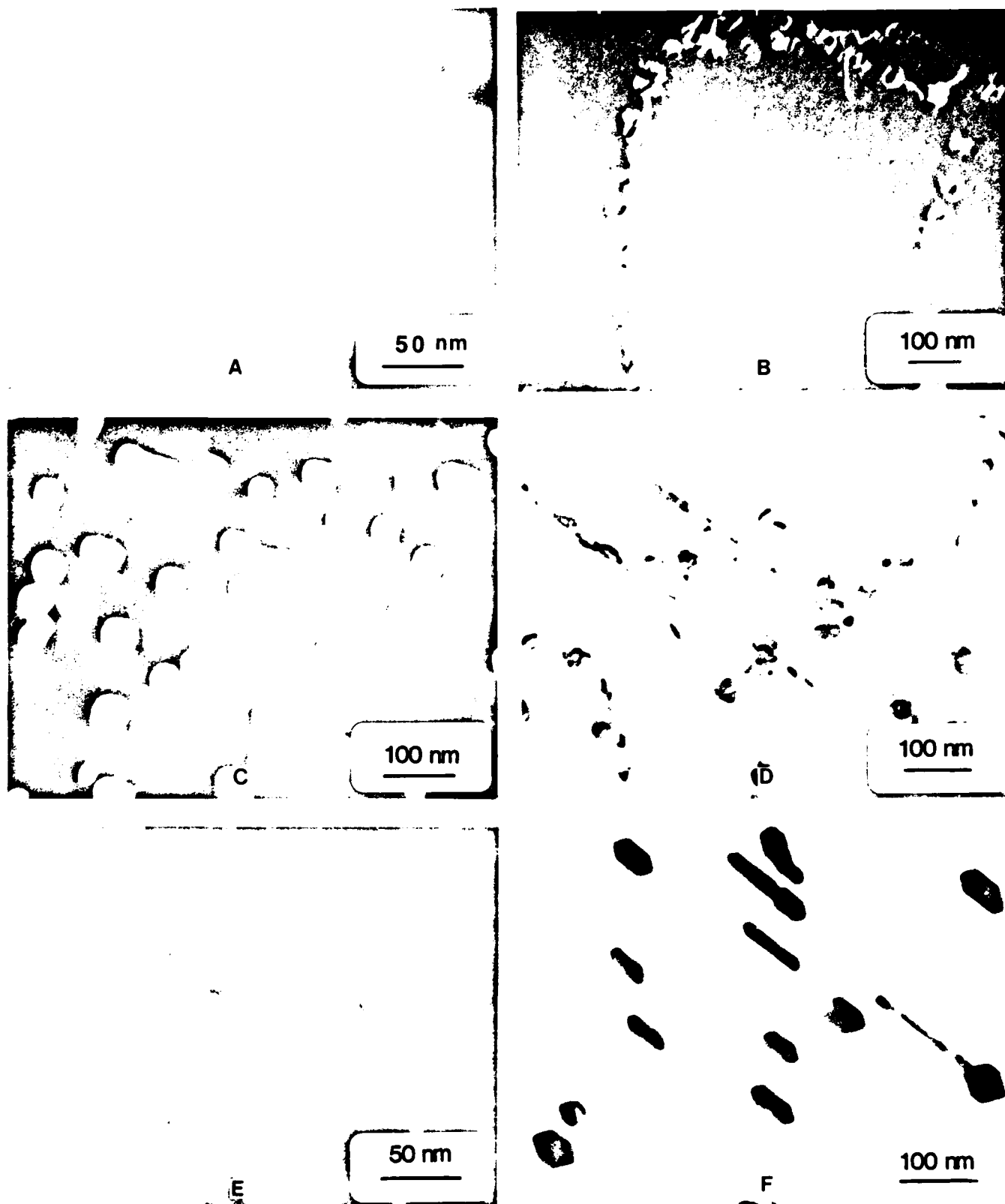


Figure 3. TEM micrographs following the decomposition of the Al_3Zr phase following 95% cold rolling and aging at 450°C for (a) 0.5 hrs., (b) 5 hrs., (c) 10 hrs., (d) 13.5 hrs., (e) 13.5 hrs. and (f) 20 hrs.

beam-dark field technique to reduce the large diffracted intensity associated with the rod-shaped particles, it was possible to resolve the exact interaction between such precipitates and any associated dislocations (fig. 3e). As may be seen, precipitation on a dislocation associated with helical climb appears to be responsible for the formation of such rod-shaped precipitates. Furthermore, the absence of matrix strain contrast and the associated interfacial dislocation structure is representative of a precipitate which is incoherent.

The first appearance of the equilibrium tetragonal Al_3Zr phase became apparent following 20 hours of aging at 450°C . Examination revealed that the precipitates were platelike with faceted caps, Fig. 3f, and demonstrated an orientation within the Al matrix identical to that proposed by Izumi and Oelschlagel (12), i.e.,

$$\langle 001 \rangle_{\text{Al}_3\text{Zr}} // \langle 001 \rangle_{\text{Al}} \quad (100)_{\text{Al}_3\text{Zr}} // (100)_{\text{Al}} \quad .$$

To determine if a reduction in lattice disregistry had an effect on the decomposition kinetics from the supersaturated solid solution, an identical study was performed on an Al alloy containing 1 v/o of the $\text{Al}_3(\text{V}_{0.875}\text{Zr}_{0.125})$ phase with a δ of $-0.2 \pm 0.2\%$ and 2.39% for the cubic and tetragonal phases, respectively. Overall, the decomposition followed an identical sequence to that previously observed for the unalloyed Al_3Zr , however, the kinetics of decomposition appeared appreciably more sluggish. As compared to 13.5 hours for the unalloyed Al_3Zr phase, for the $\text{Al}_3(\text{V}_{0.875}\text{Zr}_{0.125})$ phase it was not until after 20 hours of aging that the coalescence and formation of rod-shaped particles was observed. Furthermore, as compared to 20 hours in the Al_3Zr phase, for the $\text{Al}_3(\text{V}_{0.875}\text{Zr}_{0.125})$ phase it was not until after 100 hours of

aging that the equilibrium tetragonal phase was finally observed.

The kinetics of growth of the intermediate cubic phase are quantitatively summarized in figure 4, where the average radius r is plotted versus time. These data are prior to the observance of the equilibrium tetragonal phase, 20 hours in the Al - Al_3Zr system versus 100 hours in the Al - $\text{Al}_3(\text{V}_{0.875}\text{Zr}_{0.125})$ system. As may be seen, the increased stability of the cubic $\text{Al}_3(\text{V}_{0.875}\text{Zr}_{0.125})$ phase compared to the unalloyed Al_3Zr phase results in a decrease in the growth rate by a factor of approximately five times.

In an attempt to observe a direct transformation from the cubic phase to the tetragonal phase, bypassing coalescence and the formation of rod-shaped particles, a third set of Al - Al_3Zr specimens were initially cold rolled by 95% and isothermally aged at 600°C. Again, copious precipitation was observed

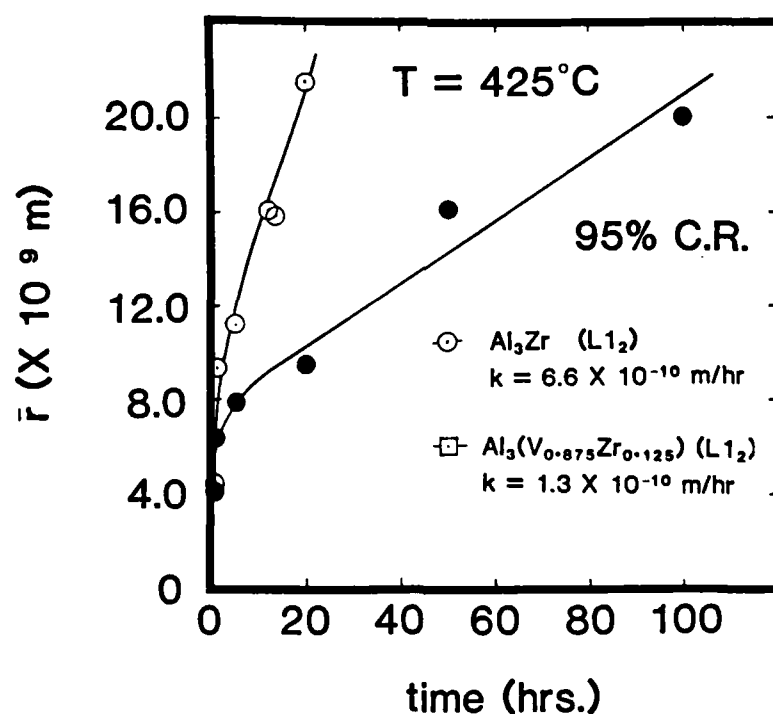


Figure 4. Growth kinetics of the cubic $\text{Al}_3(\text{V},\text{Zr})$ phases prior to observance of the equilibrium tetragonal phases in specimens cold rolled by 95% and aged at 450°C.

almost immediately in the form of small spherical particles. Following 12 hours of aging at 600°C, a healthy dispersion of $L1_2$, Al_3Zr particles is once again observed, yet some of the particles are becoming lenticular in shape and oriented along $[110]$ directions (Fig. 5a). With continued aging it is readily apparent that the lenticular particles are growing at a faster rate than the smaller, spherical particles. Furthermore, examination within some of the smaller particles in figures 5a & b reveal sharp lines of contrast which are thought to be Antiphase Domain Boundaries (APB). Their appearance is similar to that observed in $AuCu_3$ samples (26) and support Ryum's model for the transformation from the cubic $L1_2$ phase to the tetragonal DO_{22} phase by the formation of an APB with a displacement vector $R = \bar{a}/2[110]$ on $\{100\}$ type planes (18). With continued aging, figures 5c & d, all of particles were observed to be lenticular in shape prior to forming the equilibrium tetragonal structure previously observed.

Effect of δ on the Coarsening Kinetics of both the Cubic and Tetragonal $Al_3(V,Zr)$ Phases.

The coarsening kinetics of both the cubic Al_3Zr and $Al_3(V_{0.975}Zr_{0.125})$ phases and the tetragonal Al_3Zr phase at 425°C are shown in figures 6 and 7, respectively. Typical micrographs of both the cubic and tetragonal precipitates are shown in figures 8 and 9, respectively. For the spherical, cubic particles, the particle diameter was taken as the line of no contrast, while for the tetragonal, plate-like phase the diameter was measured along the minor axis of the plate as well as the apparent length along the major axis. For the cubic Al_3Zr phase, coarsening kinetics were also measured following isothermal aging at 375°C. As predicted by the LSW theory of diffusion-

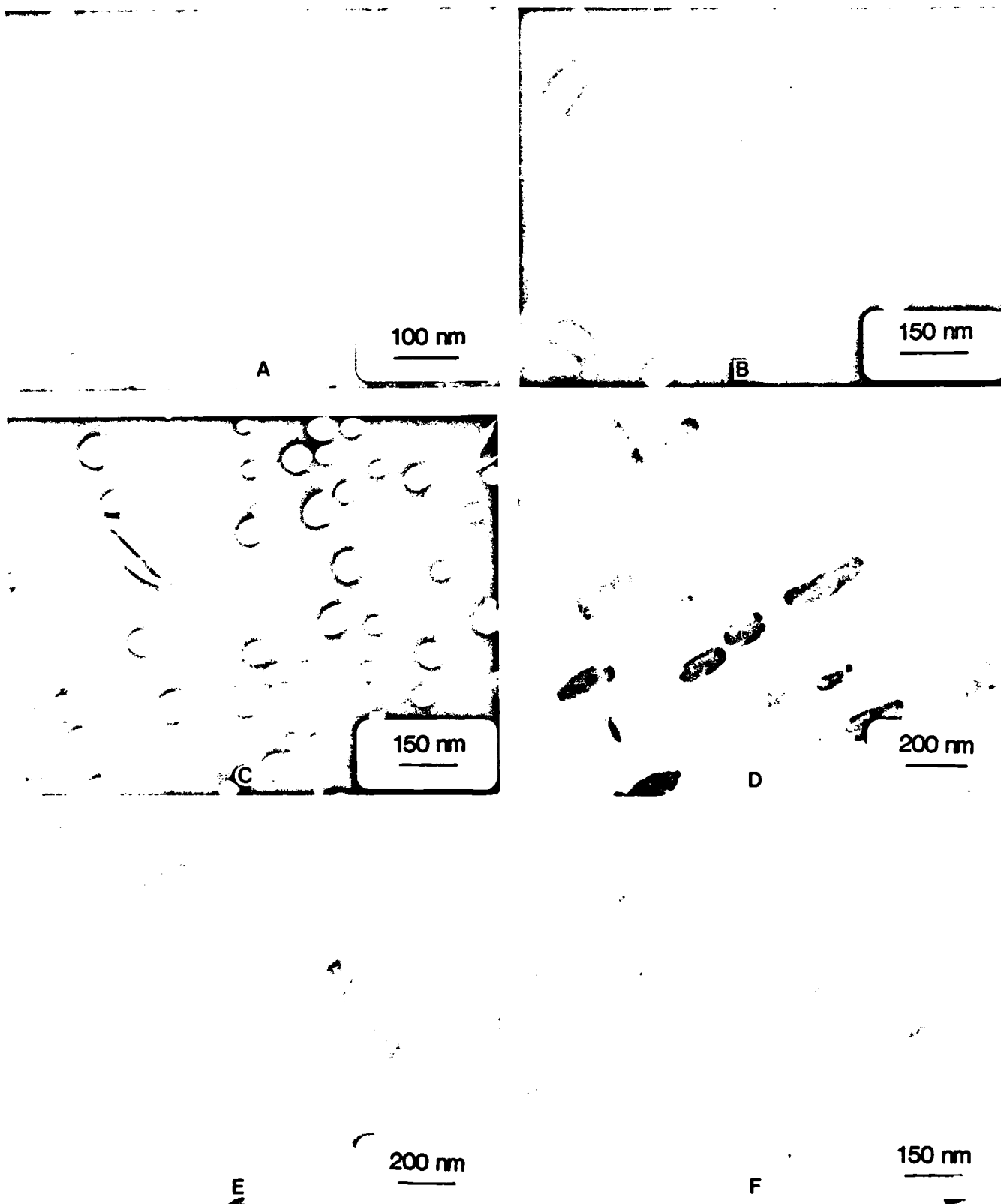


Figure 5. TEM micrographs showing the direct transformation from the cubic (L1₂) Al₃Zr phase to the tetragonal (DO₂₃) phase following 95% cold rolling and aging at 600°C for (a) 12 hrs., (b) 12 hrs., (c) 15 hrs., (d) 20 hrs., (e) 25 hrs. and (f) 25 hrs.

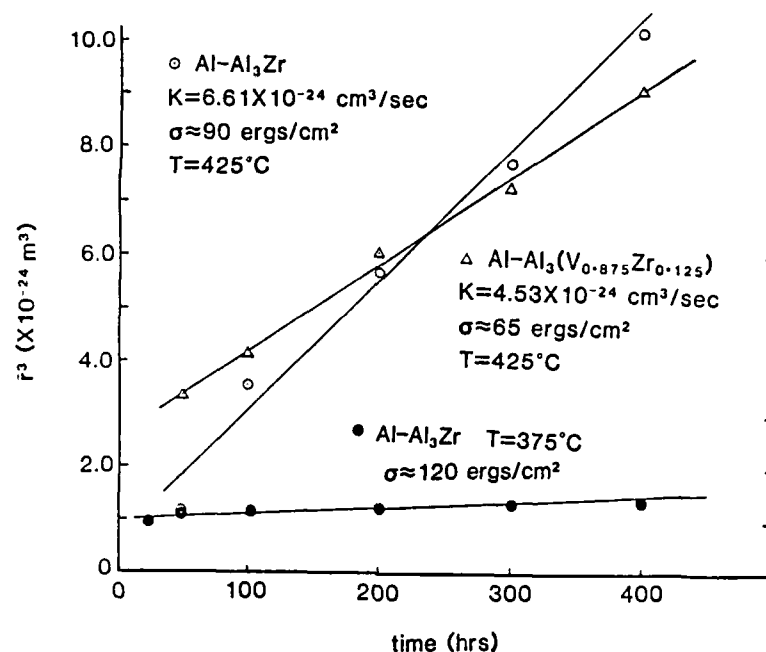


Figure 6. Coarsening kinetics of the cubic ($L1_2$), Al_3Zr and $\text{Al}_3(\text{V}_{0.875}\text{Zr}_{0.125})$ phases at 375°C (•) and 425°C. \bar{r} is the average particle radius at a particular time t .

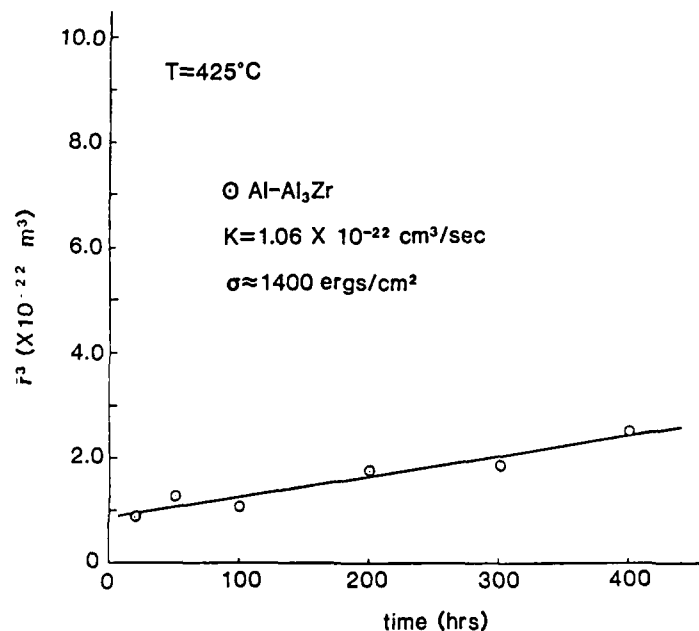


Figure 7. Coarsening kinetics of the tetragonal Al_3Zr phase at 425°C. \bar{r} is the average particle radius measured along the minor axis of the plate.

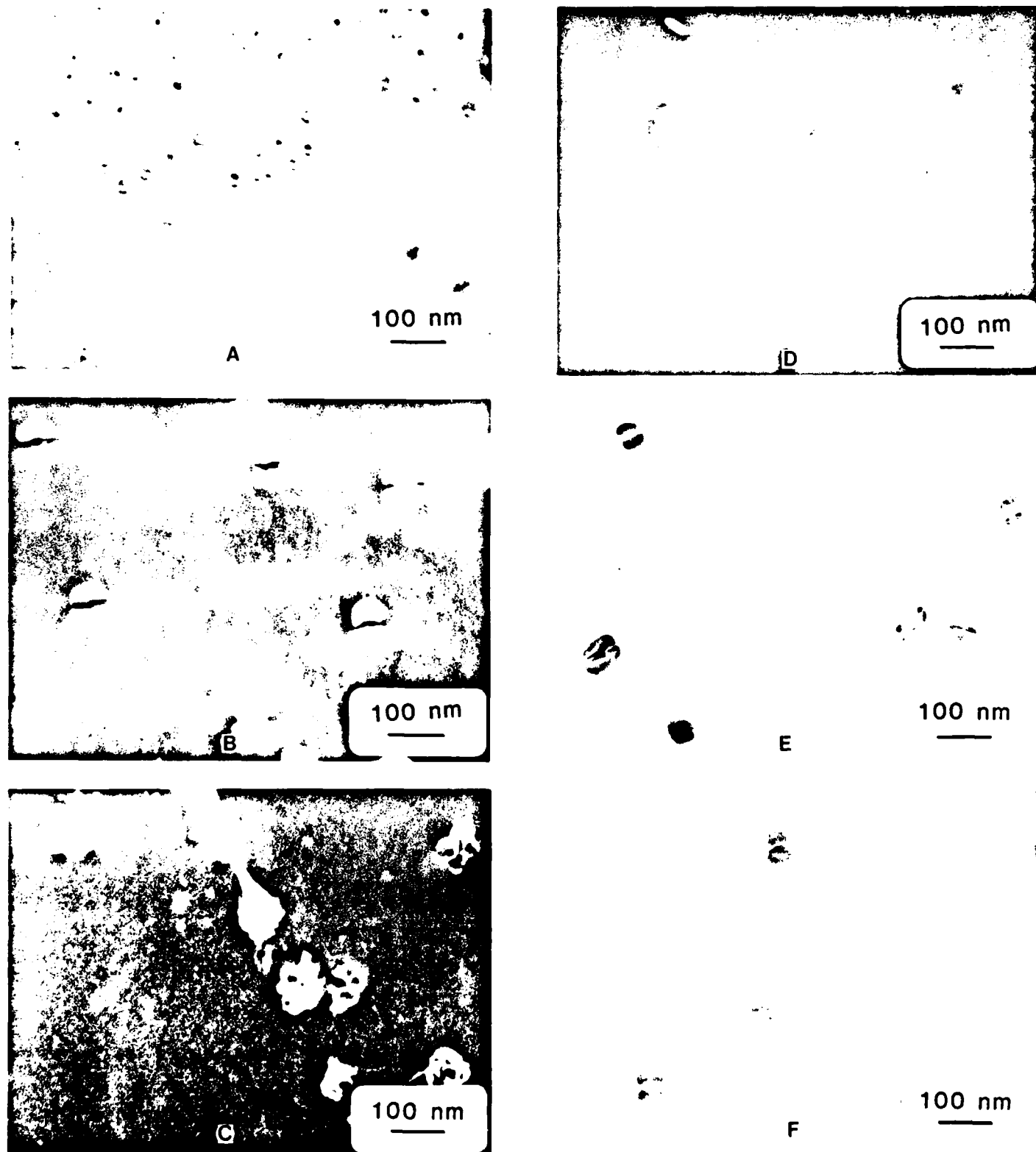


Figure 3. Transmission electron micrographs showing the coarsening kinetics of both the cubic Al_3Zr (a-c) and $\text{Al}_3(\text{V}_{0.998}\text{Zr}_{0.123})$ phases (d-f) after aging at 425°C for (a,d) 5hrs., (b,e) 200 hrs. and (c,f) 400 hrs.

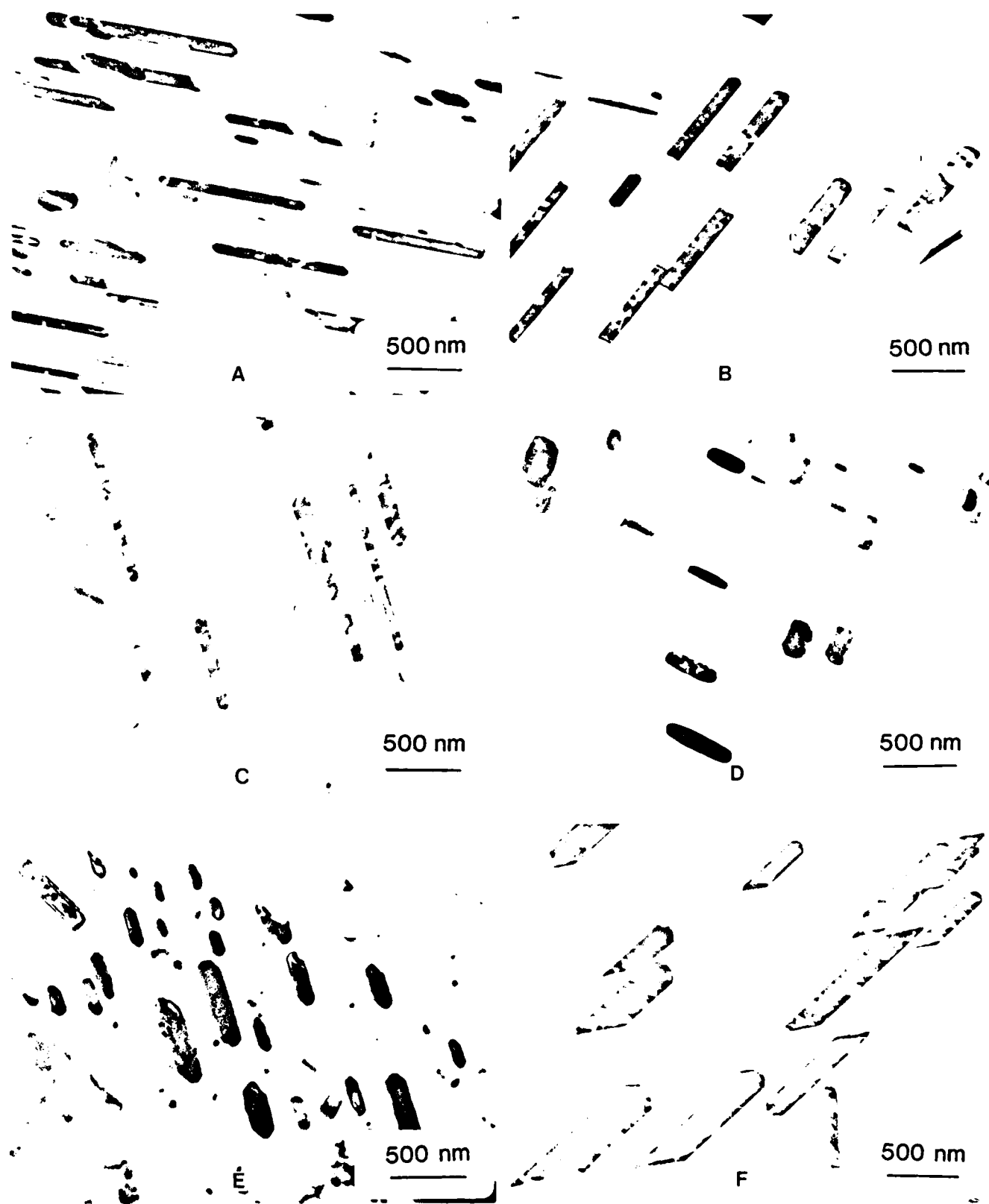


Figure 9. Transmission electron micrographs showing the coarsening kinetics of the tetragonal Al_2Zr phase following aging at 425°C for (a) 20 hrs., (b) 50 hrs., (c) 100 hrs., (d) 200 hrs., (e) 300 hrs. and (d) 400 hrs.

controlled coarsening (eqns. 1,2), a linear relationship between the cube of the average particle radius and the time is obtained for both systems and phases investigated. Through a least squares analysis, the coarsening rates and hence, the interfacial energies of each of the phases may be determined. The values of the rate constants, k , the relevant parameters, D , C_o , and V_m as well as the interfacial energies, σ , are reported in Table 1. In the analysis, the diffusivity of V in Al was not used since it was greater than the diffusivity of Zr in Al (21).

The particle size distributions for each of the systems, phases and aging temperatures investigated are reproduced in figures 10 - 13. In each system, the distribution profiles represent measurements of a minimum of 400 particles and a maximum of nearly 1000 particles. The solid line in each figure represents the "quasi-steady-state" distribution predicted by the LSW theory of Ostwald ripening and given by the function

$$f(r,t) = f'(t) \rho^2 h(\rho) \quad (3)$$

where $f(t)$ is a function of time only, $\rho = r/\bar{r}$ and $h(\rho)$ is given by

$$h(\rho) = \left(\frac{3}{3+\rho}\right)^{7/3} \left(\frac{3/2}{3/2-\rho}\right)^{11/3} \exp\left(\frac{-\rho}{3/2-\rho}\right) \quad (4)$$

$$\rho < \rho_c = 3/2; h(\rho) = 0, \rho > \rho_c = 3/2 \quad .$$

As shown for the Al - cubic Al_3Zr system aged at $375^\circ C$ (following a preage at $600^\circ C$ for 1 hour), figure 10, there is very good agreement between the experimental histograms and the predicted distribution profile. The only discrepancies are apparent in the peak position being slightly skewed left and cut-off sizes greater than the predicted value of $\rho_c = 1.5$. As shown in figures 11 and 12, for both the Al - cubic Al_3Zr and Al - cubic

Table 1. Experimentally determined interfacial energies for the cubic and Al_3Zr and $\text{Al}_3(\text{V}_{0.875}\text{Zr}_{0.125})$ phases and the tetragonal Al_3Zr phase.

Compound	Structure	T (C)	D_{Zr}^* $\left(\frac{\text{cm}^2}{\text{sec}}\right)$	C_o^\dagger $\left(\frac{\text{moles}}{\text{cm}^3}\right)$	V_m $\left(\frac{\text{cm}^3}{\text{mole}}\right)$	K	σ $\left(\frac{\text{ergs}}{\text{cm}^2}\right)$
$\text{Al}-\text{Al}_3\text{Zr}$	(Ll_2)	375	1.78×10^{-15}	2.5×10^{-5}	41.28	3.38×10^{-25}	66
$\text{Al}-\text{Al}_3\text{Zr}$	(Ll_2)	425	3.24×10^{-14}	3.1×10^{-5}	41.28	6.91×10^{-24}	66
$\text{Al}-\text{Al}_3(\text{V}_{0.875}\text{Zr}_{0.125})$	(Ll_2)	425	3.24×10^{-14}	3.1×10^{-5}	39.83	4.53×10^{-24}	47
$\text{Al}-\text{Al}_3\text{Zr}$	(DO_{23})	425	3.24×10^{-14}	3.1×10^{-5}	41.94	1.06×10^{-22}	986

* The diffusivity of Zr in the Al matrix was calculated from the equation $D_{\text{Zr}} = 728 \exp(-218500/\text{RT})$ where Q was empirically determined from a plot of $1/n(\text{KT}/C_o)$ vs. $1/T$ using present coarsening data measured at 375°C and 425°C.

† C_o determined from formula $C_o = \rho_x W_e / M_{\text{Zr}}$, where ρ_x is the density of Al solid solution (assumed to be the density of pure Al) with weight fraction W_e of Zr. M_{Zr} is the atomic weight of Zr.

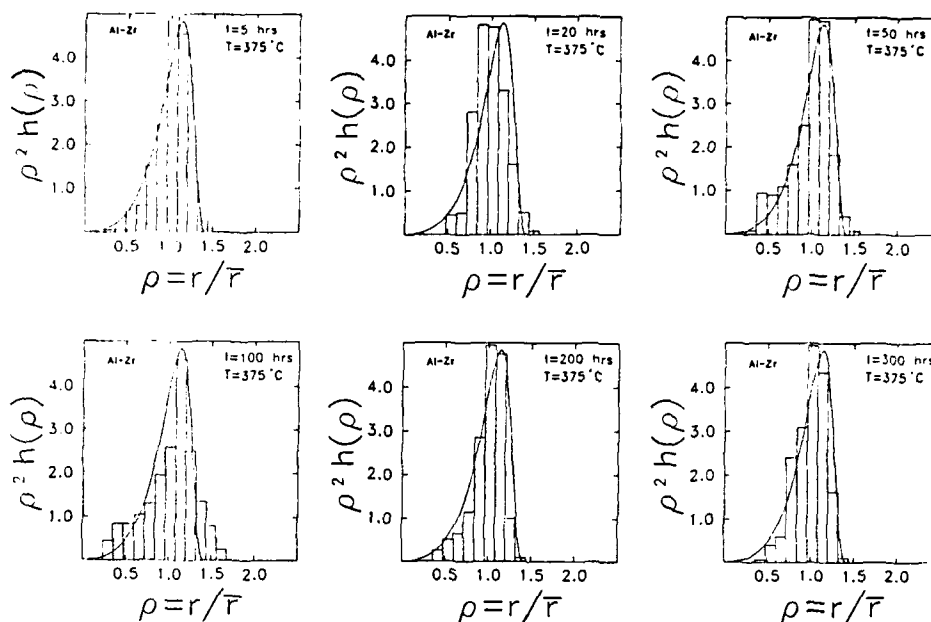


Figure 10. Comparison of the experimental particle size distributions for the cubic Al_3Zr phase aged at 375°C with the LSW predicted distribution function, $\rho^2 h(\rho)$.

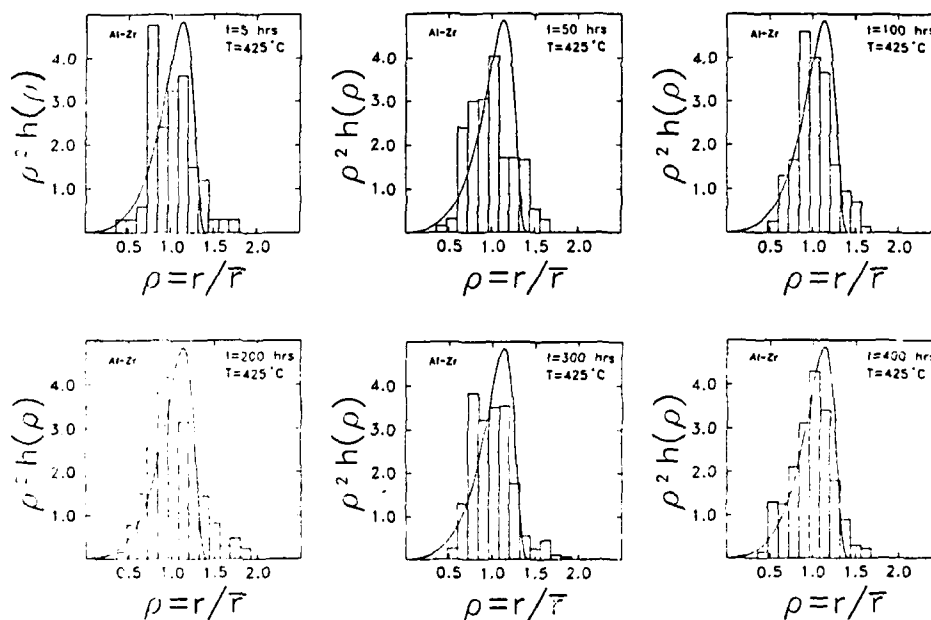


Figure 11. Comparison of the experimental particle size distributions for the cubic Al_3Zr phase aged at 425°C with the LSW predicted distribution function, $\rho^2 h(\rho)$.

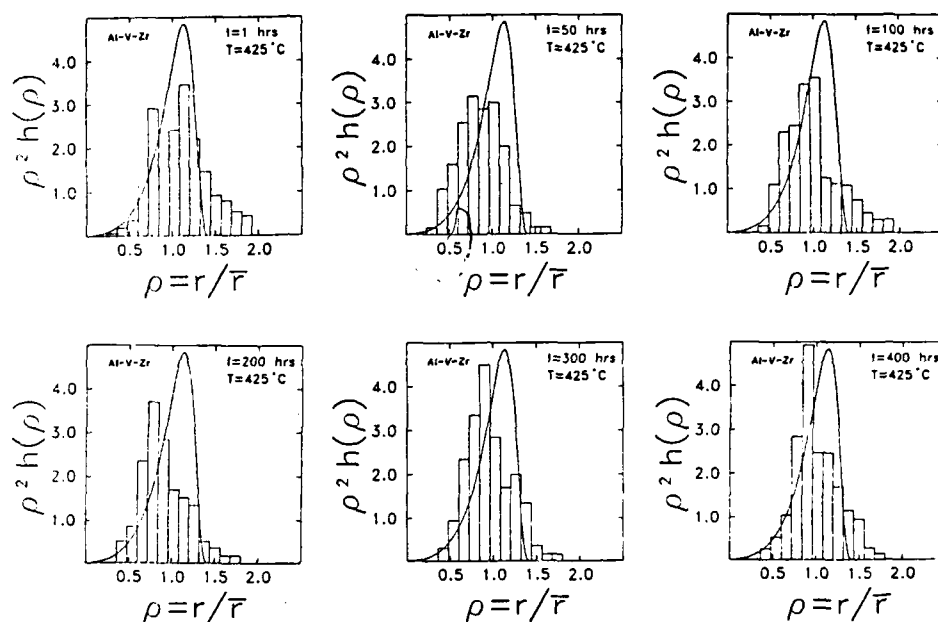


Figure 12. Comparison of the experimental particle size distributions for the cubic $\text{Al}_3(\text{V}_{0.375}\text{Zr}_{0.625})$ phase aged at 425°C with the LSW predicted distribution function, $\rho^2 h(\rho)$.

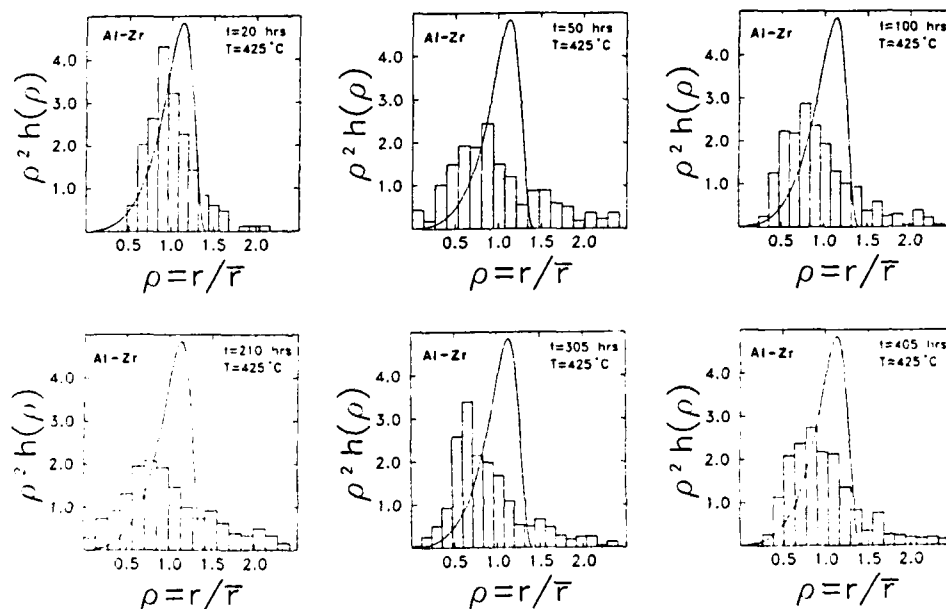


Figure 13. Comparison of the experimental particle size distributions for the tetragonal Al_3Zr phase aged at 425°C with the LSW predicted distribution function, $\rho^2 h(\rho)$.

$\text{Al}_3(\text{V}_{0.875}\text{Zr}_{0.125})$ systems aged at 425°C , these same discrepancies are also found, and are even more accentuated. For the Al - cubic Al_3Zr system, only after 400 hours of aging does there appear to be an evolution toward a steady state distribution.

The distribution profile for the Al - tetragonal Al_3Zr system aged at 425°C is shown in figure 13. Generally speaking, the experimental histograms tend to be more log-normal with skewed and depressed peaks as well as extremely long tails when compared with the LSW predicted distribution function, $\sigma^2 h(\rho)$.

Effect of Cold Rolling on the Coarsening Kinetics of the Cubic $\text{Al}_3(\text{V,Zr})$ Phases.

To investigate the effect of cold rolling on the coarsening kinetics, alloy buttons containing Al - 0.35 w/o Zr and Al - 0.40 w/o V - 0.10 w/o Zr were initially cold rolled to 5% of their original thickness prior to isothermal aging at 450°C . Prior to forming the equilibrium tetragonal $\text{Al}_3(\text{V,Zr})$ phases, the coarsening kinetics of both the cubic ($\text{L}1_2$) Al_3Zr and $\text{Al}_3(\text{V}_{0.875}\text{Zr}_{0.125})$ phases at 450°C following cold rolling were measured and are shown in figure 14. For direct comparison, the coarsening kinetics measured for the non-cold rolled $\text{Al}_3(\text{V,Zr})$ phases isothermally aged at 425°C are also included. Aside from the earliest stages of growth, a linear relationship between the cube of the average particle radius and the time is obtained for both cold rolled systems. After correcting for temperature and diffusivity differences (a factor of 4.35 times), comparison of the coarsening rates, k , of both the cold rolled and non-cold rolled cases, indicates that cold rolling had no apparent affect on the coarsening kinetics of the $\text{Al}_3(\text{V}_{0.875}\text{Zr}_{0.125})$ phase; yet, for the unalloyed Al_3Zr phase, the coarsening rate has been enhanced by a factor

of approximately five times, from approximately $2.4 \times 10^{-26} \text{ m}^3/\text{hr}$ to approximately $1.1 \times 10^{-25} \text{ m}^3/\text{hr}$. Thus the difference between the cold rolled and non-cold rolled curves for the $\text{Al}_3(\text{V}_{0.875}\text{Zr}_{0.125})$ alloy is due to temperature change alone, while cold rolling was found to enhance the coarsening rate for the alloy containing the Al_3Zr phase.

Discussion and Conclusions

Careful electron diffraction analysis performed on both the Al - cubic Al-Zr and Al - cubic $\text{Al}_3(\text{V}_{0.875}\text{Zr}_{0.125})$ systems found that the improved lattice matching previously reported (9) for the equilibrium, tetragonal $\text{Al}_3(\text{V}_{0.875}\text{Zr}_{0.125})$ phase over the unalloyed Al_3Zr phase is also found in the

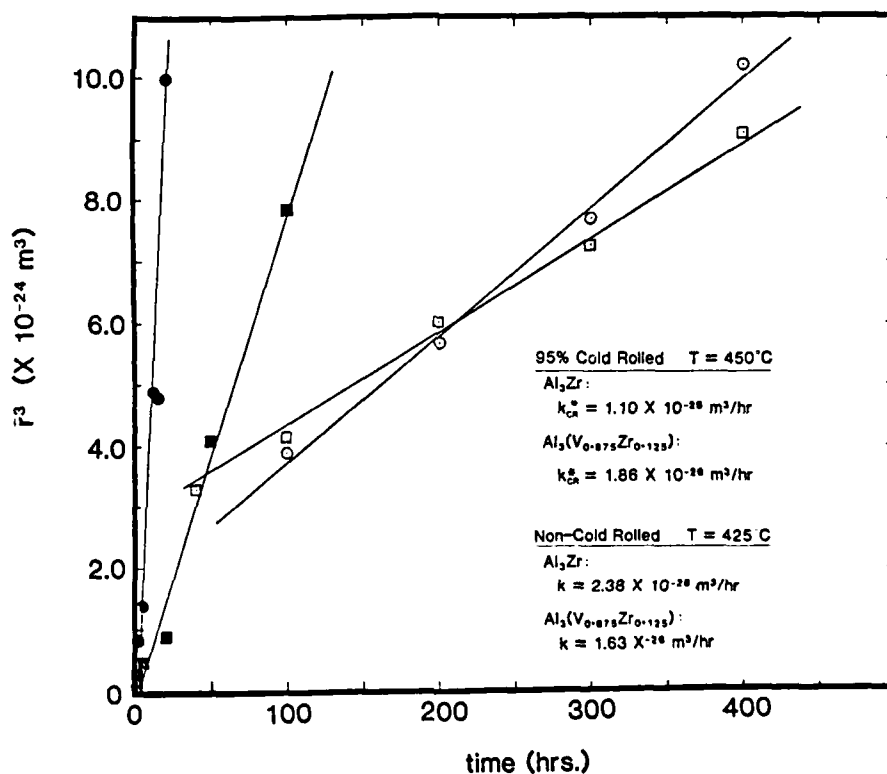


Figure 14. Comparison of the coarsening rates for Al - Al_3Zr ($\text{L}1_2$) and Al - $\text{Al}_3(\text{V}_{0.875}\text{Zr}_{0.125})$ ($\text{L}1_2$) systems in non-cold rolled condition (\circ, \square) and following 95% cold rolling (\bullet, \blacksquare), respectively. * Slope corrected for change in temperature in terms of T and D .

respective metastable cubic phases. Assuming Vegard's Law and $\delta = -0.2 \pm 0.2\%$ and $\delta = 1.0 \pm 0.2\%$ for the cubic $\text{Al}_3(\text{V}_{0.875}\text{Zr}_{0.125})$ and the Al_3Zr phases, respectively, it is possible to predict that the lattice parameter of the cubic Al_3V phase would exhibit a mismatch of approximately $-0.38 \pm 0.2\%$ (Fig. 15). This δ in turn corresponds to a lattice parameter equal to approximately 0.4034nm. Furthermore, it may be predicted that the cubic $\text{Al}_3(\text{V}_{0.875}\text{Zr}_{0.125})$ phase would be perfectly coherent with the Al matrix without lattice strain. Therefore, based on the present investigation, the coherent $\text{Al}_3(\text{V}_{0.875}\text{Zr}_{0.125})$ phase should have an even lower interfacial energy than either of the fore-mentioned phases as well as demonstrate an increased stability at elevated temperatures. This latter result alone could be of great technological importance with regards to the resistance of grain growth at elevated temperatures and is presently being investigated.

Qualitative electron microscopy revealed that the decomposition of the supersaturated solid solution into the matrix and the Al_3Zr or $\text{Al}_3(\text{V}_{0.875}\text{Zr}_{0.125})$ phases was generally identical to that previously observed in all of the Al - tetragonal Al_3X -type systems. Depending on the aging temperature, the metastable, cubic $\text{Al}_3(\text{V,Zr})$ phases was found to form cellular or spherical precipitates. At an aging temperature of 375°C, decomposition from the supersaturated solid solution was observed to occur in both systems by a discontinuous mode of precipitation. Such cellular precipitates with their associated migrating grain boundaries are apparently responsible for the so called "fan-shaped" precipitate configuration often observed in the past (11-14) and are not to be associated with segregated cells in the as-cast structure (11, 13) or a redistribution and coarsening effect (12).

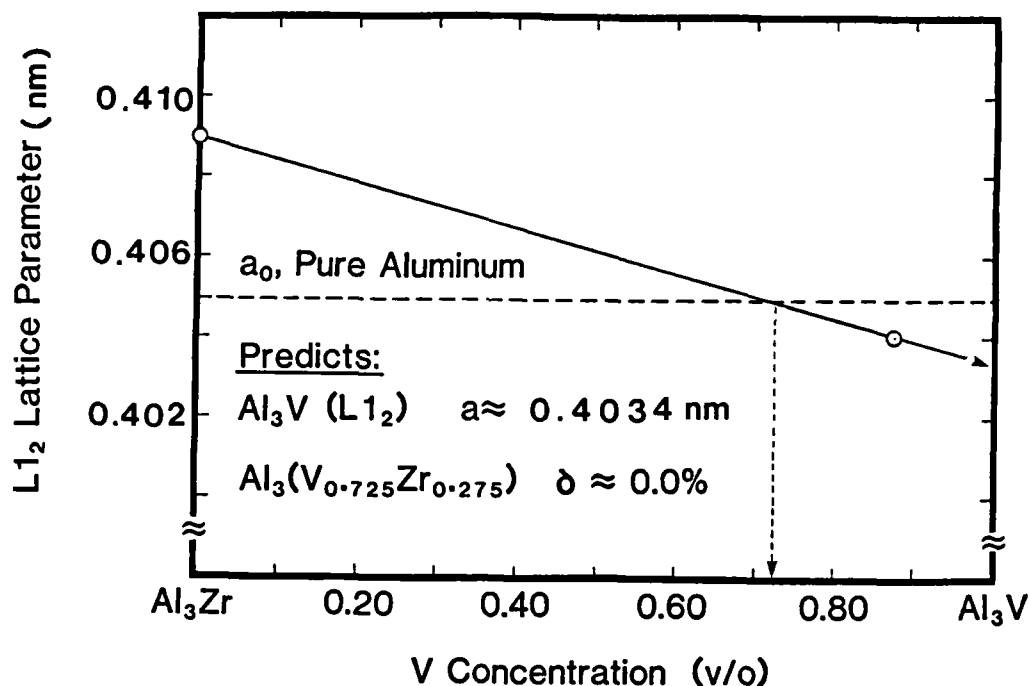


Figure 15. Lattice registry variation of cubic $Al_3(V_xZr_{1-x})$ with composition, X in Al - 1 v/o $Al_3(V,Zr)$ alloys. The dashed line represents the lattice parameter of pure Al.

Decomposition from the supersaturated solid solution following 95% cold rolling and isothermal aging at $450^\circ C$ was initially observed in both systems in the form of spherical, cubic precipitates. At the later stages of growth, rod-shaped cubic particles were often observed and were apparently the result of either a coalescence event (Fig. 3c) or precipitation on dislocations associated with helical climb (Fig. 3e). The latter result is in direct support of a model proposed by Nes (15). Such helical dislocations wrapped around the precipitate may promote a preferential growth direction by generating vacancies as well as by sweeping up nearby solute atoms with their wandering tails. With continued aging, the formation of the equilibrium tetragonal phase was apparent in segregated regions throughout the matrix with plate edges aligned along $\langle 001 \rangle$ and $\langle 110 \rangle$ directions.

The transformation from the metastable, cubic ($L1$) phase to the equilibrium, tetragonal (DO_{23}) phase has been proposed by Ryum (18) to occur through the formation of an antiphase domain boundary (APB), however, this has yet to be observed in an electron microscope for this system. As shown in figure 16, a DO_{23} -type crystal structure may be formed from an $L1_2$ -type structure by an atomic displacement of $\bar{a}/2[110]$ on $\{100\}$ planes. Electron microscopic analysis of specimens aged at 600°C are clearly in support of this model and the obvious mechanism responsible for the formation of the tetragonal phase. From previous research performed in the Al - Cu system, Weatherly (27) found that the two major origins accounting for the formation of an APB are particle coalescence as well as particle dislocation interaction. With this in mind it is not surprising that both mechanisms were previously observed. Furthermore, the latter mechanism could be responsible for the accelerated transformation observed for the unalloyed Al_3Zr phase over the $\text{Al}_3(\text{V}_{0.875}\text{Zr}_{0.125})$ phase,

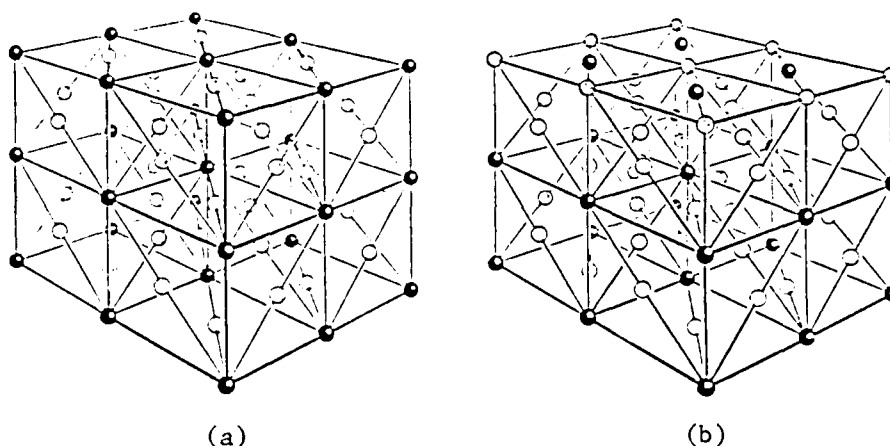


Figure 16. Crystal structures of a) the ordered $\text{Al}_3(\text{V},\text{Zr})$ phase ($L1_2$) and b) the $(111)[110]$ antiphase boundary resulting in an imperfect tetragonal $\text{Al}_3(\text{V},\text{Zr})$ phase (DO_{23}) (28).

since the coherency strain associated with a δ of approximately 1.0% is most easily accommodated by the introduction of dislocations at the particle/matrix interface.

As previously mentioned, the second major objective of this research was to investigate the effect of lattice disregistry on the isothermal coarsening kinetics as well as evaluate the fundamentals of the Lifshitz - Slyozov - Wagner theory of Ostwald ripening. As a result of the limited solubility of both V and Zr in Al and the spherical intermediate phase which forms, the systems are ideal for detailed examination and correlation with the LSW theory.

Quantitative coarsening analysis for both the cubic Al_3Zr and $\text{Al}_3(\text{V}_{0.375}\text{Zr}_{0.125})$ phase as well as the tetragonal Al_3Zr phase are in good agreement with the predicted linear relationship between a plot of the cube of the average radius, r , and isothermal aging time, t . Furthermore, from equation 3, good correlation between the calculated interfacial energy (Table 1) and percent lattice disregistry is found. As expected, the cubic $\text{Al}_3(\text{V}_{0.375}\text{Zr}_{0.125})$ phase with a $\delta = -0.2 \pm 0.2\%$ exhibits an interfacial energy of 47 ergs/cm² as compared with the unalloyed Al_3Zr phase with a $\delta = 1.0 \pm 0.2\%$, exhibiting an interfacial energy on the order of 66 ergs/cm². On the other hand, for the tetragonal Al_3Zr phase with an averaged $\delta = 2.88\%$, an interfacial energy of approximately 986 ergs/cm² was calculated. These results are fairly consistent with previous coarsening studies performed on in some Ni-base alloys with a very small mismatch (29-31) as well as on the phase in an Al-Cu alloy with a large δ (32).

Inspection of the particle size distributions (PSD) show good agreement with theory for the cubic, spherical $\text{Al}_3(\text{V,Zr})$ phases, especially for the Al -

Al₃Zr system preaged at 600°C for 1 hour followed by isothermal aging at 375°C. At virtually all of the times inspected, the histograms fit the predicted distribution function fairly well. Slight tails may be easily explained by measurements made of particles which were associated with dislocations. However, larger discrepancies between theory and experiment are apparent for the cubic phases isothermally aged at 425°C. In general, for both the Al₃Zr and Al₃(V_{0.875}Zr_{0.125}) phases, the distributions appear more log-normal throughout aging and only following 400 hrs of aging does the Al₃Zr phase begin to fit the predicted distribution profile. As may be seen in figure 13, a very poor fit between the predicted distribution profile and the experimental profile results for the plate-like, tetragonal Al₃Zr phase. Generally speaking, the PSD's appear bell-shaped with long tails and poor agreement in terms of the LSW predicted distribution function, $\rho^2 h(c)$.

Concerning the effect of cold rolling, it was found to accelerate the transformation from the metastable L1₂ structure to the equilibrium DO₂₃ structure in both alloy systems studied. For example, in the Al - Al₃Zr system following 95% cold rolling the transformation was observed to begin after 20 hours of aging at 450°C; however, in the absence of cold rolling, the cubic Al₃Zr phase was found to be stable for at least 400 hours in specimens aged at a slightly lower temperature of 425°C. In the Al - Al₃(V_{0.875}Zr_{0.125}) system, the L1₂ phase was much more resistant to promotion of the transformation by cold rolling. It is suggested that there is a greater tendency for the Al₃Zr phase to form on dislocations than the Al₃(V_{0.875}Zr_{0.125}) phase and that these dislocations promote the transformation to the tetragonal structure by assisting formation of antiphase domain boundaries.

As far as the coarsening kinetics are concerned, reducing the mismatch between the matrix and the $L1_2$, Al_3X precipitates reduces the rate of growth of the precipitate particles. Research in progress will verify whether this is also true for the DO_{23} , Al_3X precipitates as expected.

References

1. I.M. Lifshitz and V.V. Slyozov, Z. Eksper. Teor. Fiz. 35, 479 (1958).
2. C. Wagner, Z. Electrochem. 65, 581 (1961).
3. G.R. Speich and R.A. Oriani, Trans. Met. Soc. AIME 233, 623 (1965).
4. J.D. Livingston, Trans. Met. Soc. AIME 215, 566 (1959).
5. A.F. Smith, Acta Met. 15, 1867 (1967).
6. M.E. Fine, Met. Trans. 6A, 625, (1975).
7. S. Tsunekawa and M.E. Fine, Scripta Met. 16, 391 (1982).
8. M. Zedalis and M.E. Fine, Scripta Met. 17, 1247 (1983).
9. G. Brauer, Z. anorg. allg. Chem. 242, 1 (1939).
10. N. Ryum, J. Inst. Met. 94, 191 (1966).
11. N. Ryum, Acta Met. 17, 269 (1969).
12. O. Izumi and D. Oelschlagel, Scripta Met. 3, 619 (1969).
13. M. Sundberg, R. Sundberg and B. Jacobsen, Jernkontoret Ann. 155, 1 (1971).
14. E. Nes and N. Ryum, Scripta Met. 5, 987 (1971).
15. E. Nes, Acta Met. 20, 499 (1972).
16. T. Ohashi and R. Ichikawa, Met. Trans. 3A, 2300 (1972).
17. K.N. Melton, J. Mat. Sci. 10, 1651 (1975).
18. N. Ryum, J. Mat. Sci. 10, 2075 (1975).
19. E. Nes and H. Billdal, Acta Met. 25, 1031 (1977).
20. E. Nes and H. Billdal, Acta Met. 25, 1039 (1977).

21. C.M. Adam, in Rapidly Solidified Amorphous and Crystalline Alloys, B.H. Kear, B.C. Giessen and M. Cohen, editors, Elsevier Science Publishing Co., Inc., 411 (1982).
22. P. Hirsch, A. Howie, R.B. Nicholson, D.W. Pashley and M.J. Whelan, in Electron Microscopy of Thin Crystals, Robert E. Krieger Pub. Co., Inc., New York, 124 (1977).
23. J.W. Edington, in Practical Electron Microscopy in Materials Science, Von Nostrand Reinhold Co., New York, 83 (1976).
24. W.L. Fink and L.A. Willey, Trans. Met. Soc. AIME 133, 69 (1939).
25. A. Roth, Z. Metallkunde 32, 356 (1940).
26. R.M. Fisher and M.J. Marcinkowski, Phil. Mag. 6, 1385 (1961).
27. G.C. Weatherly, Acta Met. 18, 15 (1970).
28. P.A. Flinn, Trans. Met. Soc. AIME 219, 145 (1960).
29. A.J. Ardell and R.B. Nicholson, J. Physics Chem. Solid 27, 1793 (1966).
30. A.J. Ardell and R.B. Nicholson, Acta Met. 14, 1295 (1966).
31. A.J. Ardell, Acta Met. 16, 511 (1968).
32. D. Janoff and M.E. Fine, Mat. Sci. and Eng. 64, 67 (1984).

3. Coarsening Rate of β Phase in Al-Mg Alloys

Since the β phase (nominal composition Mg_2Al_3) in the Al-Mg system is cubic with a lattice parameter 6.97 times that of Al, it was thought that the interface between β and the Al matrix might have a low interfacial energy and, therefore, be of interest for dispersion strengthening in elevated temperature alloys. For this reason, coarsening of β precipitates in an Al-11 wt.% Mg alloy was studied in the temperature range 250 to 330°C. From the modified LSW theory an interfacial energy of approximately 1 J/m² (1000 ergs/cm²) was computed. This high value indicates that the β/α interface is incoherent in spite of the fact that the β lattice parameter is almost an exact multiple of that of the α solid solution. An anomalously high rate of coarsening at 250°C suggests that short circuit diffusion at grain boundaries and dislocations plays a role at this temperature.

4. Elastic Modulus of Al_3Zr

Since one of the desirable objectives of elevated temperature Al alloy development is an increased modulus of elasticity, it was decided to establish the elastic modulus of Al_3Zr . This was done by measuring the modulus, using the pulse echo technique, of a number of alloys with varying volume percent of Al_3Zr and extrapolating to 100% Al_3Zr . The value so established was 192 GPa, compared to 71 GPa for pure Al and 140 GPa for pure δ' Al_3Li (1).

Previously, a rough correlation of Young's modulus with melting temperature had been established (2). The 192 GPa value for Al_3Zr fits this correlation very well. It should be noted that Al_3Zr which melts at 1580°C has one of the highest melting temperatures of intermetallic compounds which are in equilibrium with Al matrix.

References

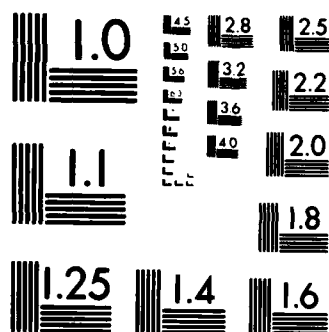
1. M. E. Fine, Scripta Metall. 15, 523 (1981).
2. M. E. Fine, L. D. Brown and H. L. Marcus, Scripta Metall. 18, 951 (1984).

AD-A151 031 SYNTHESIS AND PROPERTIES OF ELEVATED TEMPERATURE P/M 2/2
ALUMINUM ALLOYS(U) NORTHWESTERN UNIV EVANSTON IL DEPT
OF MATERIALS SCIENCE ANDEE M E FINE ET AL 30 NOV 84
UNCLASSIFIED AFOSR-TR-85-0139 AFOSR-82-0005 F/G 11/6 NL

END

FILED

DTIC



MICROCOPY RESOLUTION TEST CHART
NATIONAL BUREAU OF STANDARDS-1963-A

LIST OF PUBLICATIONS -- AF SUPPORTED

1. "Coarsening Rate of β Precipitates in Al-11Mg Alloy", S. I. Kwun and M. E. Fine. Accepted for publication in Metallurgical Transactions A.
2. "Particle Coarsening Studies of RSP-P/M Al-Fe-Ce Alloys", L. Angers, M. E. Fine and J. R. Weertman. In preparation, to be submitted to Metallurgical Transactions A.
3. "Effect of Lattice Disregistry on the Decomposition and Coarsening Kinetics in Supersaturated Al-V-Zr Alloys", M. S. Zedalis and M. E. Fine. In preparation, to be submitted to Metallurgical Transactions A.

LECTURES PRESENTED -- AF SUPPORTED

1. "Coarsening Kinetics of Cubic $Al_3(V,Zr)$ Precipitates in Al-V-Zr Alloys" (given by M. S. Zedalis, with M. E. Fine), TMS-AIME Fall Meeting, Detroit, Michigan, September 16-21, 1984.
2. "An EDS Study of the Dispersed Phase in the Al-Fe-Ce RSP P/M Alloy" (given by L. Angers, with M. E. Fine and J. R. Weertman), TMS-AIME Fall Meeting, Detroit, Michigan, September 16-21, 1984.
3. "Lattice Parameter Variation versus Composition of Al_3Zr and $Al_3V_{0.375}Zr_{0.125}$ in Dilute Al Base Alloys" (given by M. S. Zedalis, with M. E. Fine), TMS-AIME Annual Meeting, Los Angeles, California, February 25-March 3, 1984.
4. "Effect of Plastic Deformation on the Coarsening of a Dispersed Phase in a RSP P/M Al-Fe-Ce Alloy" (given by L. Angers, with M. E. Fine and J. R. Weertman), TMS-AIME Annual Meeting, Los Angeles, California, February 25-March 3, 1984.

PROFESSIONAL PERSONNEL

1. Professor Morris E. Fine, Principal Investigator
2. Professor Julia R. Weertman, Principal Investigator
3. Dr. Jain-Long Horng, Postdoctoral Fellow, 7/16/83-12/11/84.
4. Mr. Michael S. Zedalis, Ph.D. student, Graduate Research Assistant.
5. Ms. Lynette Angers, Ph.D. student, Graduate Research Assistant, Amelia Earhart Fellowship from Zonta 1983-1985.
6. Ms. Mukta V. Ghatge, M.S. student, 6/1/84-8/7/84.
7. Dr. Sook-In Kwun, $\frac{1}{2}$ time, Visiting Scholar, 9/30/83-8/16/84.

END

FILMED

4-85

DTIC